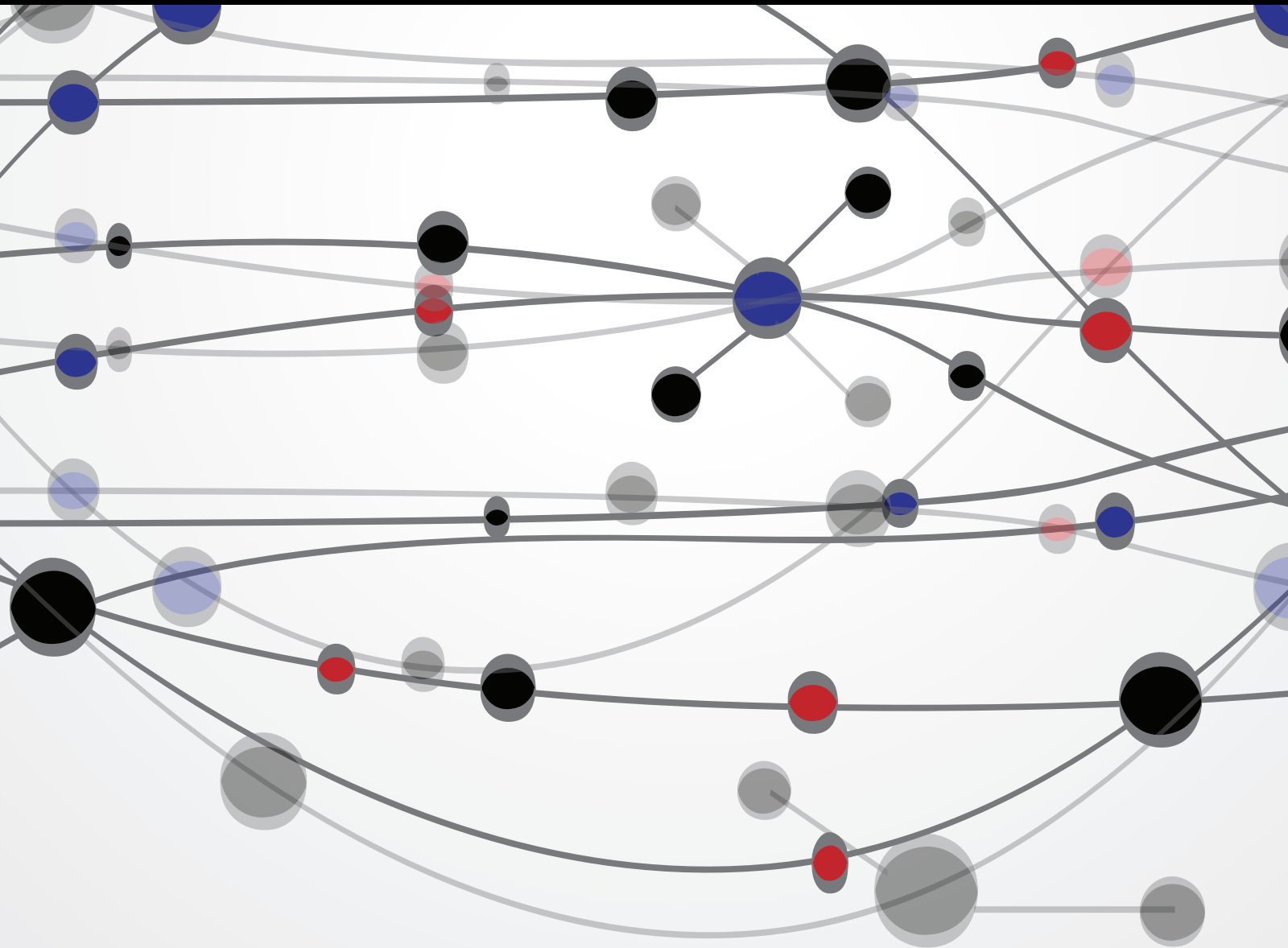


Machine Learning for Medical Applications

Guest Editors: Huiyu Zhou, Jinshan Tang, and Huiru Zheng





Machine Learning for Medical Applications

The Scientific World Journal

Machine Learning for Medical Applications

Guest Editors: Huiyu Zhou, Jinshan Tang, and Huiru Zheng



Copyright © 2015 Hindawi Publishing Corporation. All rights reserved.

This is a special issue published in “The Scientific World Journal.” All articles are open access articles distributed under the Creative Commons Attribution License, which permits unrestricted use, distribution, and reproduction in any medium, provided the original work is properly cited.

Contents

Machine Learning for Medical Applications, Huiyu Zhou, Jinshan Tang, and Huiru Zheng
Volume 2015, Article ID 825267, 1 page

A Novel Method of Early Diagnosis of Alzheimer's Disease Based on EEG Signals, Dhiya Al-Jumeily, Shamaila Iram, Francois-Benois Vialatte, Paul Fergus, and Abir Hussain
Volume 2015, Article ID 931387, 11 pages

EEG-Based Emotion Recognition Using Deep Learning Network with Principal Component Based Covariate Shift Adaptation, Suwicha Jirayucharoensak, SETHA Pan-Ngum, and Pasin Israsena
Volume 2014, Article ID 627892, 10 pages

Induced Effects of Transcranial Magnetic Stimulation on the Autonomic Nervous System and the Cardiac Rhythm, Mercedes Cabrerizo, Anastasio Cabrera, Juan O. Perez, Jesus de la Rúa, Niovi Rojas, Qi Zhou, Alberto Pinzon-Ardila, Sergio M. Gonzalez-Arias, and Malek Adjouadi
Volume 2014, Article ID 349718, 12 pages

Adaptive Bacteria Colony Picking in Unstructured Environments Using Intensity Histogram and Unascertained LS-SVM Classifier, Kun Zhang, Minrui Fei, Xin Li, and Huiyu Zhou
Volume 2014, Article ID 928395, 10 pages

Adaptive Neuro-Fuzzy Inference System for Classification of Background EEG Signals from ESES Patients and Controls, Zhixian Yang, Yinghua Wang, and Gaoxiang Ouyang
Volume 2014, Article ID 140863, 8 pages

Editorial

Machine Learning for Medical Applications

Huiyu Zhou,¹ Jinshan Tang,² and Huiru Zheng³

¹School of Electronics, Electrical Engineering and Computer Science, The Queen's University of Belfast, Belfast BT9 6AZ, UK

²School of Technology, Michigan Technological University, Houghton, MI 49931, USA

³School of Computing and Mathematics, University of Ulster, Jordanstown Campus, Shore Road, Newtownabbey BT37 0QB, UK

Correspondence should be addressed to Huiyu Zhou; h.zhou@ecit.qub.ac.uk

Received 20 November 2014; Accepted 20 November 2014

Copyright © 2015 Huiyu Zhou et al. This is an open access article distributed under the Creative Commons Attribution License, which permits unrestricted use, distribution, and reproduction in any medium, provided the original work is properly cited.

Machine learning (ML) has been well recognized as an effective tool for researchers to handle the problems in signal and image processing. Machine learning is capable of offering automatic learning techniques to excerpt common patterns from empirical data and then make sophisticated decisions, based on the learned behaviors. Medicine has a large dimensionality of data and the medical application problems frequently make the human-generated, rule-based heuristics intractable. In this special issue, we provide a forum to present the cutting-edge machine learning techniques in medical applications, including the learning of similarities across different image modalities, organ localization, learning of anatomical changes, tissue classification, and computer-aided diagnosis.

The topics of the accepted papers in this Special Issue spread from electroencephalography (EEG) signal processing to image segmentation. Z. Yang et al. in “*Adaptive neuro-fuzzy inference system for classification of background EEG signals from ESES patients and controls*” introduced an adaptive neurofuzzy inference system for classification of background EEG signals from the patients of slow-wave sleep syndrome and control subjects. Their study showed that the entropy measures of EEG were significantly different between the patients and normal subjects. Therefore, a classification framework based on entropy measures was proposed. S. Jirayucharoensak et al. in “*EEG-based emotion recognition using deep learning network with principal component based covariate shift adaptation*” proposed the utilization of a deep learning network (DLN) to discover unknown feature correlation between input signals. The DLN was implemented with a stacked autoencoder (SAE) using hierarchical feature learning approach. D. Al-Jumeily et al. in “*A novel method of early*

diagnosis of Alzheimer's disease based on EEG signals” introduced three neural synchrony measurement techniques: phase synchrony, magnitude squared coherence, and cross correlation for classification of mild Alzheimer's disease patients and healthy subjects. K. Zhang et al. in “*Adaptive bacteria colony picking in unstructured environments using intensity histogram and unascertained LS-SVM classifier*” presented a novel approach for adaptive colony segmentation in unstructured environments by treating the detected peaks of intensity histograms as a morphological feature of images. In order to avoid disturbing peaks, an entropy based mean shift filter was introduced to smooth images as a preprocessing step. The relevance and importance of these features can be determined in an improved support vector machine classifier using unascertained least square estimation. M. Cabrerizo et al. in “*Induced effects of transcranial magnetic stimulation on the autonomic nervous system and the cardiac rhythm*” demonstrated that repetitive transcranial magnetic stimulation (rTMS) could induce changes in the heart rhythm.

Acknowledgments

The guest editors would like to thank all the authors for submitting their high quality manuscripts to this special issue and all the reviewers for providing quality and timely reviews.

Huiyu Zhou
Jinshan Tang
Huiru Zheng

Research Article

A Novel Method of Early Diagnosis of Alzheimer's Disease Based on EEG Signals

Dhiya Al-Jumeily,¹ Shamaila Iram,¹ Francois-Benois Vialatte,²
Paul Fergus,¹ and Abir Hussain¹

¹ Applied Computing Research Group, Liverpool John Moores University, Byrom Street, Liverpool L3 3AF, UK

² Laboratoire SIGMA, ESPCI ParisTech, 14 boulevard des Frères Voisin, 92130 Issy-les-Moulineaux, France

Correspondence should be addressed to Dhiya Al-Jumeily; d.aljumeily@ljamu.ac.uk

Received 4 June 2014; Revised 8 August 2014; Accepted 8 August 2014

Academic Editor: Jinshan Tang

Copyright © 2015 Dhiya Al-Jumeily et al. This is an open access article distributed under the Creative Commons Attribution License, which permits unrestricted use, distribution, and reproduction in any medium, provided the original work is properly cited.

Studies have reported that electroencephalogram signals in Alzheimer's disease patients usually have less synchronization than those of healthy subjects. Changes in electroencephalogram signals start at early stage but, clinically, these changes are not easily detected. To detect this perturbation, three neural synchrony measurement techniques: phase synchrony, magnitude squared coherence, and cross correlation are applied to three different databases of mild Alzheimer's disease patients and healthy subjects. We have compared the right and left temporal lobes of the brain with the rest of the brain areas (frontal, central, and occipital) as temporal regions are relatively the first ones to be affected by Alzheimer's disease. Moreover, electroencephalogram signals are further classified into five different frequency bands (delta, theta, alpha beta, and gamma) because each frequency band has its own physiological significance in terms of signal evaluation. A new approach using principal component analysis before applying neural synchrony measurement techniques has been presented and compared with Average technique. The simulation results indicated that applying principal component analysis before synchrony measurement techniques shows significantly better results as compared to the lateral one. At the end, all the aforementioned techniques are assessed by a statistical test (Mann-Whitney U test) to compare the results.

1. Introduction

Mild cognitive impairment (MCI) is characterized by impaired memory state of brain probably leading towards mild Alzheimer's disease (MiAD) or Alzheimer's disease (AD). This prodromal stage of AD has been under a great influence of research for a long time [1–3]. Statistics reported that 6–25% of MCI is transformed to AD annually and 0.2–4% from healthy person to AD [2, 4], revealing the fact that MCI is a transition state of MiAD and AD.

Loss of functional connectivity between cortical and hippocampus has long been an important focus of researches to examine the cause of cognitive dysfunction in AD [5, 6]. Statistical analysis of interdependence among time series recorded from different brain areas, to study the functional interaction, is called “functional connectivity” [7].

Due to destructive characteristics of AD, it has also been characterized as a neocortical “disconnection syndrome” [8]. The brain's visualization as a complex network of subsystems has led us to find out the factors that can best identify functional disorders in brain [9]. There is now ample evidence that formation of dynamic links in terms of synchronization constitutes the functional integration of the brain [10–12].

Electroencephalogram (EEG) signals are considered functional examples to evaluate cognitive disturbances and a diagnostic tool, especially when a diagnostic doubt exists even after the initial clinical procedures [13, 14]. A great deal of research has already been conducted to detect the fluctuations in EEG signals [2, 5, 15]. Alteration in the regional cerebral blood flow (rCBF) has been considered one of the causes of abnormality in EEG signals of AD [16, 17]. Studies on MCI have shown a decrease of alpha power [18, 19] and an

increase of theta (4–8 Hz) power [20, 21] in corticocortical and subcortical parts of the brain. Babiloni et al. [2] claimed that the reduction of the synchronization likelihood occurs both at interhemispherical (delta-beta2) and frontoparietal (delta-gamma) electrodes.

Topographically analyzing the EEG signals, Hogan et al. [22] reported a less synchronization of upper alpha band between central and temporal cortices. In line, a correlation between higher low-frequency amplitude and alpha-beta activity at frontal region may reflect an early sign of cortical atrophy during the course of AD [23]. Similarly, perturbation in cholinergic inputs from the basal forebrain to cortex and hippocampus indicates a decrease in cortical EEG coherence [24] that can be considered a biomarker for the early detection of AD [2]. Moreover, a combination of multilinear interactions within the tensor formed by multiplying the *subject* \times *frequency* \times *regions* also provides a simple set of features for the interpretation and classification of AD at its early stage [25]. The concept of *local* and *global* methods is used to analyze synchronization between pairs of signals and entire EEG channels at the same time, respectively [15].

The studies, so far, have provided a very limited regional comparison of brain; for instance, less synchronization has been reported between temporal and central regions [22] and also in frontoparietal region [2]. Similarly, functional coupling of EEG rhythms by sensorimotor events is presented only in centroparietal regions of brain [26]. A wider range of study is still required to analyze the synchronization likelihood in all parts of brain (right temporal, left temporal, frontal, central, and occipital) at the same time, on different sets of data for AD.

Synchronization, precisely speaking, is a coordination of “rhythmic oscillators” [27] for a repetitive functional activity, whereas neural synchronization is putatively considered a mechanism where brain regions simultaneously communicate with each other to complete a specific task such as perception, cognition, and action [28, 29]. Any disturbance in the brain, caused by a disease or any other infection, can highly affect the synchronization of brain. Quantitative analysis of EEG signals provides a better insight of synchronization between different parts of brain. For instance, less synchrony has been detected in the EEG signals of AD patients as compared to healthy persons [15].

Various synchrony measurement techniques have already been discussed to detect any perturbation in the EEG signals of AD patients [30]. Both linear such as coherence and nonlinear such as phase synchronization methods are widely used to quantify synchronization in electroencephalographic signals [6, 31, 32]. A comparison of occipital interhemispheric coherence (IHCoh) for normal older adults and AD patients reveals a reduced occipital IHCoh for both lower and higher bands of alpha [33]. Almost similar findings were reported by Locatelli et al. [34] where a significant increase in delta coherence is noticed between frontal and posterior regions in AD patients while a decrease in alpha coherence is shown in temporoparietooccipital areas. Spontaneous phase synchronization of different brain regions is calculated by Kuramoto’s parameter (ρ), which is particularly useful to measure multichannel data [6].

Despite the considerable success of the above mentioned techniques to analyze disruption in the EEG signals of Alzheimer’s patients, further investigations are still required to fulfill the clinical requirements. For instance, in order to detect Alzheimer’s disease at its earlier stages, we need to focus on those areas where Alzheimer’s disease attacks at first and then we need to check its synchronization with the rest of the brain regions. Furthermore, additional novel and comprehensive methods are still required to check the validity of aforementioned techniques on EEG signals.

The above overview suggests that, first, spatial-spectral analysis of EEG signals can provide a measure of memory visualization. Second, neural synchrony measurement techniques have a potential to discriminate between AD patients and healthy subjects. What is still missing or ambiguous in the literature survey is the simultaneous comparison of all parts of brain with the right and left temporal lobes (the most affected parts of brain) to analyze synchronization and also the implementation of new methods to apply synchrony measurement techniques. In this research work, the following novel contributions are considered.

- (i) We have filtered a dataset of MiAD patients into five different frequency bands (delta, theta, alpha, beta, and gamma). For each frequency band, we have computed neural synchronization to compare all parts of brain (frontal, occipital, and central) with left and right temporal lobes.
- (ii) Furthermore, three different sets of MiAD patients are compared to check the validity of our methodology. A high intersubject variability has been seen in the EEG signals of AD patients, especially with different level of severity and comorbidities [25, 35, 36]. Most of the existing studies focus on a single synchrony measure with a single set of data [37]. Also, they apply different measures to different datasets. In this case, it is hard to compare the results to conclude a single hypothesis. To extract a general set of features, we have analysed three different databases, each from one hospital at a time.
- (iii) In order to remove the ambiguity of biased results due to “features redundancy,” we have applied PCA (principal component analysis) technique before applying synchrony measurement techniques. Reducing features vector dimension, commonly known as feature reduction, will help to get accuracy results and avoid overfitting classification [38]. We compare the results with simple Average technique to analyze the pros and cons of the new proposed methodology.

Besthorn et al. [39] applied PCA technique in the quantitative analysis of EEG signals to compress a group of predictor variables to a small set of factors or principle components. Later, they applied linear discriminant classifier to these variables to discriminate AD patients from healthy subjects. Similarly, Uhlhaas et al. [40] applied PCA to remove the artifacts from EEG signals that were generated by eye-blink. To the best of our knowledge and the literature we have surveyed so far, we could not find the application of PCA

to remove the redundant features from the data that can generate a biased result to check the synchronization of brain areas.

Given the exploratory nature of the study, our priori hypothesis is that the proposed methodology would provide a better insight to investigate the decline in the neural synchronization of AD patients. It would provide a better topographical and spectral analysis of the brain regions eliminating the probability of biased result due to feature redundancy.

The rest of this paper is structured as follows. Section 2 provides an overview of our synchrony measurement techniques, the utilized data and the filtering process using five frequency bands, methodology of the proposed technique, and statistical analysis of the results. Sections 3 and 4 are dedicated to discussion and conclusion, respectively.

2. Methods

2.1. Synchrony Measurement Techniques. In this section, we briefly review the synchrony measurement techniques that we have implemented in our datasets which include phase synchrony, cross correlation, and coherence. For this research work, we have selected three synchrony measures from the literature that provides comparatively better results when implemented in EEG signals for the diagnosis of Alzheimer's disease [15]. We use these three synchrony measures to infer which of our proposed methods provides better results in terms of P values. Figure 1 shows the 21 channels used for EEG recording.

2.1.1. Phase Synchrony (Hilbert Transform). The oscillation of two or more cyclic signals where they tend to keep a repeating sequence of relative phase angles is called phase synchronization. Synchronization of two periodic nonidentical oscillators refers to the adjustment of their rhythmicity, that is, the phase locking between the two signals [41, 42]. It refers to the interdependence between the instantaneous phases $\varphi_1(t)$ and $\varphi_2(t)$ of the two signals $s_1(t)$ and $s_2(t)$, respectively. It is usually written as

$$\varphi_{m,n} = m\varphi_1(t) - n\varphi_2(t) = \text{constant}, \quad (1)$$

where m and n are integers indicating the ratio of possible frequency locking and $\varphi_{m,n}$ is their relative phase or phase difference. To compute the phase synchronization, the instantaneous phase of the two signals should be known. This can be detected using analytical signals based on Hilbert transform [9] as follows:

$$z(t) = x(t) + i\tilde{x}(t). \quad (2)$$

Here, $z(t)$ is complex value with $x(t)$ being a real time series and $\tilde{x}(t)$ being its Hilbert transform. The Hilbert transform can be calculated as

$$\tilde{x}(t) = \frac{1}{\pi} \text{PV} \int_{-\infty}^{\infty} \frac{x(\tau)}{t - \tau} dt. \quad (3)$$

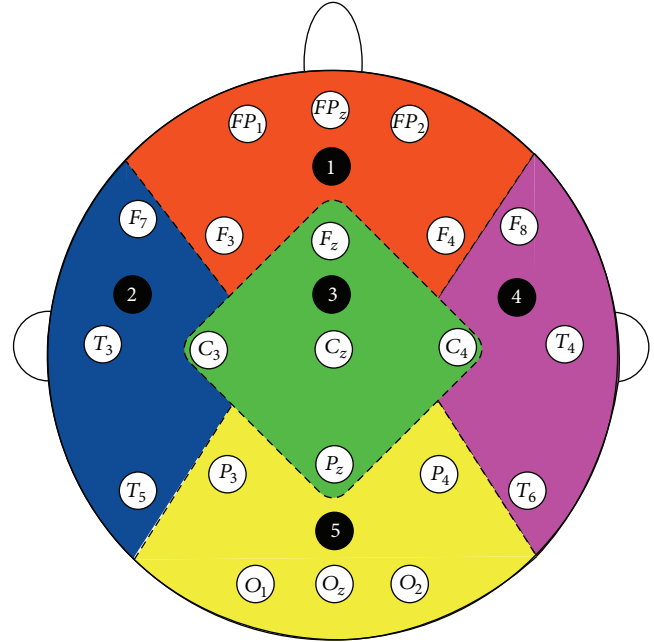


FIGURE 1: The 21 channels used for EEG recording [15].

Here, PV denotes Cauchy principle value. The instantaneous phases $\varphi_1(t)$ and $\varphi_2(t)$ for both signals can be calculated with the following formula:

$$\varphi(t) = \arctan \frac{\tilde{x}(t)}{x(t)}. \quad (4)$$

2.1.2. Cross Correlation. Cross correlation is a mathematical operation used to measure the extent of similarity between two signals. If a signal is correlated to itself, it is called autocorrelated. If we suppose that $x(n)$ and $y(n)$ (why not $s_1(t)$ and $s_2(t)$ make uniform signals suggestion) are two time series, then the correlation between them is calculated as [43]

$$\hat{R}_{xy}(m) = \begin{cases} \sum_{n=0}^{N-m-1} x_{n+m}y_n & m \geq 0 \\ \hat{R}_{yx}(-m) & m < 0. \end{cases} \quad (5)$$

Cross correlation returns a sequence of length $2 * N - 1$ vector, where x and y are of length N vectors ($N > 1$). If x and y are not of the same length, then the shorter vector is zero-padded. Cross correlation returns value between -1 and $+1$. If both signals are identical to each other, the value will be 1; if they are totally different from each other, then the cross correlation coefficient is 0, and if they are identical with the phase shift of 180° , then the cross correlation coefficient will be -1 [15].

2.1.3. Magnitude Squared Coherence. The coherence functions estimate the linear correlation of signals in frequency domain [15]. The magnitude squared coherence is defined as the square of the modulus of the mean cross power spectral density (PSD) normalized to the product of the mean auto

PSDs [44]. The coherence $C_{xy}(f)$ between two channel time series is computed as

$$C_{xy}(f) = \frac{|P_{xy}(f)|}{P_{xx}(f)P_{yy}(f)}, \quad (6)$$

where $P_{xy}(f)$ is the cross PSD estimate of x and y and $P_{xx}(f)$ and $P_{yy}(f)$ are the PSD estimates of x and y , respectively.

For discrete signals x and y , cross power spectral densities ($P_{xy}(f)$) can be calculated with the given formula as follows:

$$P_{xy}(f) = \lim_{T \rightarrow \infty} E \left\{ \left[F_x^T(\omega) \right]^* F_y^T(\omega) \right\}. \quad (7)$$

Here, cross spectral density, which is also known as cross power spectrum, is the Fourier transform of the cross correlation function

$$\begin{aligned} P_{xy}(f) &= \int_{-\infty}^{\infty} R_{xy}(t) e^{-j\omega t} dt \\ &= \int_{-\infty}^{\infty} \left[\int_{-\infty}^{\infty} (x(t)) \cdot y(T+t) dT \right] e^{-j\omega t} dt, \end{aligned} \quad (8)$$

where $R_{xy}(t)$ is the cross correlation of $x(t)$ and $y(t)$. On the other side, autopower spectral densities ($P_{xx}(f)$ and $P_{yy}(f)$) for $x(t)$ and $y(t)$ can be calculated from the autocorrelation instead of cross correlation functions. Consider

$$\begin{aligned} P_{xx}(f) &= \lim_{T \rightarrow \infty} E \left\{ \left[F_x^T(\omega) \right]^* F_x^T(\omega) \right\}, \\ P_{yy}(f) &= \lim_{T \rightarrow \infty} E \left\{ \left[F_y^T(\omega) \right]^* F_y^T(\omega) \right\}. \end{aligned} \quad (9)$$

2.2. Data Description and Data Filtering

2.2.1. Data Description. The datasets that we are analyzing have been recorded from three different countries of European Union. Specialist at the memory clinic referred all patients to the EEG department of the hospital. All patients passed through a number of recommended tests: minimal state examination (MMSE) [45], the Rey Auditory Verbal Learning Test [46], Benton Visual Retention test [47], and memory recall tests [48]. The results are scored and interpreted by psychologists and a multidisciplinary team in the clinic. After that, each patient is referred to hospital for EEG assessment to diagnose the symptoms of AD. Patients were advised to be in a resting state with their eyes closed during the test. The sampling frequency and number of electrodes for three datasets are all different. Detailed information is as follows.

2.2.2. Database A. The EEG dataset A contains 17 MiAD patients (10 males; aged 69.4 ± 11.5 years) and 24 healthy subjects (9 males; aged 77.6 ± 10 years). They all are of British nationality. This data was obtained using a strict protocol from Derriford Hospital, Plymouth, UK, and has been collected using normal hospital practices. EEG signals were obtained using the modified Maudsley system which is similar to the traditional 10–20 international system [49]. EEGs were recorded for 20 sec at a sampling frequency of 256 Hz (later on sampled down to 128 Hz) using 21 electrodes.

2.2.3. Database B. This EEG dataset is composed of 5 MiAD patients (2 males; aged 78.8 ± 5.6 years) as well as 5 healthy subjects (3 males; aged 76.6 ± 10.0 years). They all are of Italian nationality. Several tests, for instance, MMSE, the clinical dementia rating scale (CDRS), and the geriatric depression scale (GDS), were conducted to evaluate the cognitive state of the patients. The MMSE result for healthy subjects is 29.3 ± 0.7 , while for MiAD patients is 22.3 ± 3.1 . EEGs were recorded for 20 sec at a sampling frequency of 128 Hz using 19 electrodes at the University of Malta, Msida MSD06, Malta.

2.2.4. Database C. This dataset consists of 8 MiAD patients (6 males; aged 75 ± 3.4 years) and 3 healthy subjects (3 males; aged 73.5 ± 2.2 years). They all are of Romanian nationality. The AD patients have been referred by a neurologist for EEG recordings. All subjects are diagnosed with AD by means of psychometric tests (MMSE, CDR, and OTS), neuroimaging (CT), and clinical examination (gender, age, disease, duration, education, and medication). The MMSE result for healthy subjects is 28–30, while for MiAD patients it is 20–25. EEG data is recorded using a large equidistant 22-channel arrangement conforming to the international federation of clinical neurophysiology (IFCN) standards [50] for digital recording of clinical EEG from the Ecological University of Bucharest. The time series are recorded for 10 to 20 minutes at a sampling frequency of 512 Hz using 22 electrodes. The signals are notch-filtered at 50 Hz. Further details about the data can be found in [51].

For current research work, we have obtained a version of the data that is already preprocessed of artifacts by using independent component analysis (ICA), a blind source separation technique (BSS). Details of these procedures can be found in [52]. For ICA processed data, the least corrupted 20 s recordings have been selected for further analysis.

2.2.5. Data Filtering into Five Frequency Bands. EEG time series are classified into five frequency bands. Each frequency band has its own physiological significance [6, 53] as follows.

- (i) Delta (δ : $1 \leq f \leq 4$ Hz): these are characterized by deep sleep and are correlated with different pathologies.
- (ii) Theta (θ : $4 \leq f \leq 8$ Hz): these play an important role during childhood. High theta activities in adults are considered abnormal and associated with brain disorders.
- (iii) Alpha (α : $8 \leq f \leq 12$ Hz): these usually appear during mental inactive conditions and under relaxation. They are best seen during closing of eye and mostly pronounced in occipital location.
- (iv) Beta (β : $12 \leq f \leq 25$ Hz): these are visible in central and frontal locations. Their amplitude is less than alpha waves and they are mostly enhanced during tension.
- (v) Gamma (γ : $25 \leq f \leq 30$ Hz): these are best characterized by cognitive and motor functions.

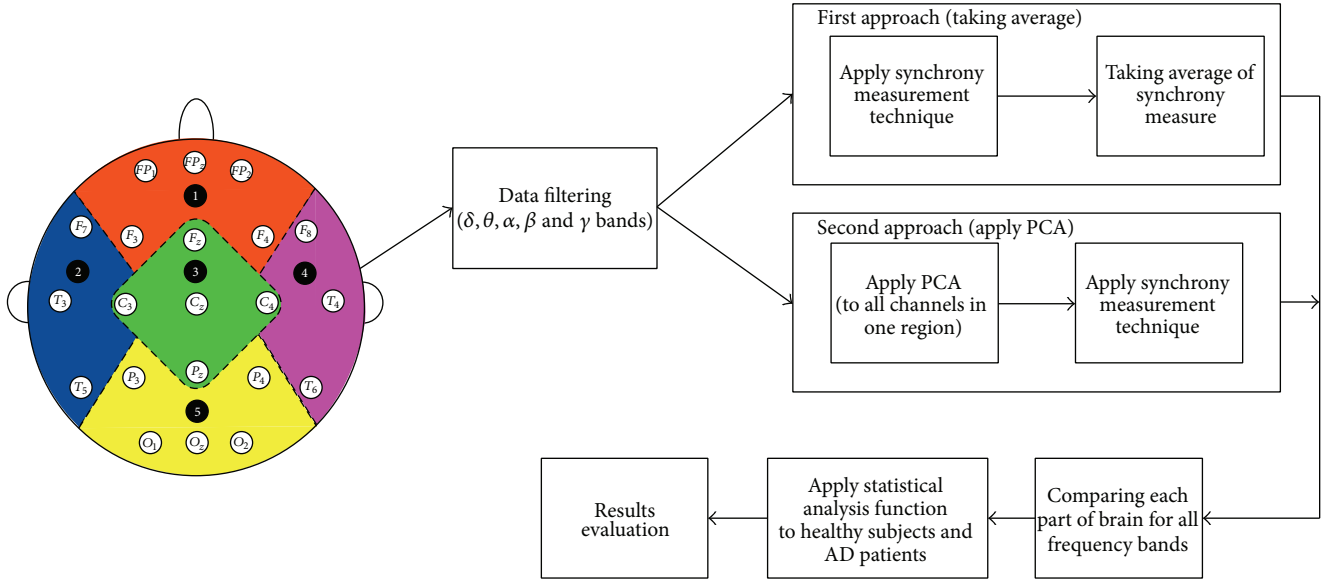


FIGURE 2: Average and PCA methods.

Bandpass filter is applied to each EEG channel to extract the EEG data in specific frequency band $[F: (F + W)]$ Hz. Butterworth filters were used (of 2nd order) as they offer good transition band characteristics at low coefficient orders; thus, they can be implemented efficiently [54].

2.3. Methodology. In this research work, a novel methodology using PCA and neural synchrony measurement of the brain is proposed. We have compared our proposed method with other methods which takes the average of synchrony measures for all channels in one region of the brain. As mentioned previously, we are comparing the right and left temporal lobes with the frontal, central, and occipital areas; so, there are a total of 7 comparisons of the brain ((left temporal-right temporal (LT-RT)), (left temporal-frontal (LT-F)), (left temporal-central (LT-C)), (left temporal-occipital (LT-O)), (right temporal-frontal (RT-F)), (right temporal-central (RT-C)), and (right temporal-occipital (RT-O))) for all frequency bands (δ , θ , α , β , and γ). A brief description of these methods is given below.

2.3.1. First Method (Taking Average of Synchrony Measures for All Channels of One Region). First, we apply neural synchrony measurement techniques to each channel pair (time series of two channels) of two different regions for all frequency bands and then we take the average of those results. For instance, we apply phase synchrony measure to each channel pair of right and left temporal lobes ((F_7-F_8) , (F_7-T_4) , (F_7-T_6) , (T_3-F_8) , (T_3-T_4) , (T_3-T_6) , (T_5-F_8) , (T_5-T_4) , and (T_5-T_6)) and then we take the average result of right temporal-left temporal. We compare the left temporal lobe with the frontal (FP_1 , FP_2 , FP_z , F_3 , and F_4), central (F_z , C_3 , C_z , C_4 , and P_z), and occipital (P_3 , P_4 , O_1 , O_2 , and O_z) areas. Similarly, we compare the right temporal lobe (F_8 , T_4 , and T_6) to the rest of the brain area. The same technique has been

used for the rest of the synchrony measures, that is, cross correlation and coherence.

After getting the results, we compare the neural synchronization of AD patients and healthy subjects, for all three measurement techniques (phase synchronization, cross correlation, and coherence), by Mann-Whitney U test. Figure 2 shows all the steps of our Average method.

2.3.2. Second Method (PCA Based Neural Synchrony Measure). In this method, instead of applying synchrony measurement techniques directly to the filtered data, first we apply principal component analysis (PCA) technique to all channels of one. This eliminates any redundant information that a region could provide. For instance, we apply PCA to all three channels of left temporal lobe (F_7 , T_3 , and T_5) and consequently it provides a single signal without any redundant information. Then, we apply PCA to all channels of right temporal lobe (F_8 , T_4 , and T_6). After that, we apply synchrony measure to these two regions. Similarly, we apply PCA to all other channels of a region: frontal (FP_1 , FP_2 , FP_z , F_3 , and F_4), central (F_z , C_3 , C_z , C_4 , and P_z), and occipital (P_3 , P_4 , O_1 , O_2 , and O_z) and compute the synchrony measure with left and right temporal lobes. The rest of the procedure is similar to the first proposed method.

2.3.3. Principal Component Analysis (PCA). The basic purpose of PCA is to reduce the dimensionality of a dataset to convert it to uncorrelated variables providing maximum information about a data while eliminating interrelated variables. In other words, it transforms the highly dimensional dataset (of m dimensions) into low dimensional orthogonal features (of n dimension) where $n < m$ [55].

In our case, we apply PCA to all channels in one particular region, for instance, the application of PCA for the left temporal lobe as shown in Figure 3(a) using channel

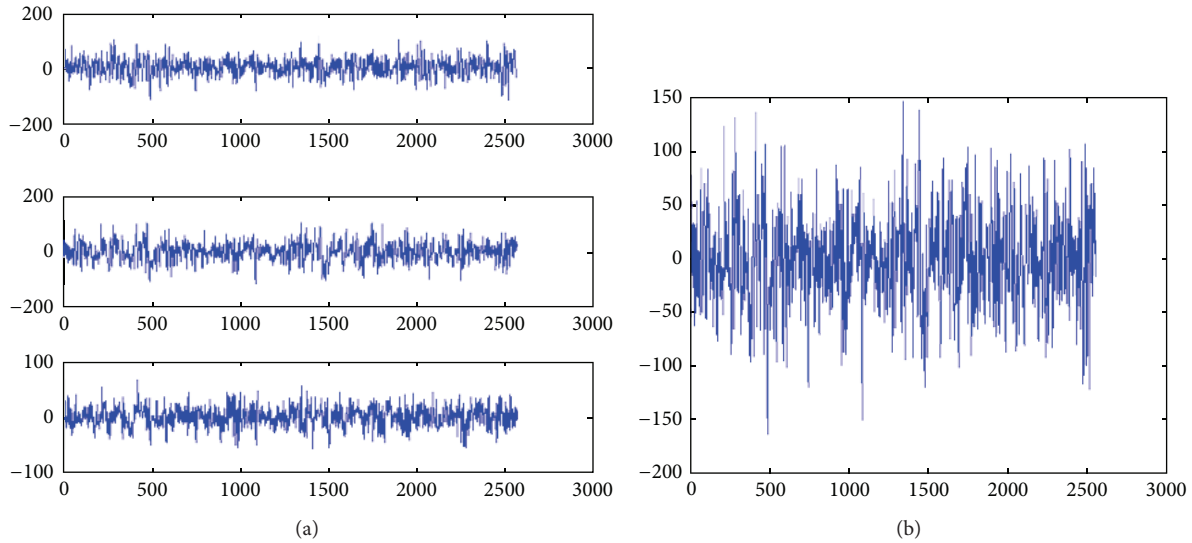


FIGURE 3: Application of PCA on left temporal lobe channels signals.

(F_7 , T_3 , T_5) are converted into a single signal as shown in Figure 3(b). The generated temporal signal contains almost all information from the left temporal lobe while eliminating any redundant information.

2.4. Statistical Analysis. To investigate whether there is a significant difference between the EEG signals of MiAD patients and the control subjects and also to prove the probable significance of our proposed methodology, we apply the Wilcoxon rank sum (Mann-Whitney) test [56, 57] to our datasets. A rank sum function is a nonparametric test which allows us to check whether the statistics at hand, in our case synchrony results, take different values from two different populations. Lower P values indicate higher significance in terms of large difference in medians of two populations [15].

Since we are applying three different synchrony measures to three different sets of data, first we consider our first proposed method (taking average of synchrony values) to compute the synchrony measure. We apply all three measures for all 7 different comparisons of brain for all frequency bands and compute the results by Mann-Whitney test. Then, we apply the same techniques on all, above mentioned, three datasets using the second proposed method (PCA based synchrony measures). This will enable us to compare our results in two different perspectives as follows.

- (i) Investigating three different synchrony measures at a time will help us to compare which measure works better for EEG signals.
- (ii) Secondly, we are able to compare two different methods for three synchrony measures using three different datasets.

In addition to evaluating the statistical significance of our proposed method, this will also help us to differentiate the MiAD patients from healthy subjects.

3. Results and Discussions

The aim of the present study is to find the relationship of EEG synchronization with AD and thus to explore further dimensions in disconnection theorem of cognitive dysfunction in AD and also to investigate a better method to detect any changes in EEG synchrony that can be considered a biomarker for the early detection of AD. Here, we investigate and discuss results in two different angles. First, we discuss the role of synchrony measures to examine a change in EEG synchrony in MiAD patients and later we confer the significance of applying PCA before synchrony measures.

3.1. Functional Disconnection of Brain Regions due to Lower Synchronization. We have observed that all of the synchrony measures, tested in this paper, show a decrease in EEG synchrony for MiAD patients as compared to healthy subjects. However, cross correlation shows a higher number of significant results at the $P = 0.01$ level as compared to phase synchrony and coherence. We have examined mostly the areas that have shown less functional connectivity for all three synchrony measures, which are; right temporal-central (RT-C) for delta, theta, and alpha bands and also left temporal-occipital (LT-O) for delta and alpha bands. The rest of this paper discusses these two regions where we find highly significant results compared to the rest of the regions.

First, we discuss *dataset A* for all three synchrony measures with PCA based method. The P values for cross correlation in RT-C region are 2.47×10^{-4} , 1.46×10^{-4} , and 0.009 for delta, theta, and alpha bands, respectively. In LT-O region, the smallest P values for delta and theta bands are 8.50×10^{-5} and 6.8×10^{-5} , respectively. The 2nd best measure which has given us remarkable results is phase synchrony, where we get 0.0067, 0.0403, and 0.0585 P values for delta, theta, and alpha bands, respectively, in RT-C region. We get 0.0041 and 0.0271 P values for delta and alpha bands in LT-O region. Lastly, the coherence function shows significant

results in RT-C region for delta band, P value = 0.0378, and in LT-O 9.8×10^{-4} and 0.05 for delta and alpha bands, respectively. Coherence function does not provide significant results and hence contradicts Bahar theory [58] where control group showed higher values of evoked coherence in delta, theta, and alpha bands in the left frontoparietal electrode pairs as compared to AD patients.

Lower P values at delta and alpha bands are shown by Babiloni et al. [2] at frontoparietal couplings of electrodes which indicates a lower synchronization in MCI and AD subjects. Further to the previous findings, our results show a higher difference of synchronization for temporal, occipital, and central areas in MiAD patients at delta, theta, and alpha levels. They show lower magnitudes of delta, theta, and alpha bands in temporal, central, and occipital areas in MiAD patients than the compared healthy subjects. Temporal regions are characterized by short term and long term memory and any neuronal change on these sites is a clear indication of progression of AD.

Interestingly, we find a decrease in alpha band synchronization for all three synchrony measures in almost all regions. For instance, for cross correlation, P value < 0.01 in almost all parts of the brain; for phase synchrony, the P values are 0.058, 0.0038, 0.011, and 0.027 in RT-C, RT-O, RT-F, and LT-O, respectively. This shows the importance of alpha rhythm for the early detection of AD which is in accordance with the phenomena that alpha rhythms are mainly modulated by thalamocortical and corticocortical systems [56, 57]. Alpha band is mainly related to subjects global attentional readiness and engagement of specific neural channels for the elaboration of sensorimotor or semantic information [2].

As aforementioned, mostly the areas that show lower dysfunctional connectivity are right temporal-central and left temporal-occipital. A lower synchronization in these connections, especially in RT-C region, for alpha band indicates a disturbance in the perception and integration of somatosensory information, visuospatial processing, and cognitive disorder. This information is in line with clinical findings presented in [59] for increasing visual and spatial deficits in MCI and MiAD patients. Table 1 shows the significant P values in different parts of the brain in different frequency bands for *dataset A*.

Similarly, for *dataset B* and *dataset C*, we found low P values in the same regions for same frequency bands but not as much significant as for *dataset A*. One thing in common in all three datasets is that they show lower P values in alpha frequency bands in the RT-C region. Table 2 shows the total number of significant values in case of PCA and Average method.

3.2. Significance of PCA Approach over Average Approach. Our second hypothesis was to show the significance of using PCA techniques to eliminate the redundant information from the data that can give biased results, before applying synchrony measures. As expected, we found a big difference in results with and without PCA method. We have found that more than 90% of the values are better in case of PCA method as compared to Average method for all of three datasets.

TABLE 1: P values for *dataset A*, different frequency bands in different brain connections.

Synchrony measure	Brain connections	Frequency regions	P values	
Cross correlation	RT-C	Delta (δ)	2.47×10^{-4}	
		Theta (θ)	1.46×10^{-4}	
		Alpha (α)	0.009	
	RT-O	Delta (δ)	6.9×10^{-5}	
		Theta (θ)	2.7×10^{-5}	
		Alpha (α)	0.0029	
	RT-F	Delta (δ)	5.01×10^{-4}	
		Theta (θ)	6.8×10^{-5}	
		Alpha (α)	0.0062	
	LT-C	Delta (δ)	Delta (δ)	4.3×10^{-5}
			Theta (θ)	3.8×10^{-5}
			Alpha (α)	0.0192
		LT-O	Delta (δ)	8.5×10^{-5}
			Theta (θ)	6.8×10^{-5}
			Alpha (α)	0.0052
		LT-F	Delta (δ)	2.2×10^{-4}
			Theta (θ)	5.4×10^{-5}
			Alpha (α)	0.0091
LT-RT	Delta (δ)	3.3×10^{-4}		
	Theta (θ)	6×10^{-5}		
	Alpha (α)	0.0253		
Phase synchrony	RT-C	Delta (δ)	0.0067	
		Theta (θ)	0.0403	
		Alpha (α)	0.05	
	RT-O	Delta (δ)	0.0041	
		Alpha (α)	0.0271	
Coherence	RT-C	Delta (δ)	0.0378	
		Delta (δ)	0.0378	
	RT-O	Alpha (α)	0.0192	

TABLE 2: Total number of significant values in case of PCA and Average method.

Synchrony measure	Method	$P < 0.01$ (Total values)	$P < 0.05$ (Total values)
Cross correlation	PCA	26	35
	Average	22	30
Phase synchrony	PCA	8	11
	Average	2	8

For instance, for *dataset A*, in case of PCA method, we have found 8 significant values below 0.01 ($P < 0.01$) and 11 significant values below 0.05 ($P < 0.05$), while only 2 values below 0.01 ($P < 0.01$) and 8 values below 0.05 ($P < 0.05$) in case of Average method for phase synchrony measure were found. Similarly, for cross correlation measures, although the difference is not very high, yet the PCA method has shown more significant values. For example, the number of P values

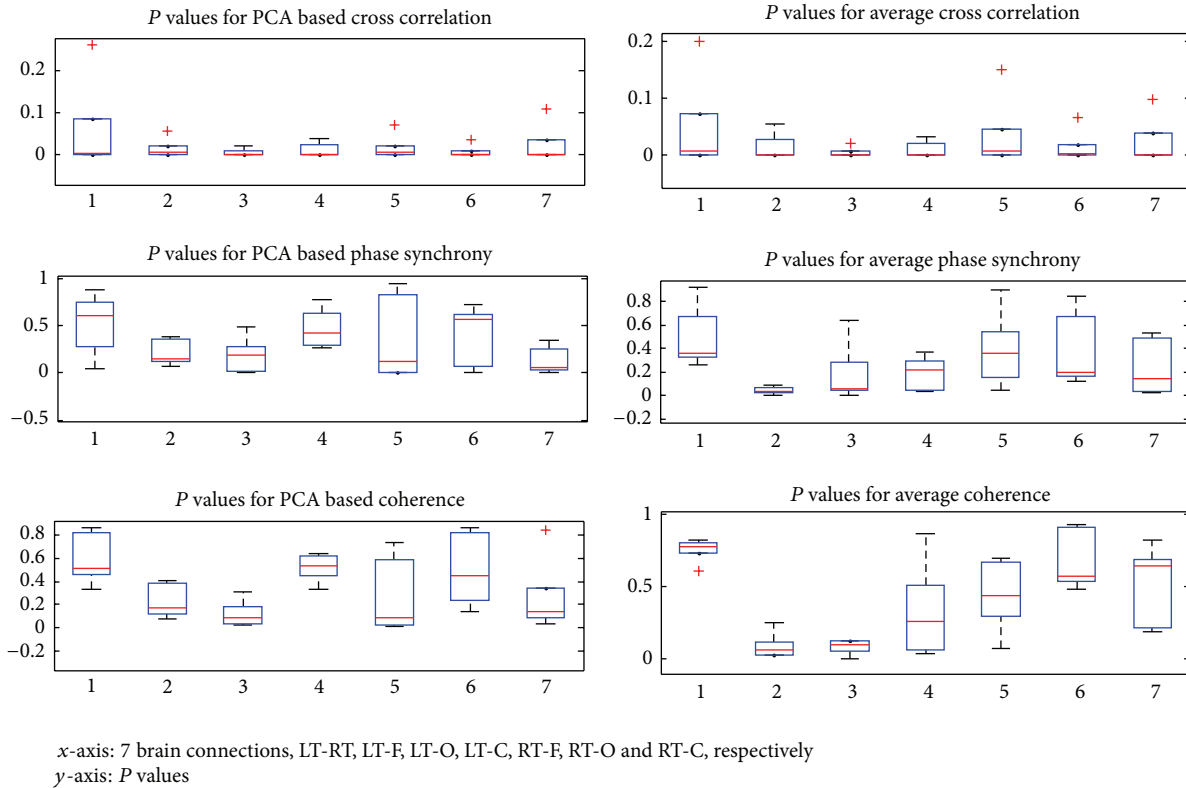


FIGURE 4: Boxplots show the results of three synchrony measures for PCA and Average methods.

below 0.01 ($P < 0.01$) is 26, while almost all 35 values were below 0.05 ($P < 0.05$); for Average method 22 values are below 0.01 and 30 values are below 0.05 ($P < 0.05$). As aforementioned, coherence function does not perform better as compared to other two synchrony measures but again we found more significant results in case of PCA method as compared to the Average method.

The results are also shown by boxplot in Figure 4 that show the difference of P values for all three synchrony measures in all 7 brain comparisons for *dataset A*. They compare the results of synchrony measures for PCA and Average methods.

Similarly, for *dataset B* and *dataset C*, the results of PCA method are more significant as compared to Average method. This clearly shows that using PCA method before synchrony measures has two advantages as follows.

- (i) As the redundant information is eliminated from the datasets, the results are not biased and are more reliable.
- (ii) Secondly, it proves that application of PCA generates more significant results as compared to average synchrony measure method.

4. Conclusion

The aim of the current study was to show the significance of applying PCA method to eliminate redundant information from the datasets to get more reliable results. In this study,

three different datasets were selected with different specifications and three different synchrony measures are applied to prove the significance of our approach. Moreover, we have compared our proposed method with Average methods to compute synchronization in MiAD patients as well as in control subjects.

Results revealed that cross correlation measure showed higher difference in synchronization of MiAD and control subjects as compared to phase synchrony, while coherence function did not perform very well. They have also indicated that alpha and theta bands play a major role in identifying the change in synchronization from MiAD and control subjects especially in right temporal-central region (RT-C) and also in left temporal-occipital (LT-O) region.

Furthermore, the original contribution of this research work is the comparison of previous methods of applying synchrony measures with PCA based method. Our proposed method proved the importance of eliminating redundant information, from EEG time series, that may come from consecutive electrodes. It should be noted that comparison with previous findings is problematic due to the significant differences in the utilized methodology and the utilization of different kinds of synchrony measures on different kinds of datasets. However, our results are consistent with most of the studies on the loss of average EEG synchrony in different parts of the brain for MiAD patients and are also in accordance with the clinical findings.

Furthermore, we have successfully shown the importance and significance of our proposed method, to detect lower

synchronization in MiAD patients, as compared to the Average method for all three datasets.

Future work will involve the study of much significant results of lower synchronization in case of *dataset B* and *dataset C* as compared to *dataset A*. In this paper, we have implemented PCA to eliminate the redundant and irrelevant information from the EEG signals and also applied signal processing techniques to extract the features that are useful for the early diagnosis of Alzheimer's disease. In this ongoing research project, the next step is the implementation of classification algorithms to recognize the data patterns that can be used for the identification and diagnosis of Alzheimer's disease in clinics.

Conflict of Interests

The authors declare that there is no conflict of interests regarding the publication of this paper.

References

- [1] J. Rogers, S. Webster, L.-F. Lue et al., "Inflammation and Alzheimer's disease pathogenesis," *Neurobiology of Aging*, vol. 17, no. 5, pp. 681–686, 1996.
- [2] C. Babiloni, R. Ferri, G. Binetti et al., "Fronto-parietal coupling of brain rhythms in mild cognitive impairment: a multicentric EEG study," *Brain Research Bulletin*, vol. 69, no. 1, pp. 63–73, 2006.
- [3] C. Babiloni, G. B. Frisoni, M. Pievani et al., "Hippocampal volume and cortical sources of EEG alpha rhythms in mild cognitive impairment and Alzheimer disease," *NeuroImage*, vol. 44, no. 1, pp. 123–135, 2009.
- [4] G. B. Frisoni, A. Padovani, and L.-O. Wahlund, "The pre-dementia diagnosis of Alzheimer disease," *Alzheimer Disease and Associated Disorders*, vol. 18, no. 2, pp. 51–53, 2004.
- [5] B. Jelles, P. Scheltens, W. M. van der Flier, E. J. Jonkman, F. H. L. da Silva, and C. J. Stam, "Global dynamical analysis of the EEG in Alzheimer's disease: frequency-specific changes of functional interactions," *Clinical Neurophysiology*, vol. 119, no. 4, pp. 837–841, 2008.
- [6] M. C. Faustino, R. P. Serquiña, P. E. Rapp, and A. M. Albano, "Phase synchronization of electroencephalographic signals in the different frequency bands," *Philippine Science Letters*, vol. 5, pp. 131–137, 2012.
- [7] A. A. Fingelkurts and S. Kähkönen, "Functional connectivity in the brain—is it an elusive concept?" *Neuroscience and Biobehavioral Reviews*, vol. 28, no. 8, pp. 827–836, 2005.
- [8] X. Delbeuck, M. van der Linden, and F. Collette, "Alzheimer's disease as a disconnection syndrome?" *Neuropsychology Review*, vol. 13, no. 2, pp. 79–92, 2003.
- [9] C. J. Stam, G. Nolte, and A. Daffertshofer, "Phase lag index: assessment of functional connectivity from multi channel EEG and MEG with diminished bias from common sources," *Human Brain Mapping*, vol. 28, no. 11, pp. 1178–1193, 2007.
- [10] W. Singer, "Neuronal synchrony: a versatile code for the definition of relations?" *Neuron*, vol. 24, no. 1, pp. 49–65, 1999.
- [11] P. Fries, "A mechanism for cognitive dynamics: Neuronal communication through neuronal coherence," *Trends in Cognitive Sciences*, vol. 9, no. 10, pp. 474–480, 2005.
- [12] F. Varela, J. P. Lachaux, E. Rodriguez, and J. Martinerie, "The brainweb: phase synchronization and large-scale integration," *Nature Reviews Neuroscience*, vol. 2, no. 4, pp. 229–239, 2001.
- [13] J. J. Claus, R. L. M. Strijers, E. J. Jonkman et al., "The diagnostic value of electroencephalography in mild senile Alzheimer's disease," *Clinical Neurophysiology*, vol. 110, no. 5, pp. 825–832, 1999.
- [14] E. Gallego-Jutgla, M. Elgendi, F. Vialatte et al., "Diagnosis of Alzheimer's disease from EEG by means of synchrony measures in optimized frequency bands," in *Proceedings of the International Conference of the IEEE Engineering in Medicine and Biology Society (EMBC '12)*, pp. 4266–4270, 2012.
- [15] J. Dauwels, F. Vialatte, and A. Cichocki, "A comparative study of synchrony measures for the early diagnosis of Alzheimer's disease based on EEG," in *Neural Information Processing*, vol. 4984, pp. 112–125, Springer, Berlin, Germany, 2008.
- [16] G. Johannesson, A. Brun, I. Gustafson, and D. H. Ingvar, "EEG in presenile dementia related to cerebral blood flow and autopsy findings," *Acta Neurologica Scandinavica*, vol. 56, no. 2, pp. 89–103, 1977.
- [17] B. Szelies, M. Grond, K. Herholz, J. Kessler, T. Wullen, and W.-D. Heiss, "Quantitative EEG mapping and PET in Alzheimer's disease," *Journal of the Neurological Sciences*, vol. 110, no. 1-2, pp. 46–56, 1992.
- [18] C. Huang, L.-O. Wahlund, T. Dierks, P. Julin, B. Winblad, and V. Jelic, "Discrimination of Alzheimer's disease and mild cognitive impairment by equivalent EEG sources: a cross-sectional and longitudinal study," *Clinical Neurophysiology*, vol. 111, no. 11, pp. 1961–1967, 2000.
- [19] M. Grunwald, F. Busse, A. Hensel et al., "Correlation between cortical θ activity and hippocampal volumes in health, mild cognitive impairment, and mild dementia," *Journal of Clinical Neurophysiology*, vol. 18, no. 2, pp. 178–184, 2001.
- [20] L. C. Fonseca, G. M. A. S. Tedrus, L. R. Prandi, and A. C. A. de Andrade, "Quantitative electroencephalography power and coherence measurements in the diagnosis of mild and moderate Alzheimer's disease," *Arquivos de Neuro-Psiquiatria*, vol. 69, pp. 297–303, 2011.
- [21] C. J. Stam, B. F. Jones, I. Manshanden et al., "Magnetoencephalographic evaluation of resting-state functional connectivity in Alzheimer's disease," *NeuroImage*, vol. 32, no. 3, pp. 1335–1344, 2006.
- [22] M. J. Hogan, G. R. J. Swanwick, J. Kaiser, M. Rowan, and B. Lawlor, "Memory-related EEG power and coherence reductions in mild Alzheimer's disease," *International Journal of Psychophysiology*, vol. 49, no. 2, pp. 147–163, 2003.
- [23] T. Dierks, R. Ihl, L. Frolich, and K. Maurer, "Dementia of the Alzheimer type: effects on the spontaneous EEG described by dipole sources," *Psychiatry Research: Neuroimaging*, vol. 50, no. 3, pp. 151–162, 1993.
- [24] M. Mesulam, "The cholinergic lesion of Alzheimer's disease: pivotal factor or side show?" *Learning and Memory*, vol. 11, no. 1, pp. 43–49, 2004.
- [25] C.-F. V. Latchoumane, F. Vialatte, A. Cichocki, and J. Jeong, "Multiway analysis of Alzheimer's disease: classification based on space-frequency characteristics of EEG time series," in *Proceedings of the World Congress on Engineering*, London, UK, 2008.
- [26] C. Babiloni, A. Brancucci, F. Vecchio, L. Arendt-Nielsen, A. C. N. Chen, and P. M. Rossini, "Anticipation of somatosensory and

- motor events increases centro-parietal functional coupling: an EEG coherence study," *Clinical Neurophysiology*, vol. 117, no. 5, pp. 1000–1008, 2006.
- [27] K. Yun, K. Watanabe, and S. Shimojo, "Interpersonal body and neural synchronization as a marker of implicit social interaction," *Scientific Reports*, vol. 2, article 959, 2012.
- [28] L. M. Ward, "Synchronous neural oscillations and cognitive processes," *Trends in Cognitive Sciences*, vol. 7, no. 12, pp. 553–559, 2003.
- [29] L. M. Ward, S. E. MacLean, and A. Kirschner, "Stochastic resonance modulates neural synchronization within and between cortical sources," *PLoS ONE*, vol. 5, no. 12, Article ID e14371, 2010.
- [30] J. Dauwels, F. Vialatte, and A. Cichocki, "Diagnosis of Alzheimer's disease from EEG signals: where are we standing?" *Current Alzheimer Research*, vol. 7, no. 6, pp. 487–505, 2010.
- [31] M. Breakspear, "Nonlinear phase desynchronization in human electroencephalographic data," *Human Brain Mapping*, vol. 15, no. 3, pp. 175–198, 2002.
- [32] A. Bruns, "Fourier-, Hilbert- and wavelet-based signal analysis: are they really different approaches?" *Journal of Neuroscience Methods*, vol. 137, no. 2, pp. 321–332, 2004.
- [33] R. Anghinah, P. A. M. Kanda, M. S. Jorge, E. E. P. de Lima, L. Pascuzzi, and A. C. P. de Melo, "Alpha hand coherence analysis of EEG in healthy adult and Alzheimer's type dementia subjects," *Arquivos de Neuro-Psiquiatria*, vol. 58, no. 2A, pp. 272–275, 2000.
- [34] T. Locatelli, M. Cursi, D. Liberati, M. Franceschi, and G. Comi, "EEG coherence in Alzheimer's disease," *Electroencephalography and Clinical Neurophysiology*, vol. 106, no. 3, pp. 229–237, 1998.
- [35] F. Nobili, F. Copello, P. Vitali et al., "Timing of disease progression by quantitative EEG in Alzheimer's patients," *Journal of Clinical Neurophysiology*, vol. 16, no. 6, pp. 566–573, 1999.
- [36] E. Pucci, N. Belardinelli, G. Cacchiò, M. Signorino, and F. Angeleri, "EEG power spectrum differences in early and late onset forms of Alzheimer's disease," *Clinical Neurophysiology*, vol. 110, no. 4, pp. 621–631, 1999.
- [37] J. Dauwels, F. Vialatte, C. Latchoumane, J. Jeong, and A. Cichocki, "EEG synchrony analysis for early diagnosis of Alzheimer's disease: a study with several synchrony measures and EEG data sets," *IEEE Engineering in Medicine and Biology Society*, vol. 2009, pp. 2224–2227, 2009.
- [38] F. Abdollahi and A. Motie-Nasrabadi, "Combination of frequency bands in EEG for feature reduction in mental task classification," in *Proceedings of the 28th Annual International Conference of the IEEE Engineering in Medicine and Biology Society (EMBS '06)*, pp. 1146–1149, New York, NY, USA, September 2006.
- [39] C. Besthorn, R. Zerfass, C. Geiger-Kabisch et al., "Discrimination of Alzheimer's disease and normal aging by EEG data," *Electroencephalography and Clinical Neurophysiology*, vol. 103, no. 2, pp. 241–248, 1997.
- [40] P. J. Uhlhaas, F. Roux, W. Singer, C. Haenschel, R. Sireteanu, and E. Rodriguez, "The development of neural synchrony reflects late maturation and restructuring of functional networks in humans," *Proceedings of the National Academy of Sciences of the United States of America*, vol. 106, no. 24, pp. 9866–9871, 2009.
- [41] M. le van Quyen, J. Foucher, J.-P. Lachaux et al., "Comparison of Hilbert transform and wavelet methods for the analysis of neuronal synchrony," *Journal of Neuroscience Methods*, vol. 111, no. 2, pp. 83–98, 2001.
- [42] P. Tass, M. G. Rosenblum, J. Weule et al., "Detection of n:m phase locking from noisy data: application to magnetoencephalography," *Physical Review Letters*, vol. 81, no. 15, pp. 3291–3294, 1998.
- [43] S. Chandaka, A. Chatterjee, and S. Munshi, "Cross-correlation aided support vector machine classifier for classification of EEG signals," *Expert Systems with Applications*, vol. 36, no. 2, pp. 1329–1336, 2009.
- [44] A. Ozerdem, B. Güntekin, E. Saatçi, Z. Tunca, and E. Başar, "Disturbance in long distance gamma coherence in bipolar disorder," *Progress in neuro-psychopharmacology & biological psychiatry*, vol. 34, no. 6, pp. 861–865, 2010.
- [45] M. F. Folstein, S. E. Folstein, and P. R. McHugh, "Mini-mental state: A practical method for grading the cognitive state of patients for the clinician," *Journal of Psychiatric Research*, vol. 12, no. 3, pp. 189–198, 1975.
- [46] H. S. Levin, "A compendium of neuropsychological tests: administration, norms, and commentary," *Archives of Neurology*, vol. 50, pp. 451–451, 1993.
- [47] A. L. Benton, *The Revised Visual Retention Test: Clinical and Experimental Applications*, The Psychological Corporation, New York, NY, USA, 1963.
- [48] G. A. Talland and M. Ekdahl, "Psychological studies of Korsakoff's psychosis: IV. The rate and mode of forgetting narrative material," *The Journal of Nervous and Mental Disease*, vol. 129, pp. 391–404, 1959.
- [49] R. W. Homan, J. Herman, and P. Purdy, "Cerebral location of international 10–20 system electrode placement," *Electroencephalography and Clinical Neurophysiology*, vol. 66, no. 4, pp. 376–382, 1987.
- [50] M. R. Nuwer, G. Comi, R. Emerson et al., "IFCN standards for digital recording of clinical EEG," *Electroencephalography and Clinical Neurophysiology*, vol. 106, no. 3, pp. 259–261, 1998.
- [51] C.-F. V. Latchoumane, F.-B. Vialatte, J. Solé-Casals et al., "Multiway array decomposition analysis of EEGs in Alzheimer's disease," *Journal of Neuroscience Methods*, vol. 207, no. 1, pp. 41–50, 2012.
- [52] F.-B. Vialatte, J. Solé-Casals, M. Maurice et al., "Improving the quality of EEG Data in patients with Alzheimer's disease using ICA," in *Advances in Neuro-Information Processing*, M. Köppen, N. K. Kasabov, and G. G. Coghill, Eds., pp. 979–986, Springer, Berlin, Germany, 2009.
- [53] R. Q. Quiroga, *Quantitative analysis of EEG signals: time-frequency methods and Chaos theory [Ph.D. thesis]*, Institute of Signal Processing, Medical University of Lübeck, 1998.
- [54] A. V. Oppenheim, R. W. Schaffer, and J. R. Buck, *Discrete-Time Signal Processing (2nd ed.)*, Prentice-Hall, New York, NY, USA, 1999.
- [55] U. Rajendra Acharya, S. Vinitha Sree, A. P. C. Alvin, and J. S. Suri, "Use of principal component analysis for automatic classification of epileptic EEG activities in wavelet framework," *Expert Systems with Applications*, vol. 39, no. 10, pp. 9072–9078, 2012.
- [56] C. H. M. Brunia, "Neural aspects of anticipatory behavior," *Acta Psychologica*, vol. 101, no. 2-3, pp. 213–242, 1999.
- [57] C. Jack, "A wilcoxon-type test for trend," *Statistics in Medicine*, vol. 4, no. 4, pp. 543–547, 1985.

- [58] B. Güntekin, E. Saatçi, and G. Yener, "Decrease of evoked delta, theta and alpha coherences in Alzheimer patients during a visual oddball paradigm," *Brain Research*, vol. 1235, pp. 109–116, 2008.
- [59] E. Arnáiz and O. Almkvist, "Neuropsychological features of mild cognitive impairment and preclinical Alzheimer's disease," *Acta Neurologica Scandinavica*, vol. 107, no. 179, pp. 34–41, 2003.

Research Article

EEG-Based Emotion Recognition Using Deep Learning Network with Principal Component Based Covariate Shift Adaptation

Suwicha Jirayucharoensak,^{1,2} Setha Pan-Ngum,¹ and Pasin Israsena²

¹ Department of Computer Engineering, Faculty of Engineering, Chulalongkorn University, Bangkok 10330, Thailand

² National Electronics and Computer Technology Center, Thailand Science Park, Khlong Luang, Pathum Thani 12120, Thailand

Correspondence should be addressed to Setha Pan-Ngum; setha.p@chula.ac.th

Received 2 May 2014; Revised 30 July 2014; Accepted 30 July 2014; Published 1 September 2014

Academic Editor: Jinshan Tang

Copyright © 2014 Suwicha Jirayucharoensak et al. This is an open access article distributed under the Creative Commons Attribution License, which permits unrestricted use, distribution, and reproduction in any medium, provided the original work is properly cited.

Automatic emotion recognition is one of the most challenging tasks. To detect emotion from nonstationary EEG signals, a sophisticated learning algorithm that can represent high-level abstraction is required. This study proposes the utilization of a deep learning network (DLN) to discover unknown feature correlation between input signals that is crucial for the learning task. The DLN is implemented with a stacked autoencoder (SAE) using hierarchical feature learning approach. Input features of the network are power spectral densities of 32-channel EEG signals from 32 subjects. To alleviate overfitting problem, principal component analysis (PCA) is applied to extract the most important components of initial input features. Furthermore, covariate shift adaptation of the principal components is implemented to minimize the nonstationary effect of EEG signals. Experimental results show that the DLN is capable of classifying three different levels of valence and arousal with accuracy of 49.52% and 46.03%, respectively. Principal component based covariate shift adaptation enhances the respective classification accuracy by 5.55% and 6.53%. Moreover, DLN provides better performance compared to SVM and naive Bayes classifiers.

1. Introduction

Brain-computer interface (BCI) has been one of the most interesting biomedical engineering research fields for decades. It provides a promising technology allowing humans to control external devices by modulating their brain waves. Most BCI applications have been developed for noninvasive brain signal processing which is practical to implement in real-world scenarios. There are plenty of successful EEG-based BCI applications such as word speller programs [1] and wheelchair controllers [2]. Not only can BCI be employed to mentally control devices, but also it can be implemented for understanding our mental states. Emotion recognition is one of such applications. Automatic emotion recognition algorithms potentially bridge the gap between human and machine interactions.

A model of emotion can be characterized by two main dimensions called valence and arousal. The valence is the degree of attraction or aversion that an individual feels toward

a specific object or event. It ranges from negative to positive. The arousal is a physiological and psychological state of being awake or reactive to stimuli, ranging from passive to active. The valence-arousal dimensional model, represented in Figure 1, of emotion is widely used in many research studies.

Electroencephalogram (EEG) is a record of the oscillation of brain electric potentials resulting from ionic current flow between brain neurons. EEG signals are acquired by measuring the electrical activities at electrode's positions on the scalp. The 10–20 system [3] of electrode placement, illustrated in Figure 2, provides an international system to ensure standardized reproducibility. By referring to 10–20 system, a subject's studies could be compared over time and subjects could be compared to each other. Human's brain wave is the composition of five main frequency bands called delta (1–3 Hz), theta (4–7 Hz), alpha (8–13 Hz), beta (14–30 Hz), and gamma (31–50 Hz), as shown in Figure 3. The characteristics of each band can be utilized to estimate subject's cognition and emotion states.

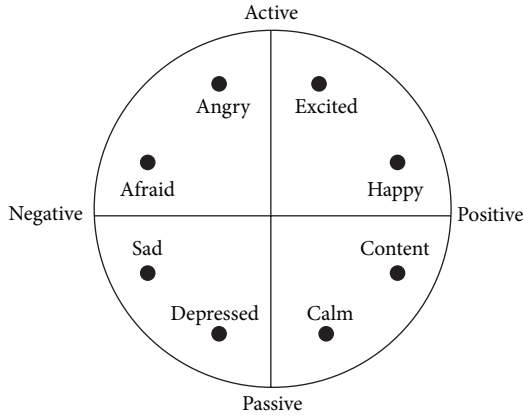


FIGURE 1: Valence-arousal dimensional model.

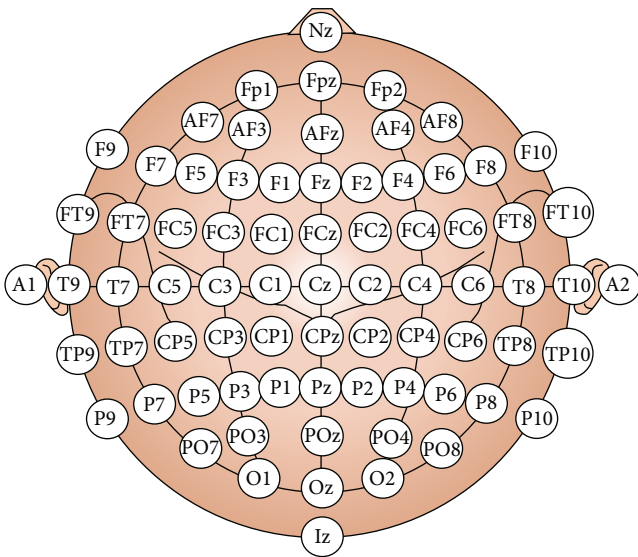


FIGURE 2: The 10–20 system of electrode placement [3].

There exist several research studies, EEG-based emotion recognition systems. Koelstra et al. [5] presented methods for single trial classification using both EEG and peripheral physiological signals. Power spectrum density (PSD) of EEG signals was used as the features. A Support vector machine (SVM) classifier was used to classify two levels of valence states and two levels of arousal states. For EEG analysis results, average and maximum classification rates of 55.7% and 67.0% were obtained for arousal and 58.8% and 76.0% for valence. Soleymani et al. [6] provided a multimodal dataset, called “MAHNOB-HCI,” for an analysis of human affective states. The EEG and peripheral physiological signals were employed to classify emotion states. The system used PSD of EEG signals from 32 channels as input features. A SVM classifier was implemented to classify three levels of valence states and three levels of arousal states. For EEG-based classification, the accuracy rates for valence and arousal are 57.0% and 52.4%, respectively. Huang et al. [7] developed an asymmetry spatial pattern (ASP) technique to extract features for EEG-based emotion recognition algorithm. The system

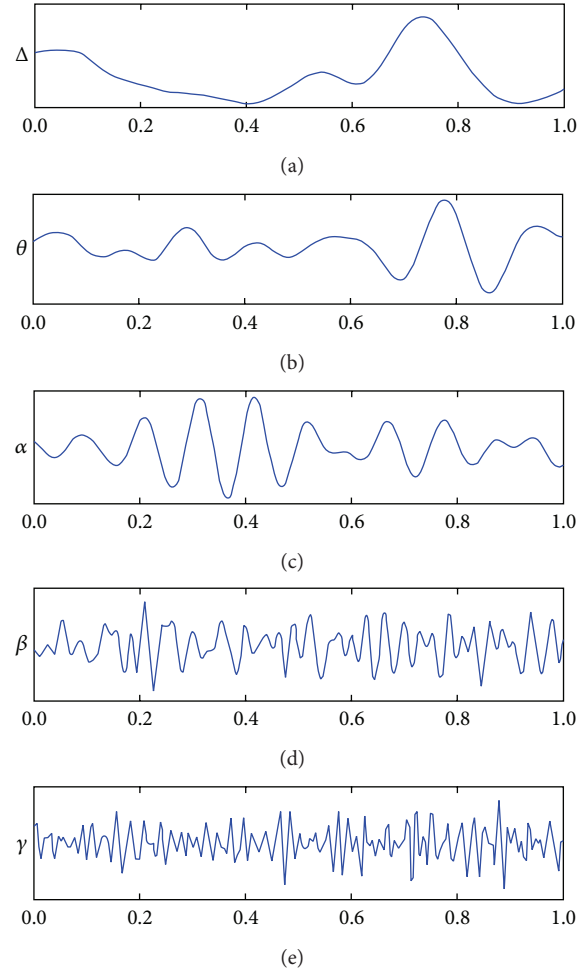


FIGURE 3: Brain waves in 5 main frequency bands [4].

employed K-Nearest Neighbor (K-NN), naive Bayes (NB), and support vector machine (SVM) for emotion classification. The average accuracy rates for valence and arousal are 66.05% and 82.46%, respectively.

Moreover, several studies [8–11] used PSD of EEG data as the input features and performed emotion classification by using SVM. Other machine learning techniques, such as naive Bayes, K-NN, LDA, and ANN, have been applied in other studies [12–15]. Although the number of research studies on EEG-based emotion recognition algorithms has been increasing in recent years, the efficiency of these algorithms is limited.

2. An Overview of Deep Learning Network

2.1. Hierarchy Feature Learning. Deep learning network (DLN) is capable of discovering unknown feature coherences of input signals that is crucial for the learning task to represent such a complicated model. The DLN provides hierarchical feature learning approach. Learned features at high-level are derived from features at low-level with greedy layer-wise unsupervised pre-training. This unsupervised pre-training provides the stage for a final training phase that is fine-tuning

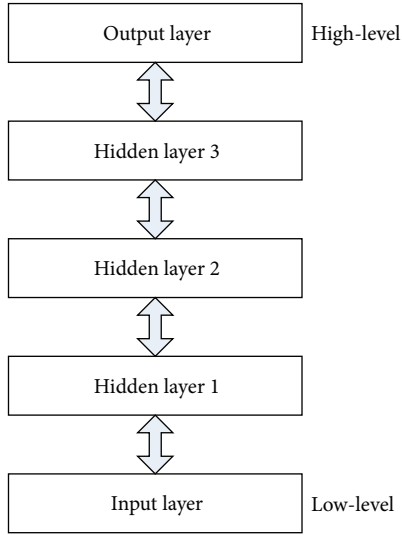


FIGURE 4: Hierarchical architecture of DLN.

process with respect to a supervised training criterion based on gradient descent optimization. Consequently, the primary purpose of DLN is to learn the kind of complicated functions that can represent high-level abstraction. A hierarchical architecture of DLN is illustrated in Figure 4.

The DLN potentially performs self-taught learning from very large numbers of sets of unlabeled data. When learning algorithms process more data, they provide better performance. The key advantage of self-taught learning and unsupervised feature learning is that the algorithm can learn from unlabeled data, and then it can learn from massive amount of information. Consequently, DLN algorithm is suitable for problems where there are a plenty of sets of unlabeled data and a handful amount of sets of labeled data.

2.2. Stacked Autoencoder. A stacked autoencoder is a neural network consisting of multiple layers of sparse autoencoders in which the outputs of each layer are wired to the inputs of the successive layers. The structure of an autoencoder is depicted in Figure 5. The autoencoder tries to learn an approximation to the identity function, shown as follows:

$$\hat{x} = h_{w,b}(x) \approx x. \quad (1)$$

The DLN exploits the unsupervised pretraining technique with greedy layerwise training. The algorithm performs unsupervised pretraining one layer at a time, starting from the input layer to the output layer. The first sparse autoencoder (1st hidden layer) is trained on the raw inputs (x) to learn primary features $h^{(1)}$ on the inputs. During pretraining process, all of weight and bias parameters have been learned to minimize the cost function, shown in (2). Next, the algorithm performs forward propagation by using the raw inputs into this trained sparse autoencoder to obtain the primary feature activations. For pretraining in the next hidden layer,

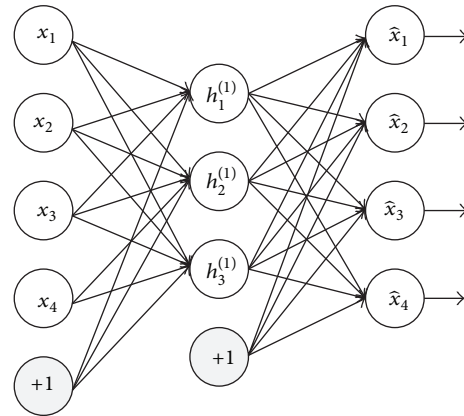


FIGURE 5: Structure of an autoencoder.

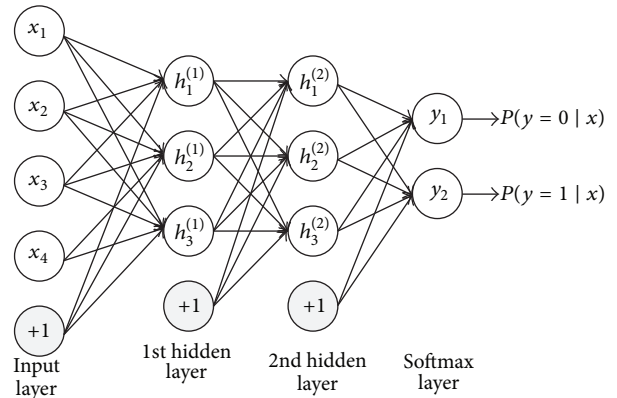


FIGURE 6: Stacked autoencoder with softmax classifier.

the algorithm computes its features in the same procedure from the learned features from the previous hidden layers:

$$\text{Cost} = \frac{1}{2n} \sum_{i=1}^n (\hat{x}_i - x_i)^2 + \beta \sum_{j=1}^m \text{KL}(\rho \parallel \hat{\rho}_j) + \frac{\lambda}{2} \sum_{i=1}^n \sum_{j=1}^m \theta_{ij}^2 \quad (2)$$

where m is number of hidden nodes, n is number of inputs, β is weight of sparsity penalty, KL is Kullback-Leibler divergence function, ρ is sparsity parameter, $\hat{\rho}_j$ is probability of firing activity, λ is weight decay parameter, and θ is weight of hidden nodes.

2.3. Softmax Classifier. Softmax classifier is responsible for statistically estimating the probability of output values of the DLN. Softmax classifier attempts to learn all of weight and bias parameters by using the learned features of the last hidden layer. A stacked autoencoder with 2 hidden layers and softmax classifier for binary classification is illustrated in Figure 6. In the case of binary classification ($k = 2$), the softmax regression hypothesis outputs $h_{\theta}(x)$, shown as follows:

$$h_{\theta}(x) = \frac{1}{e^{\theta_1^T x} + e^{\theta_2^T x}} \begin{bmatrix} e^{\theta_1^T x} \\ e^{\theta_2^T x} \end{bmatrix}. \quad (3)$$

Softmax classifier can be generalized to be multiclass classification. The hypothesis will output a vector of k estimated probabilities, shown as follows:

$$h_{\theta}(x) = \frac{1}{\sum_{j=1}^k e^{\theta_j^T x^{(i)}}} \begin{bmatrix} e^{\theta_1^T x^{(i)}} \\ e^{\theta_2^T x^{(i)}} \\ \vdots \\ e^{\theta_k^T x^{(i)}} \end{bmatrix}. \quad (4)$$

The softmax layer needs to learn the weight and bias parameters with supervised learning approach by minimizing its cost function, shown as follows:

$$\text{Cost} = -\frac{1}{m} \sum_{i=1}^m \sum_{j=1}^k 1\{y_i = j\} \log \frac{e^{\theta_j^T x^{(i)}}}{\sum_{l=1}^k e^{\theta_l^T x^{(i)}}} + \frac{\lambda}{2} \sum_{i=1}^k \sum_{j=1}^n \theta_{ij}^2, \quad (5)$$

where m is number of hidden units, n is number of inputs, k is number of classes, y is ground truth, and θ is weight of hidden nodes.

2.4. Fine-Tuning Stacked Autoencoder. After completing the weight and bias parameter learning in the softmax classifier or output layer, the algorithm has to perform fine-tuning of all weight and bias parameters in the whole network simultaneously. Fine-tuning procedure treats all layers of a stacked autoencoder as a single model and improves all the weights of all layers in the network by using backpropagation technique. The standard backpropagation algorithm is used to learn the network weights and biases based on labeled training examples. The learning goal is to minimize classification errors.

2.5. DLN for EEG Data Processing. The original concept of greedy layerwise unsupervised pretraining on the deep learning networks derived from [17]. The network consisted of multilevel restricted Boltzmann machine. Later, Wulsin et al. [18] applied the unsupervised pretraining concept to a stack of autoencoder for classifying and detecting anomaly measurement in EEG waveforms. The paper demonstrated that DLNs and raw data inputs may be more effective for online automated EEG waveform recognition than other standard techniques. DLN has also been applied to classify sleep stages [19]. The study utilized an unsupervised feature learning architecture on both raw EEG data and power spectral feature extraction to perform sleep stage classification.

3. Methodology

3.1. DEAP Dataset. DEAP [20] is a multimodal dataset for analysis of human affective states. The EEG and peripheral physiological signals of 32 subjects were recorded as each subject watched 40 one-minute highlight music videos. After watching each music video, the subjects performed a self-assessment of their levels of arousal, valence, dominance,

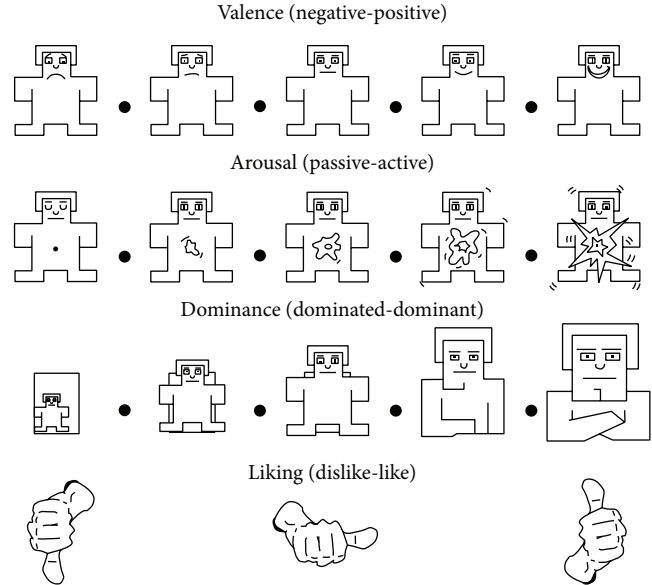


FIGURE 7: Self-assessment manikin for emotion states [21].

and liking. Self-assessment manikins (SAM) [21], as shown in Figure 7, were used to visualize the scales. The subjects selected the numbers 1–9 to indicate their emotion states in each category.

This study mapped the scales (1–9) into 3 levels of each valence and arousal states. The valence scale of 1–3 was mapped to “negative,” 4–6 to “neutral,” and 7–9 to “positive,” respectively. The arousal scale of 1–3 was mapped to “passive,” 4–6 to “neutral,” and 7–9 to “active,” respectively. According to the new scale mapping, the system provides 9-state emotion classification: happy, pleased, relaxed, excited, neutral, calm, distressed, miserable, and depressed, shown in Figure 8.

3.2. EEG Feature Extraction. In our experiment, the proposed system employed 32-channel EEG signals, without any additional peripheral physiological signals. The EEG signals were downsampled from 512 Hz to 128 Hz. The EEG channel consisted of Fp1, AF3, F3, F7, FC5, FC1, C3, T7, CP5, CP1, P3, P7, PO3, O1, Oz, Pz, Fp2, AF4, Fz, F4, F8, FC6, FC2, Cz, C4, T8, CP6, CP2, P4, P8, PO4, and O2. The power spectral density was calculated using FFT with a Hanning window of size 128 samples. The power spectral features of EEG signals on these channels were extracted in 5 frequency bands: theta (4–8 Hz), lower alpha (8–10 Hz), upper alpha (10–12 Hz), beta (12–30 Hz), and gamma (30 Hz up). In addition to the power spectral features, the difference between the spectral power of all the symmetrical 14 pairs of electrodes on the right and the left hemispheres in 5 frequency bands was extracted to measure the possible asymmetry in brain activities due to emotional stimuli. A total number of 230 EEG features were used as the input of DLN.

3.3. Feature Normalization. The baseline power was first subtracted from all of the extracted power spectral features, yielding the change of power relative to the prestimulus

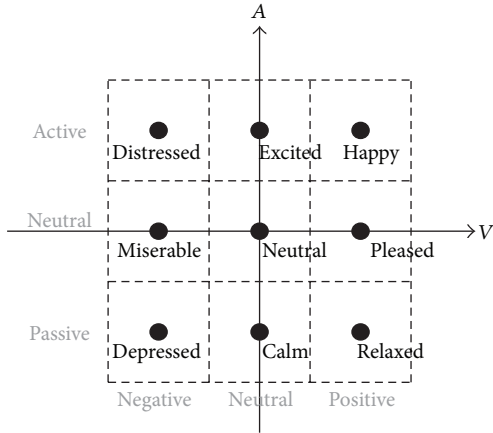


FIGURE 8: Emotion state classes.

period, after which the features were rescaled into the range [0.1, 0.9]. This normalization process is required since the DLN uses sigmoid as the activation function in the output layer. Some of the features below $-2 \cdot SD$ and above $+2 \cdot SD$ were truncated into 0.1 and 0.9, respectively.

3.4. DLN Implementation. The proposed EEG-based emotion recognition system is implemented with a stack of three autoencoders with two softmax layers, illustrated in Figure 9. The system performs emotion classification by estimating valence and arousal states separately. Two softmax classifiers, one for valence and another for arousal, can share the outcome of unsupervised pretraining procedure because they both use the same set of unlabeled raw data. However, two softmax classifiers need to use different stacked autoencoders during fine-tuning backpropagation.

The DLN utilizes the unsupervised pretraining technique with greedy layerwise training, starting from the input layer to the softmax layer. The first sparse autoencoder (1st hidden layer) is trained on the inputs' features (230 power spectral features) to learn the primary features $h^{(1)}$ on these input features. We use L-BFGS to optimize the cost function, squared error between input features and outputs. All of parameter settings in the DLN for EEG-based emotion recognition are shown in Table 1.

Subsequently, the algorithm performs forward propagation by using the input features into this trained sparse autoencoder to obtain the primary feature activations. The features, deriving from feedforward propagation of the 1st hidden layer, must be used to perform unsupervised pretraining in the second hidden layer. The algorithm computes its features in the same procedure from the learned features from the previous hidden layers.

The weight and bias parameters of the softmax layer are trained by using a supervised learning approach. The output features of the last hidden layer are used as the input features of both softmax layers. We use a set of self-assessment emotion states (valence and arousal) of subjects as a ground truth. These softmax layers can be trained as the parameters concurrently.

TABLE 1: DLN parameter settings.

Parameters	Value
Maximum iterations: SAE learning	400
Maximum iterations: softmax learning	100
Maximum iterations: fine-tuning	200
Hidden layer size	100, 50
Sparsity parameter (ρ)	0.10
Weight of sparsity penalty (β)	3.0
Weight decay parameter (λ): SAE learning	$3e^{-3}$
Weight decay parameter (λ): softmax learning	$1e^{-4}$
Weight decay parameter (λ): fine-tuning	$1e^{-3}$

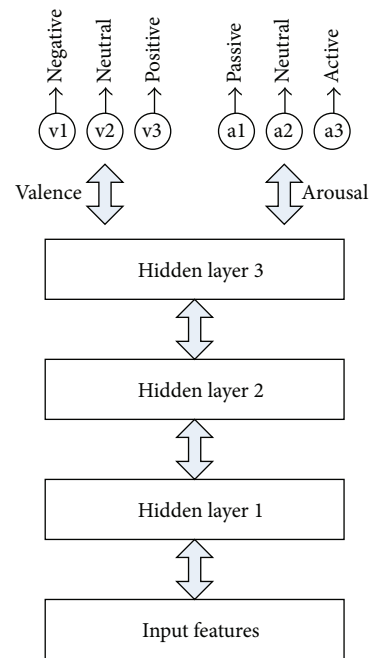


FIGURE 9: DLN with two softmax classifiers.

After the network finishes learning weight and bias parameters in both softmax classifiers, the algorithm has to perform fine-tuning of all weight and bias parameters in the whole network simultaneously. However, we are not able to use the same network parameters for two classifiers. We need to save the learned parameter outcomes of unsupervised pretraining and load the parameters for fine-tuning process of another softmax classifier. The fine-tuning process treats all layers of a stacked autoencoder and softmax layer as a single model and improves all the weights of all layers in the network by using backpropagation technique with supervised approach. The backpropagation process is used to learn the network weights and biases based on labeled training examples to minimize the classification errors.

Summary of DLN training procedure is illustrated in Figure 10. The algorithm performs a greedy layerwise unsupervised pretraining process, starting from the first hidden layer to the last hidden layer. Initial weights and biases of

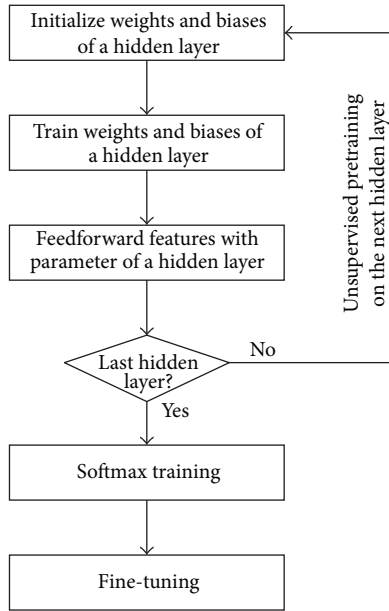


FIGURE 10: Summary of DLN training procedure.

the trained hidden layer are assigned for parameter optimizations. Next, the features from feedforward propagation of the hidden layer must be used to perform unsupervised pretraining in the next hidden layer. After finishing unsupervised pretraining in the last hidden layer, softmax training and fine-tuning procedures are required.

3.5. Covariate Shift Adaptation of Principal Components. Deep learning networks implemented with stacked autoencoders have capability of representing a highly expressive abstraction. Therefore, we are confronted with overfitting problems, especially with the tremendous number of input features and hidden nodes. Moreover, a nonstationary effect of EEG signal is still challenging to develop a reliable EEG-based emotion recognition. The proposed system employs the concept of principal component based covariate shift adaptation [22] to handle both overfitting problems and nonstationary effects simultaneously. Principal component analysis (PCA) [23] is to extract the most important principal components and normalize these components individually by shifting a window over the data to alleviate the effect of nonstationarity.

PCA is a statistical method that uses orthogonal transformation to convert a set of observations of possibly correlated variables into a set of values of linearly uncorrelated variables called principal components. The number of principal components is less than or equal to the number of original variables. This transformation is defined in such a way that the first principal component has the largest possible variance. The proposed system reduces the number of input features from 230 to 50 features.

To minimize the nonstationary effects of input features, the proposed system normalizes the input features with the average of previous feature values within a rectangular window of length w . We performed this normalization for each

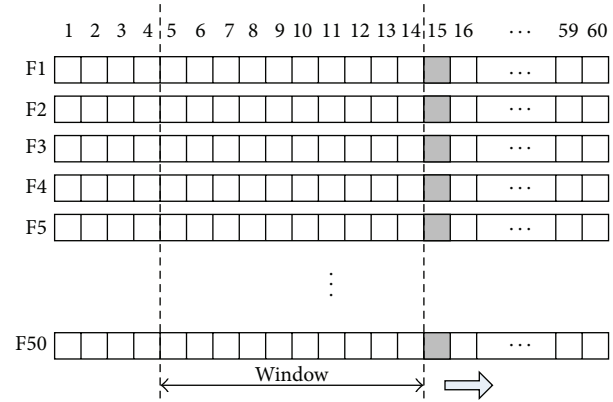


FIGURE 11: Shifting window in covariate shift adaptation.

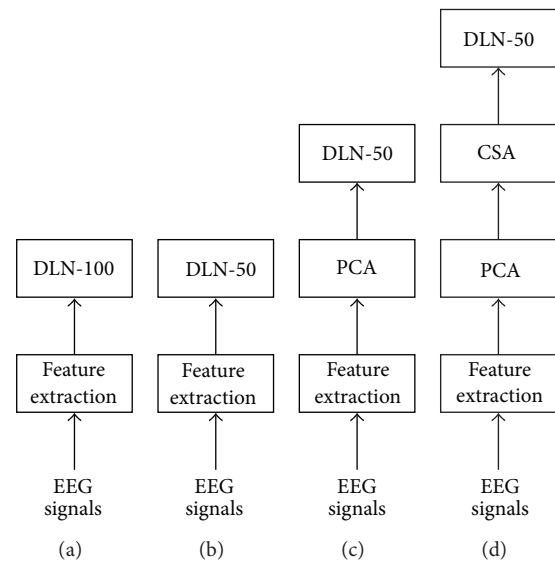


FIGURE 12: Overview of four experiment setups.

input feature individually. Figure 11 illustrates the shifting window during input feature normalization for covariate shift adaptation in each video trial. In our experiments, the window size of the process is set to 10.

4. Experiments and Results

In our experiments, the efficiency of our proposed EEG-based emotion recognition system was evaluated by four experiment setups, shown in Figure 12. In the first setup, we implemented the emotion recognition by using a deep learning network with 100 hidden nodes in each layer (DLN-100). We employed the feature extraction process to calculate all of input features of the DLN from 32-channel EEG signals. At each epoch, the system learned 230 input features consisting of power spectral density of 5 frequency bands and the differences of power spectral densities of 14 asymmetry pairs. Next, the second experiment reduced the number of hidden

nodes to 50 (DLN-50) for investigating the effect of hidden node size in the DLN.

The third experiment setup, shown in Figure 12(c), exploited the PCA to alleviate overfitting problem of the DLN. The PCA extracted the 50 most important components from initial 230 input features. The extracted features were fed into the DLN with 50 hidden nodes in each layer.

The last experimental setup enhanced the efficiency of the emotion recognition system by applying covariate shift adaptation (CSA) concept to solve the problem of nonstationarity in EEG signals. The system normalized the input features with the average of previous feature values within a rectangular window of length w . This normalization was processed for each input feature individually.

The classification accuracy of valence and arousal states in four experiment setups was measured with a leave-one-out cross validation scheme. The full leave-one-out cross validation of 32 subject acquisitions was performed. A training dataset was a composition of all input features from the other 31 subjects. A test dataset was the subject's input features under evaluation. Each individual dataset consisted of power spectral features from EEG signal records while the subject was watching 40 one-minute music videos. The DLN performed its weight and bias optimization based on gradient descent approach. Therefore, the classification accuracy was occasionally affected by its initial weight and bias parameter. In our experiment, we repeated the classification accuracy measurement five times and used the average of the accuracy for further analysis.

The comparison of accuracy from four experiment setups for valence and arousal states on individual subjects is listed in Table 2. The average accuracy and standard deviation of 32 subjects in four experiments are depicted in Figure 13. The DLN-100 provides the accuracy of 49.52% for valence and 46.03% for arousal. The DLN-50 accuracy slightly decreases into 47.87% and 45.50%. The number of hidden nodes in the DLN affects accuracy performance of affective state classification. The greater the number of hidden nodes is, the higher accuracy the DLN provides. In experiments, the number of hidden nodes in each layer was reduced from 100 to 50 nodes. The accuracy decreased 1.62% and 0.53% for valence and arousal classifications, respectively.

There is a strong relationship between autoencoder and principal component analysis [24]. If the number of hidden nodes is less than the number of visible nodes, the autoencoder essentially performs nonlinear principal analysis (NPCA). Both approaches are responsible for learning some correlations of data. If some of the input features are correlated, then these algorithms will be able to discover some of those correlations. The PCA helps the stack of autoencoder to learn some linear correlations among the input features by acting as one more hidden layer at the input and then boost the performance of the learning task. From experimental results, the PCA increases the accuracy performance by 3.01% for valence and 3.14% for arousal.

Subsequently, we applied covariate shift adaptation (CSA) concept to alleviate the effect of nonstationarity in EEG signals. The CSA provides the classification performance to 53.42% for valence and 52.03% for arousal. The PCA+CSA

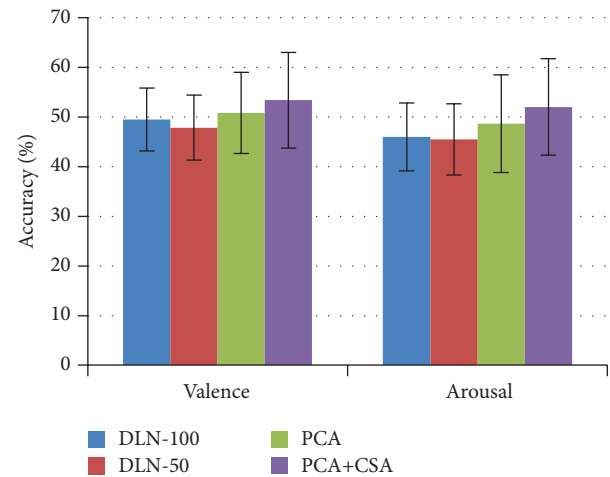


FIGURE 13: Average accuracy of the experiments.

setup improves the accuracy by 5.55% and 6.53% for valence and arousal states, respectively.

To evaluate the efficiency of the DLN, LIBSVM tools [25] were used to measure the accuracy performance of a SVM classifier. Its kernel function was set to radial basis function and other parameters were assigned by default values. There were three experiment setups for the SVM classifier: 230 input features, PCA, and PCA+CSA. Table 2 shows the accuracy performance of the SVM classifier.

The comparison of DLN and SVM accuracy is depicted in Figures 14 and 15 for valence and arousal states, respectively. The DLN outperforms SVM in all experiments. It is interesting to investigate the effect of PCA for feature dimension reduction. The PCA enhanced the accuracy performance of the DLN but it diminished those of the SVM. The effect of PCA on SVM is congruent with a study by Li et al. [26].

Overall accuracy of the SVM classifier to perform EEG-based emotion state classification from DEAP dataset is quite low. In our experiments, all parameters used in the SVM classifier were assigned with their default values. Moreover, the SVM exhaustively estimated its optimal decision surfaces with a large number of sets of training data (74400 instances). These two reasons potentially lead to the SVM's poor performance in this case.

The performance comparison among EEG-based emotion classification algorithms is shown in Table 3. We also utilized a naive Bayes (NB) classifier in WEKA tool to perform emotion state classification of the DEAP dataset with 10-fold cross validation. Another NB classification technique in Chung and Yoon [16] uses a weighted-log-posterior function for the Bayes classifier but its accuracy performance was measured in leave-one-trail-out cross validation.

5. Discussion

The primary purpose of this research is to explore how well the deep learning network in the version of stacked autoencoder performs EEG-based affective computing algorithm. From our experimental results, the average of emotion

TABLE 2: Valence and arousal state classification accuracy with leave-one-subject-out cross validation.

	Valence accuracy (%)							Arousal accuracy (%)						
	DLN			SVM				DLN			SVM			
	N100	N50	PCA	CSA	F230	PCA	CSA	N100	N50	PCA	CSA	F230	PCA	CSA
S01	46.14	44.64	50.31	56.52	38.63	40.29	42.92	50.21	48.98	38.57	42.85	41.67	42.58	23.83
S02	47.64	44.72	49.73	48.48	41.50	44.88	47.04	35.85	37.56	34.65	36.43	32.62	23.25	17.46
S03	52.45	51.43	58.10	59.81	47.38	51.75	40.17	42.84	40.61	42.86	54.43	31.63	22.08	12.38
S04	39.20	36.43	37.52	40.98	24.21	22.12	29.92	39.45	36.98	52.20	46.22	16.50	22.58	34.04
S05	54.32	56.76	55.56	60.97	44.58	33.33	49.42	48.62	47.31	58.78	53.10	41.75	39.13	47.00
S06	49.48	47.43	54.81	71.06	44.50	50.21	60.08	49.24	49.77	45.65	62.18	43.46	29.71	20.29
S07	51.87	52.51	57.94	73.48	47.00	50.58	42.88	46.25	44.27	53.15	56.01	41.13	37.79	39.83
S08	49.19	48.81	54.27	48.44	39.58	47.08	37.54	54.44	52.19	57.24	60.14	46.92	45.25	52.71
S09	55.86	58.81	63.73	38.48	43.00	36.96	27.50	49.81	49.06	62.15	64.18	47.88	51.25	54.46
S10	43.54	40.43	45.27	40.98	39.47	32.83	30.00	41.21	39.52	52.40	64.16	34.96	34.38	25.88
S11	43.87	40.31	44.90	48.11	34.04	37.46	37.38	35.68	34.48	35.45	35.85	23.58	27.54	25.08
S12	44.32	41.56	43.40	48.06	37.79	39.21	42.12	50.74	49.56	44.45	50.81	51.25	46.96	36.88
S13	54.86	53.31	44.10	47.36	49.38	32.92	30.13	48.65	48.31	38.07	41.26	35.08	27.54	28.17
S14	33.81	35.64	43.69	44.06	30.00	35.58	44.67	51.96	49.27	61.99	62.14	44.67	51.63	42.13
S15	58.74	57.45	42.90	46.60	52.13	40.63	40.00	48.55	47.90	64.15	65.01	36.29	29.46	23.25
S16	47.95	45.76	35.69	38.77	36.92	29.83	25.00	41.29	40.61	50.98	49.64	39.33	39.67	21.88
S17	53.20	49.35	45.56	47.86	51.50	44.56	40.00	56.58	58.98	61.61	62.89	50.79	38.83	33.54
S18	55.21	53.72	56.65	57.98	40.92	43.63	42.50	51.43	54.73	62.82	66.47	51.54	39.58	54.33
S19	56.38	53.51	55.90	62.27	39.04	45.38	40.42	47.19	47.52	49.74	59.81	46.67	38.00	42.67
S20	48.65	46.31	62.85	65.11	51.29	42.04	40.00	52.63	56.73	54.95	55.26	50.38	34.79	37.17
S21	51.78	48.14	67.98	70.23	46.92	46.71	42.50	45.97	44.27	37.15	41.85	40.75	35.83	25.58
S22	42.97	43.22	40.44	45.56	37.46	31.71	37.71	47.11	45.65	49.40	52.60	36.13	43.79	30.79
S23	58.43	55.01	58.73	61.73	48.75	48.58	47.50	28.45	31.02	31.15	36.35	24.88	23.25	22.50
S24	49.74	46.81	45.27	45.73	36.54	40.63	35.00	59.45	61.15	58.32	62.72	60.04	46.46	39.67
S25	35.72	36.26	41.56	45.06	31.33	26.04	37.50	40.74	40.65	37.49	39.68	33.33	24.54	25.13
S26	43.16	40.51	45.85	52.90	36.33	36.58	28.21	41.88	39.27	45.07	48.10	27.70	23.54	29.38
S27	58.65	60.14	49.94	52.61	40.58	56.17	54.88	45.86	46.31	42.03	42.81	44.96	34.29	37.13
S28	48.85	46.76	49.35	53.77	38.13	35.79	46.83	40.22	39.52	40.45	45.32	31.71	32.33	24.79
S29	51.25	48.06	51.23	54.52	41.79	45.04	49.00	35.44	35.15	37.28	38.60	27.33	35.21	19.46
S30	56.40	53.76	52.81	54.36	40.46	29.00	34.63	52.21	49.23	41.49	54.64	33.79	32.08	32.33
S31	51.34	48.10	59.02	61.69	43.04	42.46	44.71	41.76	40.02	55.20	51.97	34.67	29.79	36.13
S32	49.67	46.06	63.19	65.90	41.75	34.63	40.00	51.28	49.36	59.49	61.39	45.25	43.38	42.83
Mean	49.52	47.87	50.88	53.42	41.12	39.83	40.26	46.03	45.50	48.64	52.03	39.02	35.21	32.46
SD	±6.34	±6.57	±8.18	±9.64	±6.39	±7.94	±7.87	±6.84	±7.17	±9.85	±9.74	±9.59	±8.56	±10.90

classification accuracy from the deep learning network with a stack of autoencoders is better than existing algorithms. Consequently, the DLN is a promising alternative as EEG-based emotion classifier. However, one of the most challenging limitations for performing EEG-based emotion recognition algorithm is coping with the problem of intersubject variations in their EEG signals.

There are several promising methods to handle the inter-subject variations. Lotte and Guan [27] proposed an algorithm for learning features from other subjects by performing regularization of common spatial patterns (CSP) and linear discriminant analysis (LDA). The method regularized the estimated covariance matrix toward the average covariance matrix of other subjects. Samek et al. [28] studied

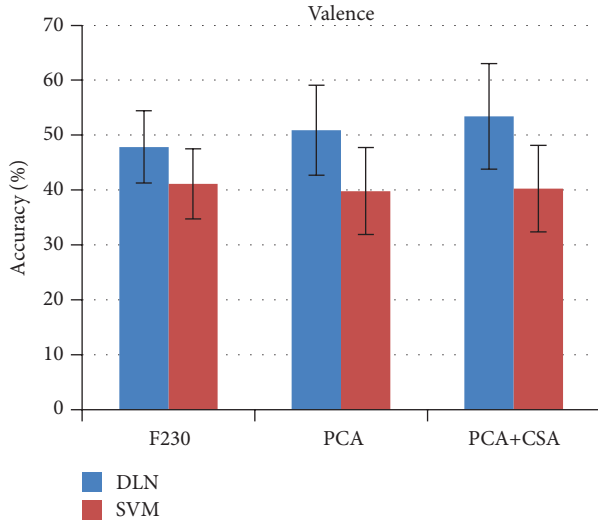


FIGURE 14: DLN versus SVM valence accuracy.

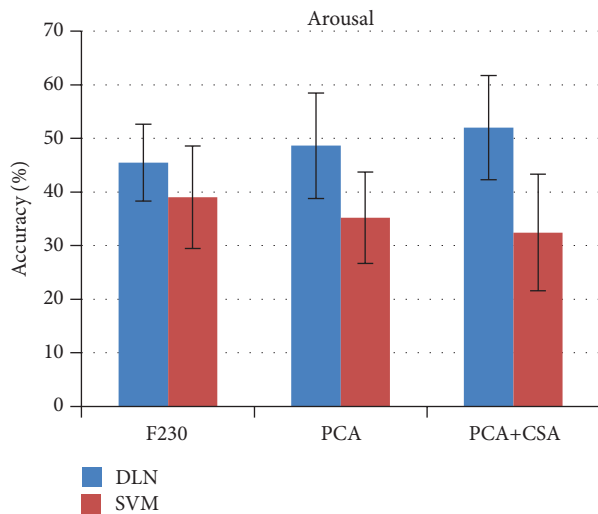


FIGURE 15: DLN versus SVM arousal accuracy.

transferring information about nonstationarities in data, instead of learning the task-relevant part from others. These principal nonstationarities are similar between subjects and can be transferable. Also they have an adverse effect on classification performance, and thus removing them is favorable. We plan to implement one of these two methods, depending on the nonstationary characteristics of the dataset, for alleviating the intersubject variations in our next version of EEG-based emotion recognition system.

One of the major limitations of the DLN is its tremendous amount of computational time requirement during unsupervised pretraining and supervised fine-tuning procedures. In our experiment setup, the DLN for EEG-based emotion recognition is constituted of three stacks of hidden layers and each hidden layer has 100 hidden nodes. At each epoch,

TABLE 3: Summary of accuracy performance (%).

	Valence	Arousal
DLN (with PCA+CSA)	53.42 ± 9.64	52.03 ± 9.74
SVM	41.12 ± 6.39	39.02 ± 9.59
NB-230 features	43.97	33.13
NB-weighted log posterior	53.40*	51.00*

*Subject-dependent results [16].

the algorithm learned 230 input features. To estimate an individual subject's classification accuracy, there were in total 31 subjects watching 40 videos, each of 60 seconds ($31 * 40 * 60 = 74,400$) epochs. They are used to adjust the weight and bias parameters of the DLN. Table 1 shows other DLN's parameter settings. The approximated time used to train the DLN is 20–25 minutes on a laptop computer (Core i5-3320M 2.6 GHz, RAM 8 GB, SSD 128 GB, Windows 7 64-bit Professional).

To speed up training time of the DLN, we are able to exploit some parallelism between two softmax classifiers. However, we need to duplicate the stack of autoencoder implementation for valence and arousal states. Both stacks of autoencoders can be used for separated fine-tuning process of valence and arousal simultaneously. During unsupervised pretraining, two softmax classifiers can share the outcome of unsupervised pretraining procedure because they both use the same set of unlabeled raw data. After completing all sequences of DLN training procedure, shown in Figure 10, the DLN can be used to classify emotion states in real time. Even though the DLN requires tremendous amount of training time, it is able to perform EEG-based emotion classification in real time. During classification phase, the DLN simply feeds the input features through all layers of the network. To give better response, we are able to decrease the window size of covariate shift adaptation but we may trade off with lower classification accuracy.

6. Conclusion

The proposed EEG-based emotion recognition is implemented with a deep learning network and then enhanced with covariate shift adaptation of the principal components. The deep learning network is constituted of a stack of three autoencoders and two softmax classifiers for valence and arousal state classifications. The purpose of PCA is to reduce dimension of input features. The CSA handles the nonstationary effect of EEG signals. The classification accuracy of the DLN with PCA+CSA is 53.42% and 52.05% to classify three levels of valence states and three levels of arousal states. The DLN provides better accuracy performance compared to SVM and naive Bayes classifier. One of the major limitations for performing EEG-based emotion recognition algorithm is dealing with the problem of intersubject variations in their EEG signals. The common features of transferable nonstationary information can be investigated to alleviate the intersubject variation problems.

Conflict of Interests

The authors declare that there is no conflict of interests regarding the publication of this paper.

References

- [1] F. Akram, M. K. Metwally, H. Han, H. Jeon, and T. Kim, "A novel P300-based BCI system for words typing," in *Proceedings of the International Winter Workshop on Brain-Computer Interface (BCI '13)*, pp. 24–25, February 2013.
- [2] R. S. Naveen and A. Julian, "Brain computing interface for wheel chair control," in *Proceedings of the 4th International Conference on Computing, Communications and Networking Technologies (ICCCNT '13)*, pp. 1–5, Tiruchengode, India, July 2013.
- [3] F. Sharbrough, G. E. Chatrion, R. P. Lesser, H. Luders, M. Nuwer, and T. W. Picton, "American Electroencephalographic Society guidelines for standard electrode position nomenclature," *Journal of Clinical Neurophysiology*, vol. 8, no. 2, pp. 200–202, 1991.
- [4] Wikipedia, "Electroencephalography," March 2014, <http://en.wikipedia.org/wiki/Electroencephalography>.
- [5] S. Koelstra, A. Yazdani, M. Soleymani et al., "Single trial classification of EEG and peripheral physiological signals for recognition of emotions induced by music videos," in *Proceedings of the International Conference on Brain Informatics*, Toronto, Canada, 2010.
- [6] M. Soleymani, J. Lichtenauer, T. Pun, and M. Pantic, "A multimodal database for affect recognition and implicit tagging," *IEEE Transactions on Affective Computing*, vol. 3, no. 1, pp. 42–55, 2012.
- [7] D. Huang, C. Guan, K. K. Ang, H. Zhang, and Y. Pan, "Asymmetric spatial pattern for EEG-based emotion detection," in *Proceeding of the International Joint Conference on Neural Networks (IJCNN '12)*, pp. 1–7, Brisbane, Australia, June 2012.
- [8] G. Chanel, J. J. M. Kierkels, M. Soleymani, and T. Pun, "Short-term emotion assessment in a recall paradigm," *International Journal of Human Computer Studies*, vol. 67, no. 8, pp. 607–627, 2009.
- [9] D. Nie, X.-W. Wang, L.-C. Shi, and B.-L. Lu, "EEG-based emotion recognition during watching movies," in *Proceedings of the 5th International IEEE/EMBS Conference on Neural Engineering (NER '11)*, pp. 667–670, Cancun, Mexico, May 2011.
- [10] X.-W. Wang, D. Nie, and B.-L. Lu, "EEG-based emotion recognition using frequency domain features and support vector machines," in *Neural Information Processing*, B.-L. Lu, L. Zhang, and J. Kwok, Eds., vol. 7062, pp. 734–743, Springer, Berlin, Germany, 2011.
- [11] N. Jatupaiboon, S. Pan-ngum, and P. Israsena, "Real-time EEG-based happiness detection system," *The Scientific World Journal*, vol. 2013, Article ID 618649, 12 pages, 2013.
- [12] G. Chanel, J. Kronegg, D. Grandjean, and T. Pun, "Emotion assessment: arousal evaluation using EEG's and peripheral physiological signals," in *Multimedia Content Representation, Classification and Security*, B. Gunsel, A. Jain, A. M. Tekalp, and B. Sankur, Eds., vol. 4105, pp. 530–537, Springer, Berlin, Germany, 2006.
- [13] O. AlZoubi, R. A. Calvo, and R. H. Stevens, "Classification of EEG for affect recognition: an adaptive approach," in *AI 2009: Advances in Artificial Intelligence*, A. Nicholson and X. Li, Eds., vol. 5866 of *Lecture Notes in Computer Science*, pp. 52–61, Springer, Berlin, Germany, 2009.
- [14] G. Chanel, C. Rebetez, M. Bétrancourt, and T. Pun, "Emotion assessment from physiological signals for adaptation of game difficulty," *IEEE Transactions on Systems, Man, and Cybernetics A Systems and Humans*, vol. 41, no. 6, pp. 1052–1063, 2011.
- [15] U. Wijeratne and U. Perera, "Intelligent emotion recognition system using electroencephalography and active shape models," in *Proceedings of the 2nd IEEE-EMBS Conference on Biomedical Engineering and Sciences (IECBES '12)*, pp. 636–641, December 2012.
- [16] S. Y. Chung and H. J. Yoon, "Affective classification using Bayesian classifier and supervised learning," in *Proceedings of the 12th International Conference on Control, Automation and Systems (ICCAS '12)*, pp. 1768–1771, October 2012.
- [17] G. E. Hinton, S. Osindero, and Y. Teh, "A fast learning algorithm for deep belief nets," *Neural Computation*, vol. 18, no. 7, pp. 1527–1554, 2006.
- [18] D. F. Wulsin, J. R. Gupta, R. Mani, J. A. Blanco, and B. Litt, "Modeling electroencephalography waveforms with semi-supervised deep belief nets: fast classification and anomaly measurement," *Journal of Neural Engineering*, vol. 8, no. 3, Article ID 036015, 2011.
- [19] M. Långkvist, L. Karlsson, and A. Loutfi, "Sleep stage classification using unsupervised feature learning," *Advances in Artificial Neural Systems*, vol. 2012, Article ID 107046, 9 pages, 2012.
- [20] S. Koelstra, C. Mühl, M. Soleymani et al., "DEAP: a database for emotion analysis; using physiological signals," *IEEE Transactions on Affective Computing*, vol. 3, no. 1, pp. 18–31, 2012.
- [21] J. D. Morris, "SAM: the self-assessment manikin. An efficient cross-cultural measurement of emotion response," *Journal of Advertising Research*, vol. 35, no. 8, pp. 63–68, 1995.
- [22] M. Spüler, W. Rosenstiel, and M. Bogdan, "Principal component based covariate shift adaption to reduce non-stationarity in a MEG-based brain-computer interface," *EURASIP Journal on Advances in Signal Processing*, vol. 2012, article 129, 2012.
- [23] I. T. Jolliffe, *Principal Component Analysis*, Springer, New York, NY, USA, 1986.
- [24] P. Baldi and K. Hornik, "Neural networks and principal component analysis: learning from examples without local minima," *Neural Networks*, vol. 2, no. 1, pp. 53–56, 1989.
- [25] C. Chang and C. Lin, "LIBSVM: a Library for support vector machines," *ACM Transactions on Intelligent Systems and Technology*, vol. 2, article 27, no. 3, 2011.
- [26] K. Li, X. Li, Y. Zhang et al., "Affective state recognition from EEG with deep belief networks," in *Proceedings of the IEEE International Conference on Bioinformatics and Biomedicine*, 2013.
- [27] F. Lotte and C. Guan, "Learning from other subjects helps reducing brain-computer interface calibration time," in *Proceedings of the 35th IEEE International Conference on Acoustics, Speech, and Signal Processing (ICASSP '10)*, pp. 614–617, Dallas, Tex, USA, March 2010.
- [28] W. Samek, F. C. Meinecke, and K. Muller, "Transferring subspaces between subjects in brain-computer interfacing," *IEEE Transactions on Biomedical Engineering*, vol. 60, no. 8, pp. 2289–2298, 2013.

Research Article

Induced Effects of Transcranial Magnetic Stimulation on the Autonomic Nervous System and the Cardiac Rhythm

Mercedes Cabrerizo,¹ Anastasio Cabrera,¹ Juan O. Perez,¹ Jesus de la Rua,¹ Niovi Rojas,¹ Qi Zhou,¹ Alberto Pinzon-Ardila,^{2,3} Sergio M. Gonzalez-Arias,^{3,4} and Malek Adjouadi¹

¹ Center for Advanced Technology and Education, Department of Electrical and Computer Engineering, College of Engineering and Computing, Florida International University (FIU), USA

² Neuroscience Consultants, USA

³ Baptist Health Neuroscience Center, Baptist Hospital of Miami, USA

⁴ FIU Herbert Wertheim College of Medicine, USA

Correspondence should be addressed to Mercedes Cabrerizo; cabreriz@fiu.edu

Received 2 May 2014; Accepted 7 June 2014; Published 17 July 2014

Academic Editor: Huiyu Zhou

Copyright © 2014 Mercedes Cabrerizo et al. This is an open access article distributed under the Creative Commons Attribution License, which permits unrestricted use, distribution, and reproduction in any medium, provided the original work is properly cited.

Several standard protocols based on repetitive transcranial magnetic stimulation (rTMS) have been employed for treatment of a variety of neurological disorders. Despite their advantages in patients that are retractable to medication, there is a lack of knowledge about the effects of rTMS on the autonomic nervous system that controls the cardiovascular system. Current understanding suggests that the shape of the so-called QRS complex together with the size of the different segments and intervals between the PQRST deflections of the heart could predict the nature of the different arrhythmias and ailments affecting the heart. This preliminary study involving 10 normal subjects from 20 to 30 years of age demonstrated that rTMS can induce changes in the heart rhythm. The autonomic activity that controls the cardiac rhythm was indeed altered by an rTMS session targeting the motor cortex using intensity below the subject's motor threshold and lasting no more than 5 minutes. The rTMS activation resulted in a reduction of the RR intervals (cardioacceleration) in most cases. Most of these cases also showed significant changes in the Poincare plot descriptor SD2 (long-term variability), the area under the low frequency (LF) power spectrum density curve, and the low frequency to high frequency (LF/HF) ratio. The RR intervals changed significantly in specific instants of time during rTMS activation showing either heart rate acceleration or heart rate deceleration.

1. Introduction

The TMS technology was introduced in the 1980s, and since its introduction, it has been used in clinical care for several neurological disorders [1–4]. The initial intent of this technology was to improve the health of patients with depression as exemplified in studies [5–8]. Its application has now been extended to gauge the merits of magnetic stimulation to other neurological disorders such as epilepsy [9–11], Huntington's disease [12], Parkinson's disease [13], different effects of schizophrenia [14–16], Alzheimer's disease, and effects of aging [17, 18], in patients who have had a stroke [19–21], autism [22], and attention deficit and hyperactivity disorders [23, 24]. These are by no means an

exhaustive listing of such noteworthy references, but these are examples of studies that highlight the extensive use of TMS technology. It should be noted that the use of TMS can be performed under two modes of operation, namely, single pulse [25] or repetitive mode of stimulation [26, 27]. Safety measures and ethical considerations in the use of TMS technology are well described in [28, 29]. In many of these disorders, the autonomic symptoms are peculiar and may represent the clinical onset of the disorder. For instance, motor activity and some brain abnormalities are associated with changes in the heart rate rhythm and blood pressure; among those abnormal conditions are epilepsy, stroke, and intense emotional stress. External stimulations with TMS are accompanied with diverse effects depending on the site

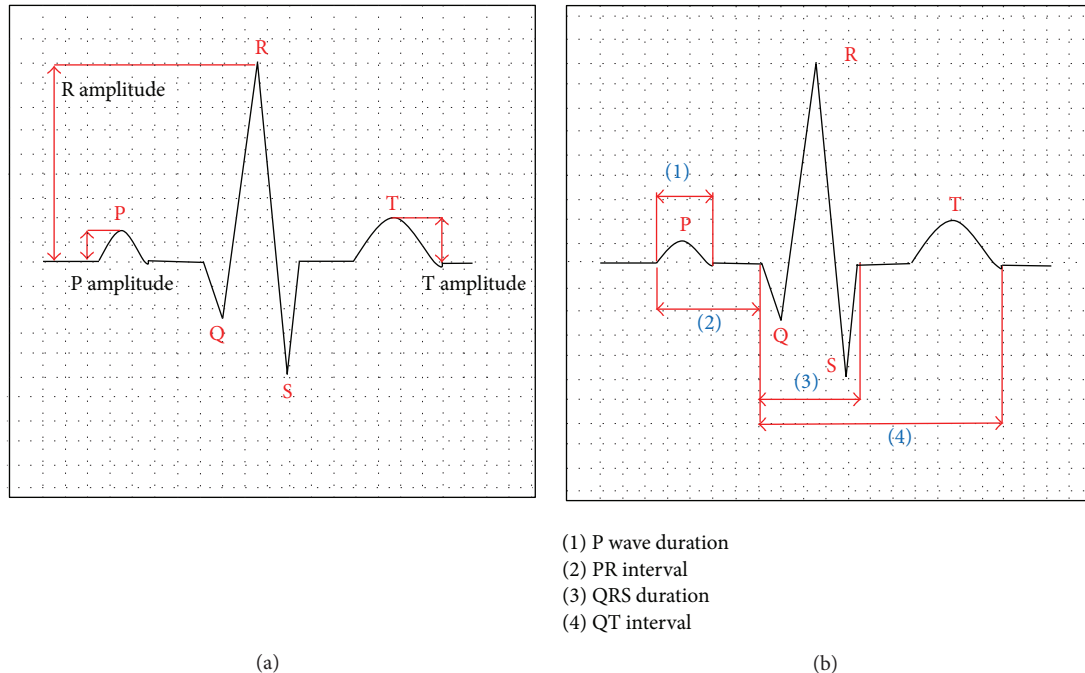


FIGURE 1: PQRST waveforms from an electrocardiography device.

of stimulation [28, 29]. When applied to the motor cortex, which is accompanied by the contraction of muscles, TMS can alter the heart rate variability (HRV) due to connections between the brain cortex and the autonomic centers [30, 31]. Generally, central nervous system (CNS) activation of motor areas is accompanied by diverse scales of cardiac acceleration mediated by the autonomic nervous system (ANS). The ANS is in turn modified by the reflex activity triggered by feedback of the cardiovascular system and articulation sensors which are stimulated by movement [32]. The brain cortex, the brain stem, and the autonomic nerves can alter the heart function and potentially trigger arrhythmias [33]. Such clinical manifestations in some patients suggest that there is a link between cortical structures and autonomic centers. However, not too many studies refer to this problem; only very few research groups have investigated this phenomenon [29]. For example, it is known that epilepsy alters significantly the heart rhythm [10] and produces prolonged QT intervals, T wave alternans, and ventricular late potentials. During seizures, bradycardia and asystole states can occur in some patients. Stroke can also alter the heart rhythm [34] and intense emotions can disrupt significantly the heart rate and blood pressure of a given patient [35]. An illustration of the PQRST deflections of the heart is given in Figure 1.

High frequency stimulation with rTMS (≥ 5 Hz) produces cortical excitation, so when applied to the primary motor cortex, it additionally provokes muscle movement. It could also evoke cardiac responses mediated by connections in the brain cortex with the cardiac-related centers of the CNS. In several studies, muscle reaction due to rTMS over the left primary motor cortex (M1) appears to be limited to the limb areas; however they are also accompanied by changes in the

heart rate variability (HRV) of the RR intervals and the power spectrum of the ECG signals. By using low frequency rTMS [36], it was found that the low frequency (LF) and high frequency (HF) power were significantly increased. Also by measuring the HRV, it was found that rTMS produced significantly greater reduction in the sympathetic/parasympathetic ratio, suggesting improvement in the sympathovagal balance. The LF and HF areas from power spectral plots show that there is an increment of these values after rTMS stimulation, while the LF/HF ratio decreased [37]. As rTMS technology develops in scope and application domains, its use on patients with known cardiac conditions should be carefully weighed with respect to the heart ailment itself and the effects that were observed in this study with healthy controls. With this posed assertion, this study presents a new methodology that relies on a newly developed hardware-software assimilated system with real time integration of electrocardiography (ECG) recordings while a patient is undergoing brain stimulation through rTMS. Real time effects of rTMS on the HRV are performed both in the time and frequency domains through the automatic examination of the RR intervals variability [17].

The integration of several modalities augments the capabilities of a given system to produce a more accurate diagnosis and therefore a better plan for treatment [16, 38–40]. The proposed study thus aligns in time and space electrocardiography (ECG) with the neuronavigated transcranial magnetic stimulation (TMS) machine using a repetitive pulse (rTMS) [41]. By time and space alignment we mean the opportunity for simultaneous recordings of the ECG under repeated transcranial magnetic stimulation (rTMS) while using the same 3D coordinate system on the same patient.

2. Materials and Methods

2.1. Specific Aim of the Study. The strategy behind this study design is to control the magnetic stimulation of the brain according to the selected moments of the cardiac cycle. Empirical evidence suggests that if the magnetic stimulus is not adequately synchronized with the cardiac cycle, there is potential for slowing the heart rate; however, the same stimulus can produce minimal or no alteration of the heart rate if an adequate synchronization is carefully chosen.

More importantly, experimental evaluations indicate the importance of the interval between two consecutive *R* deflections (the deflection with the highest amplitude in the cardiac cycle), which is referred to in this study as the *RR* interval. Whether the treatment is through providing stimulation or medication, every precaution needs to be taken such that any effects observed on these heart deflections in healthy control subjects could not otherwise yield unwarranted effects on subjects with specific heart ailments. For example, according to the American Heart Association, ADD/ADHD stimulant medications have been found to cause sudden death in children and adults with specific heart conditions. Several research studies have later shown that these medications do increase the heart rate in some predisposed individuals. Even though such side effects are rare and are observed in a small number of children with ADHD, they remain of extreme importance and every precaution should be taken to prevent these types of risks.

2.2. Subjects. The effects of the high frequency repetitive TMS (rTMS) on 10 young volunteers (3 females and 7 males) with no history of medical conditions were examined. The study was approved by the Institutional Review Board (Protocol number: IRB-13-0230; Reference number: 101219) and consent forms were provided to the subjects. These subjects did not experience any signs of any cardiovascular disease and were not taking any medication and were advised not to take any caffeine or perform any physical activity that can alter the ECG signal prior to the rTMS session.

All the subjects were laid down in a comfortable chair in a supine position. The Nexstim system's 6-channel EMG module (SR = 1450 Hz, cut-off frequency of 350 Hz for the low pass filter) automatically calculated the motor evoked potential (MEP) amplitudes and latencies as the motor cortex (cortex area of the thumb) is stimulated [34]. Disposable Ag-AgCL surface electrodes were used to record the MEP responses that were displayed in a computer screen in order to assess the validity of the response based on the strength of MEPs reflecting the ability of that area to develop muscle contraction.

2.3. Design and Implementation of the Study. The research aims of this study were carried out using a hardware-software system developed in our lab that aligns in time and space ECG with the operational functions of the TMS machine. This integrated and noninvasive ECG-TMS system consists of two main components: (1) a novel hardware design solution that automatically activates the solenoids of the TMS pedals for the 3 different operational functions: increasing the intensity,

decreasing the intensity, and triggering the electromagnetic pulse; (2) a software module that serves a dual purpose: (i) reading the ECG signal and synchronizing the trigger of the TMS via the hardware component, a synchronization which can be made in relation to any of the deflections of the recorded ECG in monitoring the heartbeat during brain stimulation [42], and (ii) serving as a graphical user interface for man-machine interaction and for the potential deployment of a feedback mechanism.

The magnetic stimulation was performed using the Nexstim eXimia TMS system. The rTMS session was delivered by an 8-inch coil with an orientation quasi-perpendicular to the area of the central sulcus (about 45° from the brain midline) and applied to the left primary motor cortex (M1), which is related to the hand movement of the right side. The coil was positioned 2 cm lateral to the scalp projection of the sagittal suture and 1 cm to the projection of the coronal suture (posterior portion of the frontal lobe). The motor threshold was calculated for each subject prior to the session. This threshold was defined as the lowest magnetic stimulation possible that was still able to induce MEPs response in the range of 100–500 μ V peak-to-peak amplitude in the right arm in the abductor pollicis brevis (APB) muscle in at least 4 out of several attempts. The MRI-guided marker was positioned on the motor cortex at approximately 25 mm depth as an initial position to begin the stimulation. Then, magnetic pulses with an intensity of 10% below this motor threshold were applied and ECG and blood pressure were recorded before, during, and after the rTMS sessions. Heart rate variability (HRV) was processed in the time domain. A comparison was established between the baseline and rTMS activation recordings.

The ECG biophysical amplifier used was able to record 12 leads of real time ECG at a sampling rate (SR) of 1 KHz. A band-pass filter (0.05–300 Hz) was implemented and applied to the recorded signals with a 16-bit A/D conversion, a sensitivity of 0.4 μ V, and a common-mode rejection ratio (CMRR) of 120 dB.

The rTMS protocol implemented for all subjects is as described in Figure 2, where trains of stimuli of 1-second duration at 10 Hz were applied to four different electrode locations (*F1L*, *F2L*, *F1R*, and *F2R*) on the scalp; as a total, 50 pulses were delivered to each brain location, as the train of pulses was repeated 5 times at intervals of 1 minute (interstimulus time: 59 seconds). The intensity of the magnetic pulses was below the visual motor response in the hand. An initial blood pressure was obtained and an ECG signal was recorded for 5 minutes as baseline measurements. These same measurements were also collected at the end of a 5-minute session of brain stimulation to assess the difference in these measurements between baseline and after brain stimulation.

The TMS session applied to the subject in order to record the ECG signals was delivered by the in-house developed software, which is fully compatible with and coupled effectively to the TMS machine. An extended ECG montage with 12 leads was simultaneously recorded as illustrated in Figure 3 and stored in a computer, making it amenable to real time ECG monitoring. During the offline analysis of the ECG, normal *RR* intervals were automatically identified, removing

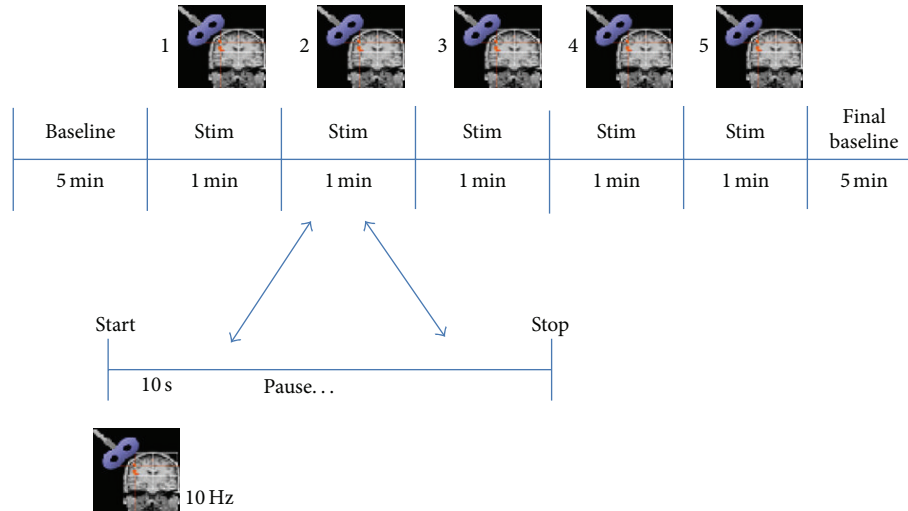


FIGURE 2: rTMS protocol implemented for all subjects. Note that 5 stimuli were applied during intervals of 1 minute of duration.

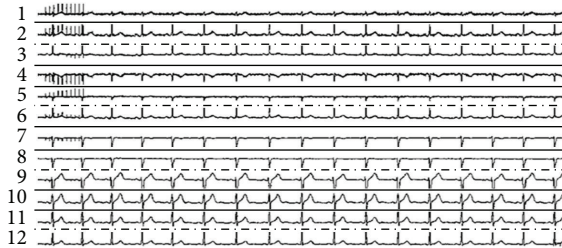


FIGURE 3: 12-lead ECG recording. Note: stimuli artifact (1 sec, 10 Hz) is seen at the beginning of recording in several leads.

those intervals altered by noise or by a surge of ectopic beats, a disturbance of the cardiac rhythm. These intervals were replaced by a mean *RR* interval value calculated automatically by the software.

Figure 4 describes the main steps of the proposed study. A high frequency magnetic pulse was applied to the subject in the motor cortex region in order to see the induced changes of this stimulation in the cardiovascular system and to gauge the balance between the sympathetic and parasympathetic nervous system. The ECG signal was acquired and digitized for 15 minutes. Feature extraction algorithms were performed on the input signal, and a reliable *RR* interval vector was extracted for further processing in both time and frequency domains.

2.4. Time Domain Variability. Time domain variables such as mean, standard deviation of *RR* intervals, and coefficient of variation measured before, during, and after stimulation were extracted [43]. A Poincare plot representation and calculation of its parameters such as SD1 (short-term variability) and SD2 (long-term variability) were also assessed [44].

The heart rate variability (HRV) was significantly changed, as shown in Figure 5 for a particular subject. In this figure, vertical black lines divide the session into five 1-minute intervals. An increase of the heart rate was observed

as the *RR* interval values decreased due to the stimulation on the left frontal motor cortex. Specifically to this subject, during the first minute, there was an evident decrease of the *RR* interval values in the active phase when the subject is stimulated using rTMS as compared to the baseline when the subject is at rest.

As can be observed from the histograms of Figure 5, the mean of the *RR* interval value dropped from 771 in the baseline phase to 615 during the stimulation phase. Furthermore, the standard deviation increased from 33.2 at baseline to 53.5 during stimulation.

To elicit a better understanding of these *RR* intervals, Figure 6 represents a Poincare plot with the distribution of the *RR* interval values at baseline and during stimulation performed on the left side of the motor cortex. The line ($x = y$) in the plot has a physiological significance because all the points that fall in this line correspond to equal and consecutive *RR* interval values (distances from $R_{(1)}-R_{(2)}$, $R_{(2)}-R_{(3)}$, and so on until $R_{(n-1)}-R_{(n)}$). All the points above the identity line correspond to a decrease in the heart rate and the points below this line correspond to an increase in the heart rate [44].

The Poincare plot for a given *RR* vector of length N , denoted by $X = (x_1, x_2, \dots, x_N)$, can be derived using the following two subvectors:

$$X_{RR} = (x_1, x_2, \dots, x_{N-1}), \quad X_{RR+1} = (x_2, x_3, \dots, x_N). \tag{1}$$

These two subvectors correspond to the x -axis and y -axis of the Poincare plot. When this graphical representation is used with real data (10 minutes of ECG recording), the data points are fit to an ellipse for further interpretation. This plot is characterized by two standard descriptors (SD1, SD2) as defined below:

$$SD1 = \sqrt{\text{var}(X_{RR})}, \quad SD2 = \sqrt{\text{var}(X_{RR+1})}. \tag{2}$$

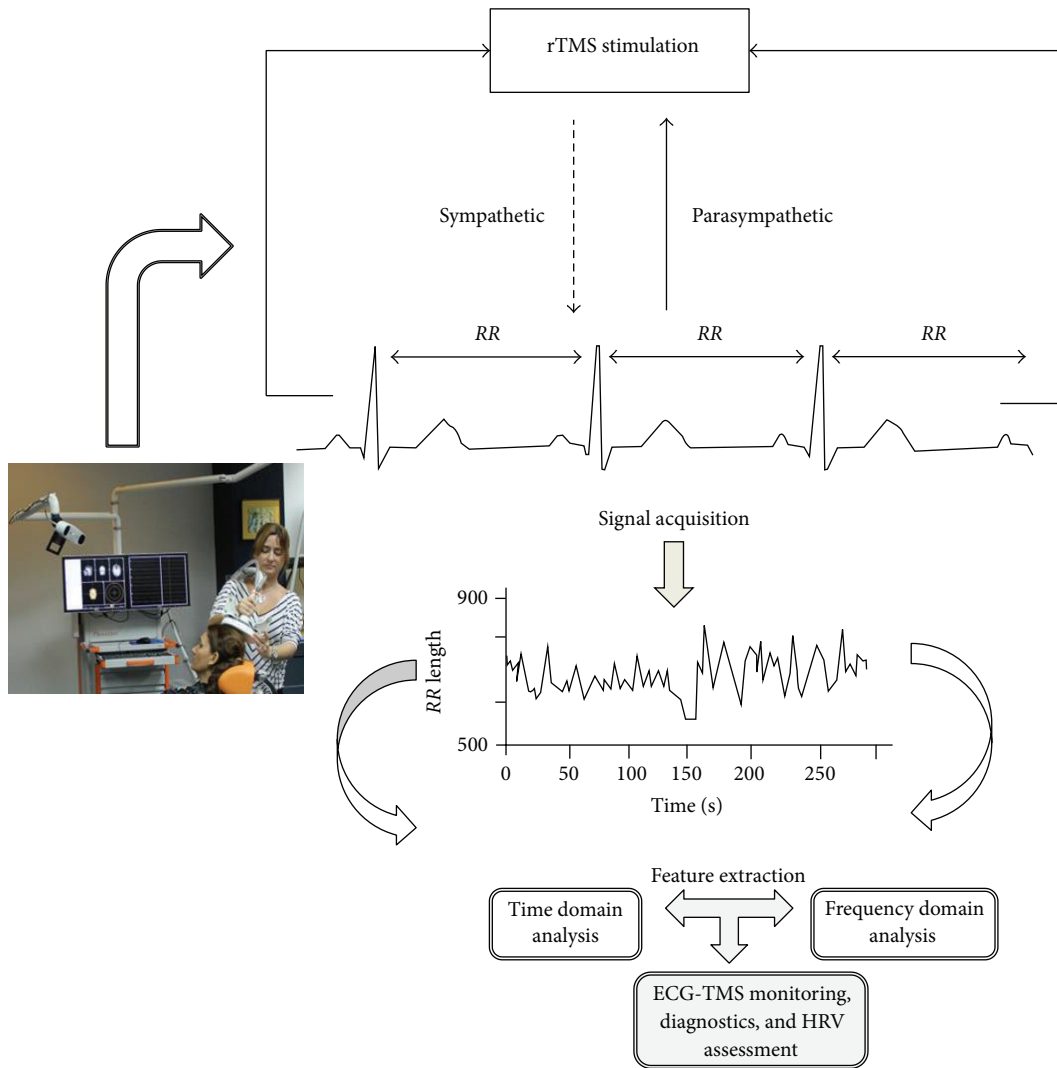


FIGURE 4: Design structure of the ECG-TMS system.

The HRV measure can be expressed as in

$$\text{var} = \left(\frac{X_{RR}}{X_{RR+1}} - \mu \left(\frac{X_{RR}}{X_{RR+1}} \right) \right)^2. \quad (3)$$

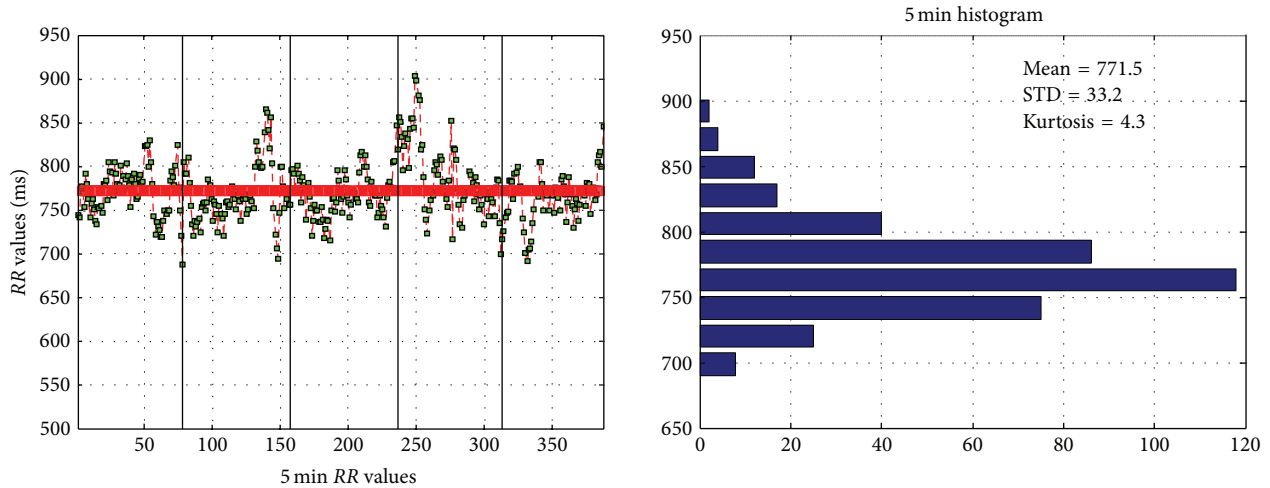
An ellipse has two perpendicular axes that intersect at the center of the ellipse due to its symmetry. The larger of these two axes is called the major axis (SD2), while the smaller of these two axes is called the minor axis (SD1). It is considered that SD1 reflects the standard deviation of the short-term variability of the ECG, while SD2 reflects the standard deviation of the long-term variability of the ECG.

A clear displacement and higher concentration of the points (shorter RR interval) are observed during stimulation as recorded from the F1L electrode, which is located on the left hemisphere. The SD2 descriptor increased and SD1 decreased, which is clear evidence of the change in both the short- and long-term variability.

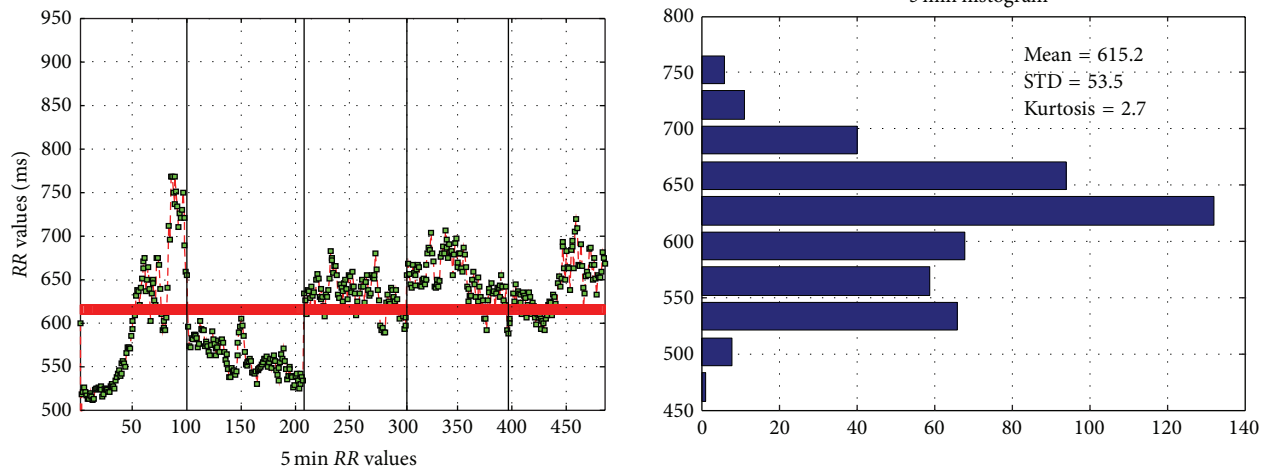
The Poincare plot and its inherent descriptors constitute a novel approach to visualize the HRV in a given patient. The mean and standard deviation of these descriptors were also calculated for all subjects at baseline and during stimulation in order to assess a meaningful global change within the two different phases. Quantified results are provided in Table 1.

An overall assessment of these results as given in Table 1 for all the subjects indicates that the average of the RR intervals during the entire rTMS session decreased (baseline 862 ± 94 , rTMS 840 ± 16 ms). These results also show a slight increase of the heart rate (70 to 71 bpm). However in 7 out of the 10 cases, RR intervals decreased (cardioacceleration; from baseline 850 ± 86 to rTMS 830 ± 119 ms), while, for the remaining 3 cases, RR intervals increased (cardioinhibition; baseline 826 ± 137 , rTMS 865 ± 108 ms).

A new descriptor was incorporated in order to assess with higher accuracy the total variability of a session. The new descriptor takes into account the two standard deviations of the two axes (SD1 and SD2) and the average behavior of the



(a) Baseline showing RR interval values and related histogram



(b) Active phase during rTMS stimulation showing RR intervals and related histogram

FIGURE 5: RR interval and related histograms comparing (a) baseline to (b) active phase.

heart rate ($Mean_{RR}$) as a direct measurement of the HRV. This measurement is normalized with respect to the number of subjects (N) as follows:

$$Total_{var} = \frac{Mean_{RR} * SD1 * SD2}{N} \tag{4}$$

It is observed that the SD1 descriptor did not change after rTMS (baseline 32 ± 9.5 and rTMS 30 ± 11 ms). The descriptor SD2, on the other hand, had a more pronounced variation (baseline 71 ± 17 , rTMS 81 ± 17 ms). SD1 in 70% of the cases showed the same trend (baseline 30 ± 10 , rTMS 30 ± 12 ms). SD2 showed again a larger increase (baseline 64 ± 15 , rTMS 80 ± 17 ms). Conversely in 30% of the cases, both descriptors, SD1 and SD2, decreased after rTMS (SD1 baseline 36 ± 11 , rTMS 31 ± 4.3 ; SD2 baseline 88 ± 11 , rTMS 82 ± 19 ms).

The periodogram slope of every minute interval of the 5-minute period of stimulation was also calculated. If the trend of the periodogram plot increased, the slope of the best fit

line was quantified as “+1”; if instead the trend of the periodogram plot decreased (decrease in RR intervals), the slope was quantified as “-1”; if no change (no significant increase or decrease of RR intervals) occurred, it was quantified as “0.”

Figure 7 shows a comparison between baseline (supine position during 5 minutes) and the activation phase (during rTMS stimulation using a frequency of 10 Hz). The slopes of the baseline phase (blue) and active phase (red) of the RR intervals are calculated for each minute during the recording to show the effect of the rTMS on the heart rate.

The stimulation started at the beginning of every minute and lasted only 1 second. The effects of the magnetic stimulation are observed for 59 seconds, until another stimulation of 1 second begins. From these results, it can be observed that there is an evident deflection of the RR intervals from the baseline, and during stimulation, the heart rate increased due to a decrease of the RR interval values.

An interesting remark to be made on the basis of the results shown in Figure 7 is the gradual move of the red

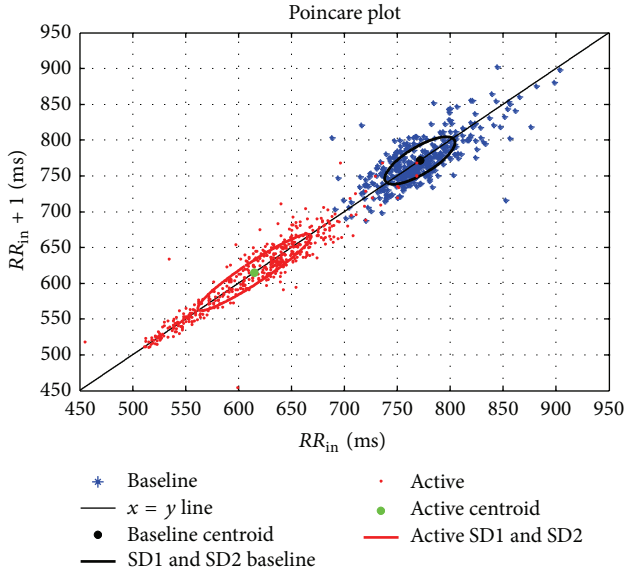


FIGURE 6: Poincare plot of RR intervals distribution.

TABLE 1: Comparative measurements at baseline and during stimulation.

Subject number	Baseline			rTMS stimulation		
	RR	SD1	SD2	RR	SD1	SD2
1	932	21.9	62.1	817	21.6	48.3
2	842	46.6	83.9	820	46.7	96.2
3	780	25.6	56.3	767	17	79.8
4	772	16.2	44	615	12.5	74.7
5	937	35.8	85.7	920	36.7	100
6	893	31	77.1	889	33.8	87.1
7	1004	31.7	53.9	982	38.7	79.2
8	872	30.4	63	888	35.9	84.5
9	918	48.1	87.1	959	26.8	59.8
10	668	28.5	100	746	34.6	98
Mean	861.8	31.58	71.31	840.3	30.43	80.76
STD	93.67	9.45	17.03	15.79	10.67	16.64
Total variability	195,846			204,120		

segments towards the blue (baseline) segments in time as stimulations are given. Does this mean that in time the effect of the stimulation on the ECG is lessened? In other words it is as if one is startled by such stimulation at first and then gets used to it in time; it is an observation to be considered in future studies.

The results showed that changing of trends in slopes during rTMS was statistically significant regardless of whether the orientation is positive or negative. Figure 7 also shows that the number of slope changes, positive or negative, was more frequent at any minute of rTMS than at baseline. These findings suggest that there was disruption of the vagosympathetic balance in most cases as a consequence of

TABLE 2: Influence of rTMS upon the slope of consecutive RR intervals during each minute of baseline and rTMS recordings.

Min.	Baseline					rTMS				
	1	2	3	4	5	1	2	3	4	5
1	0	0	-1	0	0	0	0	-1	0	1
2	1	0	0	0	0	0	-1	1	1	-1
3	0	0	0	-1	1	0	-1	0	0	0
4	1	0	0	0	0	0	1	0	0	0
5	0	0	0	0	0	1	1	0	1	1
6	0	0	1	0	0	0	0	0	0	1
7	0	0	0	0	0	0	0	0	0	0
8	0	0	0	0	0	0	0	-1	1	0
9	0	0	-1	0	0	-1	1	1	1	-1
10	0	0	1	0	1	1	0	0	0	-1
			*							**

Baseline: * $P < 0.05$.

Active phase: ** $P < 0.02$.

rTMS. Some cases showed cardioacceleration followed by cardioinhibition as shown in Table 2.

2.5. *Statistical Analysis.* Comparisons of average values of RR intervals in the whole 5-minute recording were made using the Student's t -test for small samples. When recording signals are analyzed empirically, it is mandatory to assess if results are consistent or are only due to random events. This is performed by statistical hypothesis testing using the P value, which is the probability of obtaining the observed test statistics given the null hypothesis. If the P value is smaller (a given predefined significance level), the null hypothesis is rejected and the observed result is considered "significant" for our analysis. To compare slopes changes, three categories were considered: no change (0), positive (+1), or negative (-1). Statistical significance of $P < 0.05$ using the chi-square method was considered. The chi-square statistic measures, instead of a population average, the difference between the observed counts and the counts that would be expected if there was no relationship between the two groups (baseline and stimulation). An important observation that can be made from the results shown in Table 2 is that, for the baseline, the 3rd minute (indicated by a *) is the one that showed the most significant variation in terms of changes in slope trend ($P < 0.05$). In the active phase, it is minute 5 (indicated by a **) that showed the most significant variation in terms of changes in slope trend ($P < 0.02$).

2.6. *Frequency Domain Variability.* Spectral analysis has been performed using the fast Fourier transform (FFT) in the tachogram signal. For frequency domain measurements, it is recommended that the duration of the ECG recording is at least greater than 5 minutes. ECG signals were visually corrected for ectopic and missed beats. This was performed by filtering the signal to eliminate the false peaks and by interpolating in between missing beats. This way a modified and corrected tachogram is obtained for the analysis. The power spectrum of the HRV vector during 5 minutes of ECG

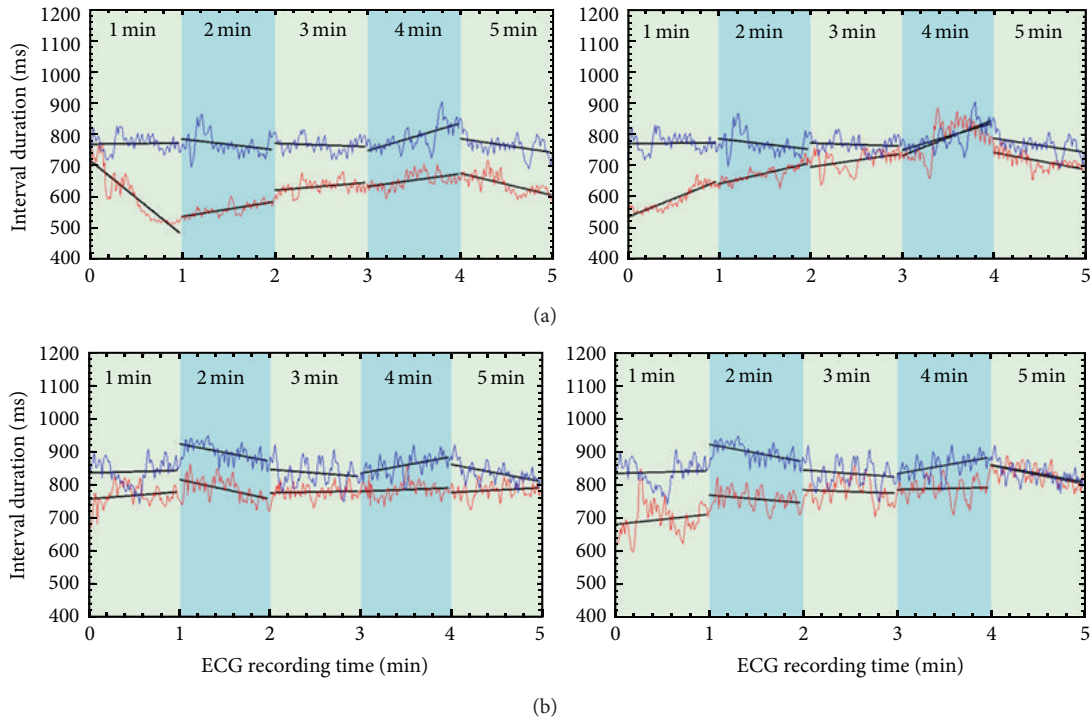


FIGURE 7: Illustrative examples on observed changes on the RR intervals for 2 subjects: subject 1 (a); subject 2 (b).

recording was used as a quantitative measurement to assess autonomic changes in the cardiovascular system.

In humans there are two frequency ranges of interest defined in the low frequency as LF = (0.04–0.15 Hz) and in the high frequency as HF = (0.15–0.4 Hz). Parasympathetic and sympathetic effects are associated with the changes of these frequencies. Parasympathetic activity is considered responsible for these HF values. Both parasympathetic and sympathetic activities, together with other mechanisms, are considered to determine the LF range [45, 46].

As shown in Figure 8, the results of a representative subject show some differences in HRV as determined from spectral analysis in the LF and HF ranges. These results are observed for all subjects of the study. Repetitive TMS, particularly after stimulation of the left hemisphere, induced a slight decrease in the parasympathetic (HF components of the spectrum) and a stronger decrease in the LF power spectrum (partially sympathetic activity). The quantitative changes in the power spectrum of the HRV proved that the cardiovascular control mechanism was altered during rTMS [47, 48].

In reference to the results shown in Figure 9 and Table 3, frequency domain estimates (see Table 3) suggest that the ratio LF/HF, an indicator of sympathetic activation, increased for 60% of the subjects while it decreased for the remaining 40% of the subjects. The majority of these results indicate that rTMS influenced the vasomotor center, which is located in the reticular substance of the medulla and pons, connected with the motor cortex. The indirect influence of rTMS upon cardiac centers was apparently heterogeneous. Some previous reports describe changes in the power spectrum of the

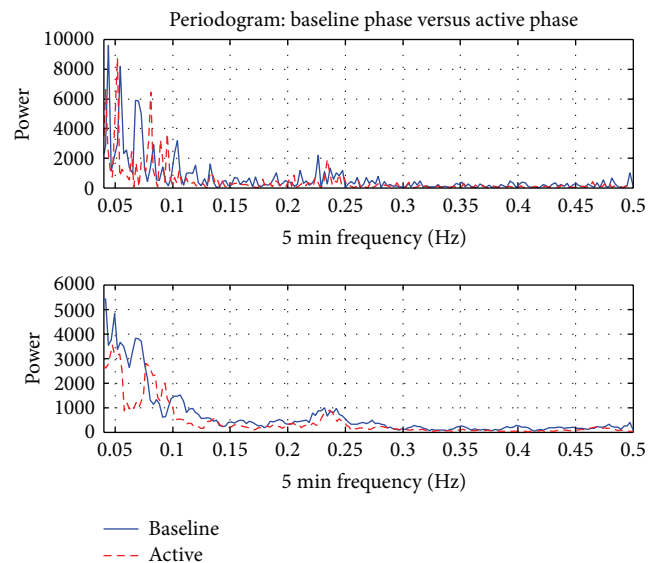


FIGURE 8: Power spectrum. Note: sampling rate of the ECG was 1 Hz, so the frequency spectrum was plotted until 0.5 Hz (Nyquist frequency criteria). There is an increment of the power around 0.05 and 0.1 Hz during the stimulation using 10 Hz and 5 repetitions.

HRV accompanying rTMS. For example, when using low frequency rTMS it was found that both LF and HF power increased significantly. The area under the LF and HF curves from power spectral plots increased after TMS stimulation and LF/HF ratio decrease for 40% of the subjects.

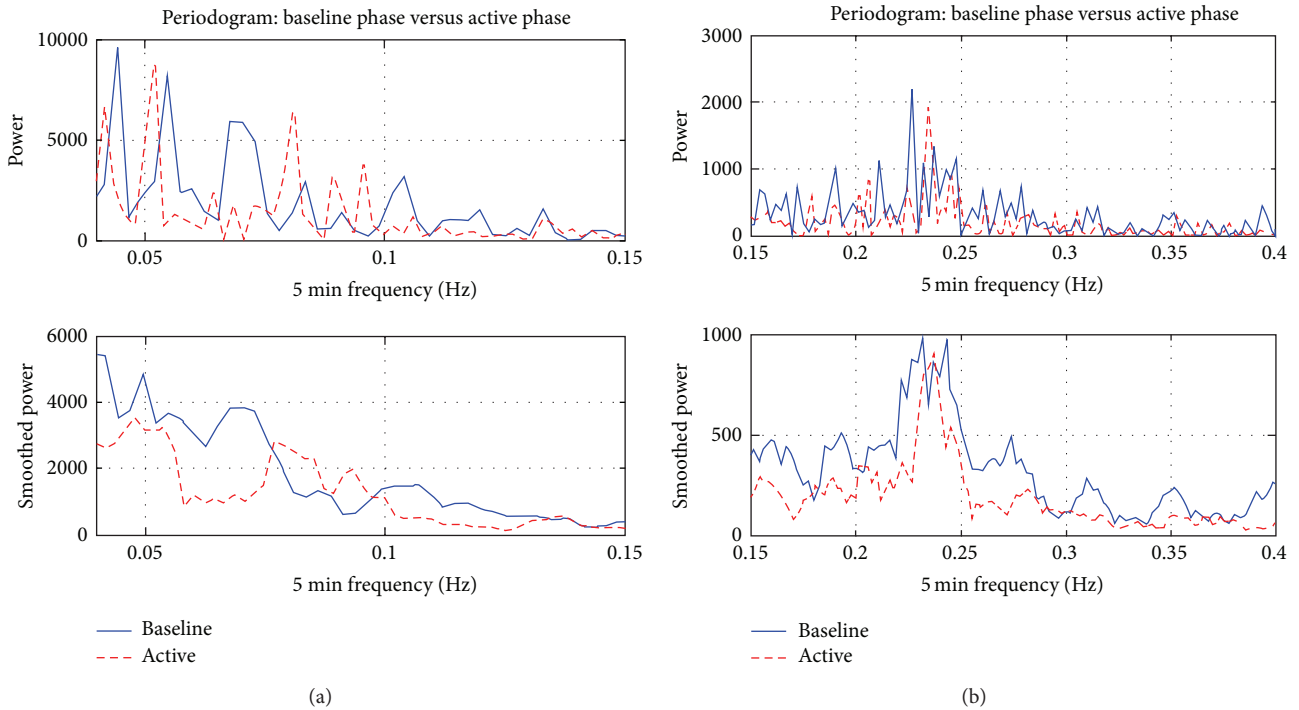


FIGURE 9: Power spectrum: (a) corresponds to LF and (b) to HF components.

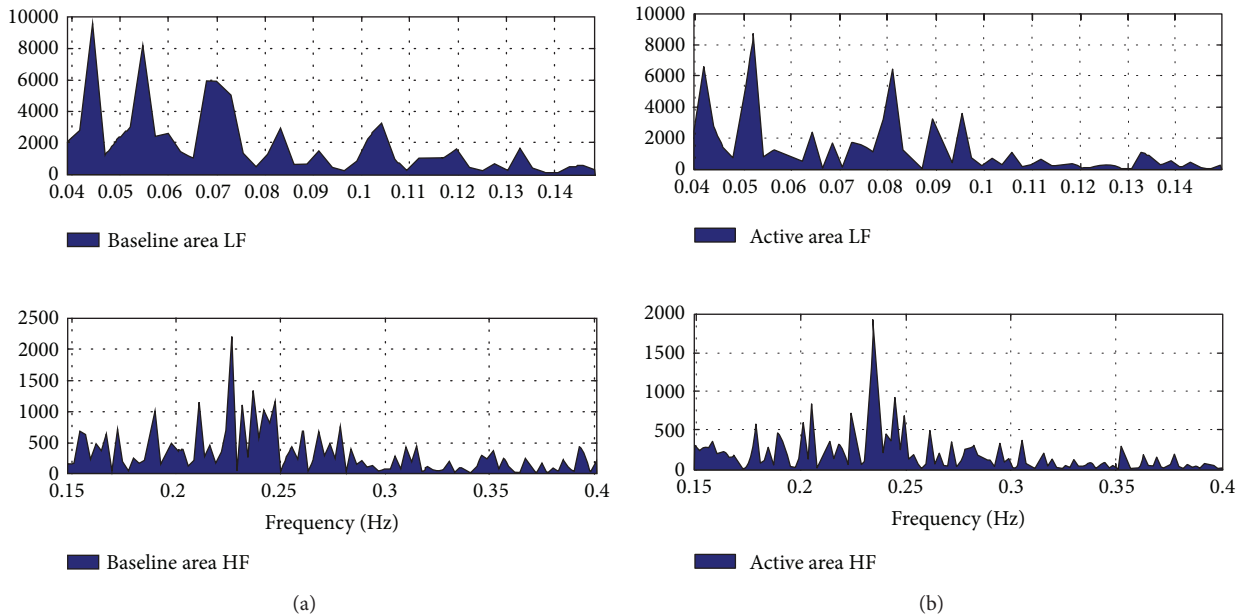


FIGURE 10: Area under the curve: baseline (a) and active phase (b).

A comparison of the area under the curve (AUC) of the LF and HF components, as observed in Figure 9, was performed on the spectral curve of the RR intervals during 5 minutes (at baseline and in the activation phase) for one of the subjects as an illustrative example. Results shown in Figure 10 indicate that there is a considerable change in the total area when comparing baseline to the activation phase: total baseline HF = 81 and total activation HF = 48. The LF is also altered during stimulation.

3. Discussions

No adverse incidents and no relevant changes in blood pressure (± 10 mmHg in systolic or diastolic pressure), or any discomfort, were expressed by the subjects under rTMS stimulation. Motor responses observed in some cases were hand contractions of the contralateral side stimulated. Results show that, after rTMS, the mean RR interval decreased by 2% (cardioacceleration). Two distinct groups were identified

TABLE 3: Differences in HRV (as determined from spectral analysis: LF and HF).

Subject number	Baseline			rTMS stimulation		
	LF	HF	L/H	LF	HF	L/H
1	397	159	2.5	167	197	0.69
2	509	1218	0.41	742	1153	0.64
3	243	167	1.46	298	96	3.12
4	201	81	2.48	143	48	2.98
5	824	405	2.04	683	447	1.53
6	967	394	2.45	1470	1400	1.05
7	659	1589	0.41	450	538	0.84
8	432	271	1.59	856	354	2.42
9	678	245	2.77	302	261	1.16
10	1619	328	3.18	1112	349	4.94
Mean	653	486	1.92	622	484	1.94
STD	418	502	1.4	435	447	1.4

TABLE 4: General statistics.

	RR (ms)	HR (bpm)	SD1	SD2	LF	HF	L/H
	Baseline						
Mean	861	71	32	71	652	489	1.92
±STD	94	4.5	9.5	17	418	502	0.95
	rTMS stimulation						
Mean	840	74	30	81	422	484	1.94
±STD	146	12.5	11	17	435	447	1.4

according to their reaction to rTMS: group 1 with cardioacceleration (7 cases) and group 2 with cardioinhibition (3 cases). In group 1, RR intervals decreased by 6%; one case showed a heart rate increment of 10 bpm. In this group, the SD2 descriptor of the Poincare plot increased by 5.4% while SD1 did not change. The area under the curve of the low frequency band (LF) of the power spectrum density increased by 4%, while the high frequency band increased by 8%. The ratio LF/HF increased from 0.94 to 1.02. In group 2, an increment of 5.2% in RR interval (cardioinhibition) was observed. In this group, both SD2 and SD1 decreased. The LF band area was decreased by 17%, while the HF band increased by 14%. However, the ratio LF/HF decreased from a baseline value of 3.23 to 2.35 after rTMS. Generally, the ratio LF/HF increased in 60% of all cases.

As can be observed in Table 4, the mean RR interval did not change considerably from the baseline phase to the stimulation phase, but the standard deviation increased substantially during rTMS, meaning that dispersion of the points (RR values) became apparent. Also, the mean LF component of the spectral curve decreased during the stimulation, so there was a disruption of the normal rhythm of the parasympathetic and sympathetic activities of the cardiovascular system.

The results showed that, for the majority of the cases, a decrease of the RR interval was observed, while for 25% of the cases the response was reversed. As an overall, changes

in the RR intervals were even more apparent during the first minute of stimulation using trains of 10 Hz.

4. Conclusion

With this study we have extended the application field of TMS and ECG integration by examining the effects of rTMS brain stimulation on the heart rhythm as observed through recorded ECG signals. Our findings indicate that it is important to know and understand the basic interactions between the human cortex and the autonomic nervous system. We suggest that ECG monitoring should be performed when stimulating patients through the TMS machine under the repetitive mode of operation, most especially in subjects with known heart ailments or persons in the older age groups. This is essential for checking in real time for any potential changes that could lead to unforeseen events. Our technology will stop stimulation automatically as soon as such initial changes occur. For example, it is reported that subjects older than 40 years of age are more vulnerable to alterations of the cardiac rhythm. If any rTMS session should be undertaken, a monitoring ECG protocol should be followed in order to avoid any complications.

Finally, the monitoring of the HRV is a powerful tool for understanding and monitoring the cardiovascular system, especially for patients with known cardiac illnesses. Objectively, since rTMS has a great impact on some patients suffering from a diverse number of neurological diseases, it remains to be determined if it can also help in predicting any cardiac condition during or after any session of repetitive magnetic stimulation.

Conflict of Interests

The authors declare that there is no conflict of interests regarding the publication of this paper.

Acknowledgments

This work is supported by the National Science Foundation under Grants CNS-0959985, CNS-1042341, HRD-0833093, IIP 1338922, and IIP-1230661. The support of the Ware Foundation is greatly appreciated.

References

- [1] M. Kobayashi and A. Pascual-Leone, "Transcranial magnetic stimulation in neurology," *The Lancet Neurology*, vol. 2, no. 3, pp. 145–156, 2003.
- [2] M. Hallett, "Transcranial magnetic stimulation and the human brain," *Nature*, vol. 406, no. 6792, pp. 147–150, 2000.
- [3] P. M. Rossini and S. Rossi, "Transcranial magnetic stimulation: diagnostic, therapeutic, and research potential," *Neurology*, vol. 68, no. 7, pp. 484–488, 2007.
- [4] H. R. Siebner, G. Hartwigsen, T. Kassuba, and J. C. Rothwell, "How does transcranial magnetic stimulation modify neuronal activity in the brain? Implications for studies of cognition," *Cortex*, vol. 45, no. 9, pp. 1035–1042, 2009.

- [5] K. Udupa, T. N. Sathyaprabha, J. Thirthalli, K. R. Kishore, T. R. Raju, and B. N. Gangadhar, "Modulation of cardiac autonomic functions in patients with major depression treated with repetitive transcranial magnetic stimulation," *Journal of Affective Disorders*, vol. 104, no. 1-3, pp. 231-236, 2007.
- [6] U. Herwig, Y. Lampe, F. D. Juengling et al., "Add-on rTMS for treatment of depression: a pilot study using stereotaxic coil-navigation according to PET data," *Journal of Psychiatric Research*, vol. 37, no. 4, pp. 267-275, 2003.
- [7] C. Plewnia, P. Pasqualetti, S. Grosse et al., "Treatment of major depression with bilateral theta burst stimulation: a randomized controlled pilot trial," *Journal of Affective Disorders*, vol. 156, pp. 219-223, 2014.
- [8] E. V. Harel, A. Zangen, Y. Roth, I. Reti, Y. Braw, and Y. Levkovitz, "H-coil repetitive transcranial magnetic stimulation for the treatment of bipolar depression: an add-on, safety and feasibility study," *The World Journal of Biological Psychiatry*, vol. 12, no. 2, pp. 119-126, 2011.
- [9] E. H. Bae, L. M. Schrader, K. Machii et al., "Safety and tolerability of repetitive transcranial magnetic stimulation in patients with epilepsy: a review of the literature," *Epilepsy & Behavior*, vol. 10, no. 4, pp. 521-528, 2007.
- [10] A. Ponnusamy, J. L. B. Marques, and M. Reuber, "Comparison of heart rate variability parameters during complex partial seizures and psychogenic nonepileptic seizures," *Epilepsia*, vol. 53, no. 8, pp. 1314-1321, 2012.
- [11] P. R. Bauer, S. Kalitzin, M. Zijlmans, J. W. Sander, and G. H. Visser, "Cortical excitability as a potential clinical marker of epilepsy: a review of the clinical application of transcranial magnetic stimulation," *International Journal of Neural Systems*, vol. 24, no. 2, Article ID 1430001, 21 pages, 2014.
- [12] A. L. Philpott, P. B. Fitzgerald, T. D. R. Cummins, and N. Georgiou-Karistianis, "Transcranial magnetic stimulation as a tool for understanding neurophysiology in Huntington's disease: a review," *Neuroscience and Biobehavioral Reviews*, vol. 37, no. 8, pp. 1420-1433, 2013.
- [13] F. Fregni, C. M. Santos, M. L. Myczkowski et al., "Repetitive transcranial magnetic stimulation is as effective as fluoxetine in the treatment of depression in patients with Parkinson's disease," *Journal of Neurology, Neurosurgery and Psychiatry*, vol. 75, no. 8, pp. 1171-1174, 2004.
- [14] R. Prikryl, L. Ustohal, H. P. Kucerova et al., "Repetitive transcranial magnetic stimulation reduces cigarette consumption in schizophrenia patients," *Progress in Neuro-Psychopharmacology and Biological Psychiatry*, vol. 49, pp. 30-35, 2014.
- [15] Y. Levkovitz, L. Rabany, E. V. Harel, and A. Zangen, "Deep transcranial magnetic stimulation add-on for treatment of negative symptoms and cognitive deficits of schizophrenia: a feasibility study," *International Journal of Neuropsychopharmacology*, vol. 14, no. 7, pp. 991-996, 2011.
- [16] M. Frantseva, J. Cui, F. Farzan, L. V. Chinta, J. L. P. Velazquez, and Z. J. Daskalakis, "Disrupted cortical conductivity in schizophrenia: TMS-EEG study," *Cerebral Cortex*, vol. 24, no. 1, pp. 211-221, 2014.
- [17] P. Julkunen, A. M. Jauhiainen, S. Westerén-Punnonen et al., "Navigated TMS combined with EEG in mild cognitive impairment and Alzheimer's disease: a pilot study," *Journal of Neuroscience Methods*, vol. 172, no. 2, pp. 270-276, 2008.
- [18] P. M. Rossini, S. Rossi, C. Babiloni, and J. Polich, "Clinical neurophysiology of aging brain: from normal aging to neurodegeneration," *Progress in Neurobiology*, vol. 83, no. 6, pp. 375-400, 2007.
- [19] F. C. Hummel and L. G. Cohen, "Non-invasive brain stimulation: a new strategy to improve neurorehabilitation after stroke?" *The Lancet Neurology*, vol. 5, no. 8, pp. 708-712, 2006.
- [20] N. Yozbatiran, M. Alonso-Alonso, J. See et al., "Safety and behavioral effects of high-frequency repetitive transcranial magnetic stimulation in stroke," *Stroke*, vol. 40, no. 1, pp. 309-312, 2009.
- [21] F. Fregni, P. S. Boggio, A. C. Valle et al., "A sham-controlled trial of a 5-day course of repetitive transcranial magnetic stimulation of the unaffected hemisphere in stroke patients," *Stroke*, vol. 37, no. 8, pp. 2115-2122, 2006.
- [22] E. M. Sokhadze, A. El-Baz, J. Baruth, G. Mathai, L. Sears, and M. F. Casanova, "Effects of low frequency repetitive transcranial magnetic stimulation (rTMS) on gamma frequency oscillations and event-related potentials during processing of illusory figures in Autism," *Journal of Autism and Developmental Disorders*, vol. 39, no. 4, pp. 619-634, 2009.
- [23] Y. Bloch, E. V. Harel, S. Aviram, J. Govezensky, G. Ratzoni, and Y. Levkovitz, "Positive effects of repetitive transcranial magnetic stimulation on attention in ADHD Subjects: a randomized controlled pilot study," *The World Journal of Biological Psychiatry*, vol. 11, no. 5, pp. 755-758, 2010.
- [24] M. T. Acosta and F. E. Leon-Sarmiento, "Repetitive transcranial magnetic stimulation (rTMS): new tool, new therapy and new hope for ADHD," *Current Medical Research and Opinion*, vol. 19, no. 2, pp. 125-130, 2003.
- [25] C. S. Konen and P. Haggard, "Multisensory parietal cortex contributes to visual enhancement of touch in humans: a single-pulse TMS study," *Cerebral Cortex*, vol. 24, no. 2, pp. 501-507, 2014.
- [26] T. Paus, M. A. Castro-Alamancos, and M. Petrides, "Cortico-cortical connectivity of the human mid-dorsolateral frontal cortex and its modulation by repetitive transcranial magnetic stimulation," *European Journal of Neuroscience*, vol. 14, no. 8, pp. 1405-1411, 2001.
- [27] A. Berardelli, M. Inghilleri, J. C. Rothwell et al., "Facilitation of muscle evoked responses after repetitive cortical stimulation in man," *Experimental Brain Research*, vol. 122, no. 1, pp. 79-84, 1998.
- [28] E. M. Wassermann, "Risk and safety of repetitive transcranial magnetic stimulation: report and suggested guidelines from the International Workshop on the Safety of Repetitive Transcranial Magnetic Stimulation, June 5-7, 1996," *Electroencephalography and Clinical Neurophysiology/Evoked Potentials*, vol. 108, no. 1, pp. 1-16, 1998.
- [29] S. Rossi, M. Hallett, P. M. Rossini, and A. Pascual-Leone, "Safety, ethical considerations, and application guidelines for the use of transcranial magnetic stimulation in clinical practice and research," *Clinical Neurophysiology*, vol. 120, no. 12, pp. 2008-2039, 2009.
- [30] A. Bastani and S. Jaberzadeh, "Does anodal transcranial direct current stimulation enhance excitability of the motor cortex and motor function in healthy individuals and subjects with stroke: a systematic review and meta-analysis," *Clinical Neurophysiology*, vol. 123, no. 4, pp. 644-657, 2012.
- [31] P. Manganotti, E. Formaggio, S. F. Storti et al., "Effect of high-frequency repetitive transcranial magnetic stimulation on brain excitability in severely brain-injured patients in minimally conscious or vegetative state," *Brain Stimulation*, vol. 6, no. 6, pp. 913-921, 2013.
- [32] W. Barron and J. H. Coote, "The contribution of articular receptors to cardiovascular reflexes elicited by passive limb

- movement," *Journal of Physiology*, vol. 235, no. 2, pp. 423–436, 1973.
- [33] D. P. Zipes, "Heart-brain interactions in cardiac arrhythmias: role of the autonomic nervous system," *Cleveland Clinic Journal of Medicine*, vol. 75, supplement 2, pp. S94–S96, 2008.
- [34] G. Engström, B. Hedblad, S. Juul-Möller, P. Tydén, and L. Janzon, "Cardiac arrhythmias and stroke: increased risk in men with high frequency of atrial ectopic beats," *Stroke*, vol. 31, no. 12, pp. 2925–2929, 2000.
- [35] Y. J. Akashi, H. M. Nef, H. Möllmann, and T. Ueyama, "Stress cardiomyopathy," *Annual Review of Medicine*, vol. 61, pp. 271–286, 2010.
- [36] T. Yoshida, A. Yoshino, Y. Kobayashi, M. Inoue, K. Kamakura, and S. Nomura, "Effects of slow repetitive transcranial magnetic stimulation on heart rate variability according to power spectrum analysis," *Journal of the Neurological Sciences*, vol. 184, no. 1, pp. 77–80, 2001.
- [37] B. M. Clarke, A. R. M. Upton, M. V. Kamath, T. Al-Harbi, and C. M. Castellanos, "Transcranial magnetic stimulation for migraine: clinical effects," *Journal of Headache and Pain*, vol. 7, no. 5, pp. 341–346, 2006.
- [38] J. C. Peters, J. Reithler, T. Schuhmann et al., "On the feasibility of concurrent human TMS-EEG-fMRI measurements," *Journal of Neurophysiology*, vol. 109, no. 4, pp. 1214–1227, 2013.
- [39] M. C. Pellicciari, D. Brignani, and C. Miniussi, "Excitability modulation of the motor system induced by transcranial direct current stimulation: a multimodal approach," *NeuroImage*, vol. 83, pp. 569–580, 2013.
- [40] A. Pascual-Leone, C. Freitas, L. Oberman et al., "Characterizing brain cortical plasticity and network dynamics across the age-span in health and disease with TMS-EEG and TMS-fMRI," *Brain Topography*, vol. 24, no. 3-4, pp. 302–315, 2011.
- [41] M. Adjouadi, M. Cabrerizo, N. Rojas, and J. O. Perez, "Electrocardiography Triggered Transcranial Magnetic Stimulation Systems and Methods," USA Patent, 2013.
- [42] G. Gulli, C. Tarperi, A. Cevese, M. Acler, G. Bongiovanni, and P. Manganotti, "Effects of prefrontal repetitive transcranial magnetic stimulation on the autonomic regulation of cardiovascular function," *Experimental Brain Research*, vol. 226, no. 2, pp. 265–271, 2013.
- [43] Y. Luo, R. H. Hargraves, A. Belle et al., "A hierarchical method for removal of baseline drift from biomedical signals: application in ECG analysis," *The Scientific World Journal*, vol. 2013, Article ID 896056, 10 pages, 2013.
- [44] M. Brennan, M. Palaniswami, and P. Kamen, "Do existing measures of Poincaré plot geometry reflect nonlinear features of heart rate variability?" *IEEE Transactions on Biomedical Engineering*, vol. 48, no. 11, pp. 1342–1347, 2001.
- [45] G. F. Chess, R. M. Tam, and F. R. Calaresu, "Influence of cardiac neural inputs on rhythmic variations of heart period in the cat," *The American Journal of Physiology*, vol. 228, no. 3, pp. 775–780, 1975.
- [46] M. V. Kamath and E. L. Fallen, "Power spectral analysis of heart rate variability—a noninvasive signature of cardiac autonomic function," *Critical Reviews in Biomedical Engineering*, vol. 21, no. 3, pp. 245–311, 1993.
- [47] A. Guyton and J. Hall, "Nervous regulation of the circulation, and rapid control of arterial pressure," in *Textbook of Medical Physiology*, vol. 2006, pp. 184–194, 1991.
- [48] A. J. Camm, M. Malik, J. T. Bigger et al., "Heart rate variability—standards of measurement, physiological interpretation, and clinical use," *Circulation*, vol. 93, pp. 1043–1065, 1996.

Research Article

Adaptive Bacteria Colony Picking in Unstructured Environments Using Intensity Histogram and Unascertained LS-SVM Classifier

Kun Zhang,¹ Minrui Fei,¹ Xin Li,¹ and Huiyu Zhou²

¹ School of Mechatronic Engineering & Automation, Shanghai University, M8 Building, 149 Yanchang Road, ZhaBei District, Shanghai 200072, China

² The Institute of Electronics, Communications and Information Technology, Queen's University Belfast, Belfast, UK

Correspondence should be addressed to Minrui Fei; mrfei@staff.shu.edu.cn

Received 13 March 2014; Accepted 10 April 2014; Published 12 May 2014

Academic Editor: Jinshan Tang

Copyright © 2014 Kun Zhang et al. This is an open access article distributed under the Creative Commons Attribution License, which permits unrestricted use, distribution, and reproduction in any medium, provided the original work is properly cited.

Features analysis is an important task which can significantly affect the performance of automatic bacteria colony picking. Unstructured environments also affect the automatic colony screening. This paper presents a novel approach for adaptive colony segmentation in unstructured environments by treating the detected peaks of intensity histograms as a morphological feature of images. In order to avoid disturbing peaks, an entropy based mean shift filter is introduced to smooth images as a preprocessing step. The relevance and importance of these features can be determined in an improved support vector machine classifier using unascertained least square estimation. Experimental results show that the proposed unascertained least square support vector machine (ULSSVM) has better recognition accuracy than the other state-of-the-art techniques, and its training process takes less time than most of the traditional approaches presented in this paper.

1. Introduction

Bacteria colony isolation [1] is a labor intensive task over the past decades. Manual bacteria colony picking is tedious and experience dependent. Colony screening is in unstructured environments due to different agar mediums and cultivations. Figure 1 is an example of Erythrosin bacteria colony sitting on agar. An automatic colony picking system can be used to make this process consistent and reliable with less time consumption. Researchers worldwide are currently seeking fast and reliable methods for high throughput colony picking. To achieve this, we need to make sure high quality colony illumination and image segmentation are the critical stages of a colony picking system. Currently, there are three major illumination techniques used for image acquisition: (1) drop-in bright-field illumination, (2) back-projective bright-field illumination, and (3) suspended dark-field illumination. Figure 2 shows the different imaging quality based on the three techniques introduced above. Suspended dark-field illumination based approaches can be used to reduce the influence of lights. In this circumstance, colony agar plates are placed in a suspended dark-field environment. Using

reflected and refractive lights, we can obtain volumetric structures of colonies with good image quality. However, the suspended dark-field illumination based approaches could achieve less satisfactory quality of images than the other two approaches, due to a similar color caused by the crowdedness of colonies. Image segmentation approaches such as thresholding [2], region growing [3], watershed [4], and mean shift [5] are commonly used in medical image analysis. Each of these classical methods has its own strengths and weaknesses. For example, a thresholding method is fast but requires the systematic parameters to be changed for different environments. Region growing methods are more robust than the thresholding methods but lack sufficient efficiency. The colony picking systems available on the market have a number of specific requirements in order to achieve good segmentation performance, for example, setting the region of interests, controlling the extent of cluttering, and maintaining appropriate light conditions.

In this paper, we deploy an intensity histogram based morphological features extraction algorithm, which contributes to colony analysis. The proposed method employs a peak-searching method in a standard intensity histogram.



FIGURE 1: Erythrosin bacteria colony on agar.

Afterwards, to achieve correct colony feature classification, we propose an entropy based mean shift algorithm to smooth the image as a preprocess stage. Finally, we introduce an improved approach for feature selection using an unascertained least square support vector machine (ULSSVM) classifier. To our knowledge, this is the first attempt to use the unascertained attributes of the detected features for the purpose of classification. We evaluate the proposed approach on a large dataset of colony images. Based on these experiments, we show that our approach can efficiently deliver correct classification results.

2. Proposed Approach

In the smoothing process of image, it is very important for a nonlinear filter to keep the fringe detail of an image during the process. Optimization techniques have been popularly used in image processing. This is driven by the performance need as the target of an application. However, it is very difficult to obtain an optimal solution (stopping criterion) for individual applications. More details can be found in [6–9]. Mean shift has proven to be appliance effective tool for image processing because of its nonparametric property. Smoothing by mean shift algorithm has been reported in the literature. For example, in [10], Zhao and Xi introduced mean shift as a smooth filter for processing YIQ color images and compared it with Wiener filter. In [11], Han and Sohn used mean shift combined with a sigma filter in an illumination and color compensation system. In literature [12], Sahba and Venetsanopoulos applied mean shift to reserve fringe detail and detect breast mass. These results are promising but the computational speed of mean shift is unexpectedly slow.

Entropy is a measure of complexity. We can also use entropy to inspect system uncertainty. Low entropy images have very little contrast and large runs of pixels with the same value. An image that is perfectly flat will have entropy of zero. Consequently, they can be compressed to a relatively small size. On the other hand, high entropy images have a great deal of contrast from one pixel to the next and consequently have more details than low entropy images. Entropy has been applied in pattern recognition, object tracking, and image segmentation, for example, [13–15], where entropy has been used as a termination criterion. As mentioned in the first section, the proposed feature based colony classification approach begins with entropy based mean shift filter, and

it is followed by applying intensity histogram analysis to the filtered images. The characteristic peaks' coefficients retrieved from intensity histograms are then applied to colony classification within the framework of unascertained least square support vector machine.

2.1. Entropy Based Mean Shift Filter. The following is the idea of a standard mean shift approach [16]. Let x_j be a numerical sample of n in a d -dimensional space. The basic mean shift is defined as

$$M_h(x) = \frac{1}{k} \sum_{x_i \in g_h} (x_i - x), \quad (1)$$

where g_h is a window based on the center x and radius h . k is the sample set number in g_h . $(x_i - x)$ is the relative offset of center x .

Equation (1) is a monotonic form and less effective in a practical application. A Kernel based mean shift algorithm is described as follows:

$$M_h(x) = \frac{\sum_{i=1}^n Q((x_i - x)/h) \alpha(x_i - x)}{\sum_{i=1}^n Q((x_i - x)/h) \alpha(x_i)}, \quad (2)$$

where $\alpha(x)$ is the self-impact factor and $Q(x)$ is a kernel function.

In a color image with $n \times n$ pixels, each pixel corresponds to a 5-dimension vector $R^5 (R, G, B, X, Y)$. Due to the independence of space and color information, the kernel function is obtained in

$$Q_{g_s, g_r}(x) = \frac{1}{g_s^2 g_r^3} q\left(\left\|\frac{x^s}{g_s}\right\|^2\right) q\left(\left\|\frac{x^r}{g_r}\right\|^2\right), \quad (3)$$

where x^s is the spatial position of a pixel; x^r is the color information of a pixel; g_s is a spatial window based on the center x and radius s ; g_r is a color window based on the center x and radius r .

Let $q(x_t)$ be the gray value probability of the outcome x_t , $k = 1, \dots, n$. A is an image with $\log_2(0) = 0$; $\log_2(1/q(x_t))$ is called the surprisal of the outcome x_t . Entropy is defined as

$$F(X) \equiv \sum_{t=1}^n q(x_t) \log_2\left(\frac{1}{q(x_t)}\right) = -\sum_{t=1}^n q(x_t) \log_2 q(x_t). \quad (4)$$

Entropy is determined based on the pixels distribution in an image, which is influenced by two factors: foreground and background or called noise. The uncertainty of entropy is dominated by the noise's variance. Entropy can be used to measure the homogeneity of an image area: the more homogeneous image, the less the entropy values. In practice, when we work with images, due to the noise, entropy cannot decrease to zero but it can reach a stable value. Thus, entropy can be applied as a stopping criterion for a mean shift iteration (Algorithm 1).

2.2. Model of Peak Searching in Intensity Histogram. Intensity histogram is an important feature of images and can be

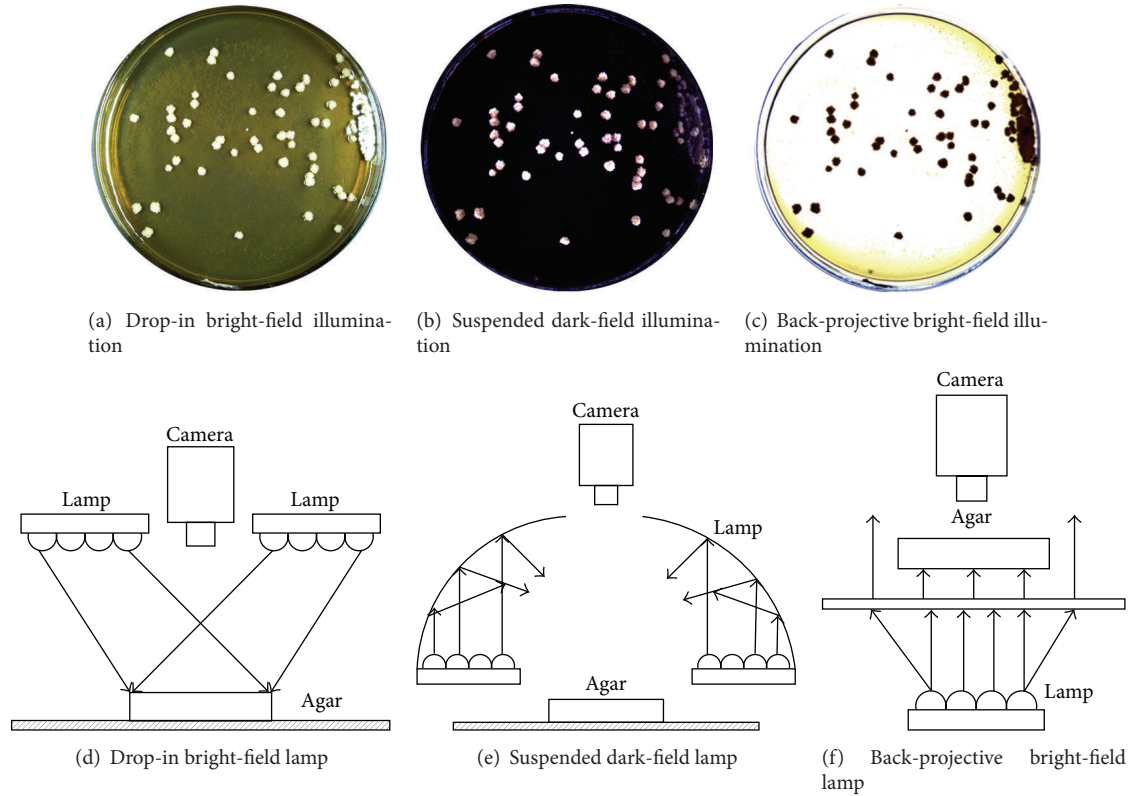


FIGURE 2: Three illumination technologies.

Let $x_i, i = 1, \dots, n$ be the input image. Let $O_i, i = 1, \dots, n$ be the filtered image. Pixel $p \in x_i, p = (R, G, B, x, y) \in R^5$. Let $ent.0$ be the entropy initial value, $ent.1$ be the next iteration of $ent.0$, and $ent.2$ be the next value of $ent.1$. Let $erras$ be the absolute value of the difference between the first two iterations. Let $edset$ be the thresholding as iterations stopping criteria. Our algorithm comprises the steps listed below:

- (1) Initialize $h = 1, y_{h,1} = p_h, ent.2 = 1, erras = 1, edset = 0$.
- (2) While $erras > edset$, then
 - (2.1) Filtering image based on mean shift. Store the image in $O^{[k]}$.
 - (2.2) Calculating entropy from the $O^{[k]}$ and store the image in $ent.1$.
 - (2.3) Entropy is used to calculate the absolute difference which is obtained in the previous step; $erras = |ent.1 - ent.2|$.
 - (2.4) Update the parameters; $ent.2 = ent.1$ and $O^{[k+1]} = O^{[k]}$.
 - (2.5) Calculate the mean shift which is carried out until entropy convergence.
- (3) Store Z_i which is calculated $Z_i = (x_i^s, y_{i,c}^r)$, here x_i^s is the spatial information and $y_{i,c}^r$ is the color range information.

ALGORITHM 1: Entropy based mean shift filtering algorithm.

regarded as the approximate expression of a density function of image intensities. It shows the frequency of an intensity appearing in an image. An intensity histogram is described in

$$G_i = \sum_{m=1}^M \sum_{n=1}^N P(i, m, n), \quad (5)$$

where M and N represent the total numbers of rows and columns, respectively, and G_i represents the appearance times of intensity i , and $P(i, m, n)$ is described as follows:

$$P(i, m, n) = \begin{cases} 1 & P(m, n) = i \\ 0 & P(m, n) \neq i \end{cases} \quad (6)$$

where $P(m, n)$ is the intensity value of point (m, n) . As the sizes of different images may be different, to avoid the impact of image size, we normalize each image according to the following equation:

$$G'_i = \frac{G_i}{T}, \quad (7)$$

where G'_i is a normalization value and T represents the total amount of the pixels of an image. Figure 1 shows an example of bacteria colony and its intensity histogram using (5), (6), and (7).

In Figure 1, the entire image can be divided into two main zones: culture medium zone and colony zone, according

- (1) Obtain $\Delta G'_i$ from the image transformed based on Meanshift algorithm, and using a second order differentiation described in (8).
- (2) Find the highest peak from the entire curve.
- (3) Adaptively select a defined threshold: The threshold used to obtain the global peak is determined by both the Maximum and the minimum peaks (threshold = (max (peak) – min (peak))/8).
If two peaks are detected, continue. If two peaks are found, jump to Step 6.
- Repeat
- (4) Increase the threshold, from ((max (peak) – min (peak))/8) to ((max (peak) – min (peak))/4).
- Until
- (5) Stop if finding two characteristic peaks.
- (6) End

ALGORITHM 2: The proposed adaptive quickly peaks detection.

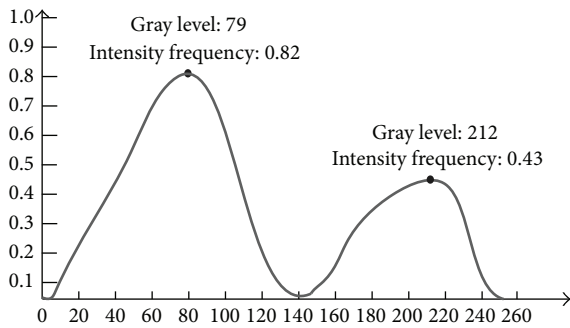


FIGURE 3: Normalised intensity histogram.

to the contrast and density of the image. In Figure 3, there are two peaks, which represent high frequency values of the corresponding intensities. The difference between the gray levels of the two peaks is 133, and the difference between the two intensity frequencies of the two peaks is 0.39. The intensity histogram mathematical model will be introduced in the following sections.

The peaks and valleys shown in Figure 3 can be obtained using the second-order derivative. The method to find a peak or a valley is described in

$$\Delta G'_i = \begin{cases} 1 & G'_i - G'_{i+1} < -H \\ 0 & |G'_i - G'_{i+1}| < H \\ -1 & G'_i - G'_{i+1} > H, \end{cases} \quad (8)$$

where H refers to a positive threshold which is set according to a specific image to reduce inaccuracy because of infinitesimal disturbance. $\Delta G'_i$ represents the tendency of the histogram curve at the point where the intensity equals i . $\Delta G'_i = 1$ means that the curve ascends, $\Delta G'_i = -1$ means that the curve descends, and $\Delta G'_i = 0$ means that the curve is flat. Therefore, $1(0 \cdots 0) - 1$ indicates the peak of the curve, and $-1(0 \cdots 0)1$ refers to the valley of the curve. In Figure 3, the peaks have been extracted according to the method described above.

Through the experiments, it is found that most of the intensity histogram curves change from double-peak to multippeak due to different bacteria colony in different illumination conditions. It is possible to obtain multiple local peaks

or valleys in case the boundary of the intensity histogram is not smooth. The proposed peaks searching algorithm is shown in Algorithm 2.

3. Unascertained Least Square Support Vector Machine

Support vector machines (SVM) have been well studied in the machine learning field, which was proposed by Vapnik [17]. The performance of SVM has been verified in many applications, such as handwriting recognition [18], face recognition [19], and medical pattern matching [20]. But the training speed of SVM is too slow and this hinders its applications. Different from the classical support vector machine methods, the least squares support vector machines (LSSVM) proposed by Suykens and Vandewalle [21] were to change the form of the original convex quadratic optimization problem into a linear optimization problem and they effectively enhance the training speed. But it is hard to classify some uncertain information. Based on LSSVM and unascertained mathematical models, we propose the ULSSVM algorithm. For unascertained information, we can use unascertained number [22] and unascertained programming [23] to describe our algorithm. Please see below for a summary of these theories.

Theorem 1. $[\alpha, \beta], \alpha = x_1 < x_2 < \cdots, x_n = \beta$, if function $f(x)$ satisfies

$$f(x) = \begin{cases} \phi_i & x = x_i, i = 1, \dots, l \\ 0 & x \neq x_i, x \in [\alpha, \beta], \end{cases} \quad (9)$$

$$s.t. \sum_{i=1}^l \phi_i = \phi, \quad 0 < \phi_i \leq 1 (i = 1, \dots, l),$$

where $[\alpha, \beta]$ and $f(x)$ form l order unascertained numbers and are set as $[[\alpha, \beta], f(x)]$. ϕ is the main reliability. $[\alpha, \beta]$ is the value range. $f(x)$ is the main reliability distribution density function. $\{x_i\}$ is a possible value sequence of the unascertained numbers. $\{\phi_i\}$ is a confidence value sequence of the unascertained numbers.

Theorem 2. Setting the unascertained number $a = [[\alpha_1, \alpha_n], f(y)], b = [[\beta_1, \beta_m], k(x)],$

$$f(y) = \begin{cases} \phi_i, & y = y_i, \quad i = 1, \dots, l \\ 0, & y \neq y_i, \quad y \in [y_1, y_l], \end{cases} \quad (10)$$

$$\sum_{i=1}^l \phi_i = \phi, \quad 0 < \phi_i \leq 1 \quad (i = 1, \dots, l), \quad (11)$$

$$k(x) = \begin{cases} \gamma_j, & x = x_j, \quad j = 1, \dots, p \\ 0, & x \neq x_j, \quad x \in [x_1, x_p], \end{cases} \quad (12)$$

$$\sum_{j=1}^p \gamma_j = \gamma, \quad 0 < \gamma_j \leq 1 \quad (j = 1, \dots, p). \quad (13)$$

One calls inequalities $a \leq b, b \leq a$ unascertained events.

Theorem 3. One calls the following programing as an unascertained constraint programing:

$$\begin{aligned} \max \quad & \bar{f} \\ \text{s.t.} \quad & Cr \{f(X, a) \geq \bar{f}\} \geq \gamma \\ & Cr \{g_j(X, b_j) \leq 0, j = 1, \dots, p\} \geq \phi, \end{aligned} \quad (14)$$

where X is a decision vector and a, b_j ($j = 1, \dots, p$) are unascertained parameter vectors. $f(X, a)$ is the target function. $g_j(X, b_j)$ is a constraint function. ϕ, γ ($\phi, \gamma \in (0, 1]$) are confidence levels of the constraint and target function. $Cr\{\cdot\}$ is a credible degree of the unascertained events.

Based on the preliminary knowledge mentioned above, if the SVM training data obtains unascertained information, we can transform the unascertained information into unascertained number

$$a = [[x_1, x_n], f(x)], \quad (15)$$

$$f(x) = \begin{cases} \phi_j & x = x_j, \quad j = 1, \dots, l \\ 0 & x \neq x_j, \quad x \in [x_1, x_l]. \end{cases} \quad (15)$$

The training set is defined in

$$K = \{(y_1, a_1), (y_2, a_2), \dots, (y_l, a_l)\}, \quad (16)$$

where $y_i \in R^l, a_i$ is an unascertained number, (y_i, a_i) ($i = 1, \dots, l$) is an unascertained training point, and K is an unascertained training set.

The objective function can be minimized as follows:

$$\min_{\omega, b, \xi} J(\omega, \xi) = \frac{1}{2} \|\omega\|^2 + \frac{1}{2} \gamma \sum_{i=1}^n \xi_i^2, \quad (17)$$

$$\text{s.t.} \quad A_i [w^T \phi(x_i) + b] = 1 - \xi_i, \quad i = 1, \dots, n.$$

We then define a Lagrange function as

$$\begin{aligned} L(\omega, b, \xi, \alpha) = & \frac{1}{2} \|\omega\|^2 + \frac{1}{2} \gamma \sum_{i=1}^n \xi_i^2 \\ & - \sum_{i=1}^n \alpha_i \{A_i [w^T \phi(x_i) + b] - 1 + \xi_i\}. \end{aligned} \quad (18)$$

According to the KKT condition,

$$\begin{aligned} \frac{\partial L}{\partial \omega} = 0 \implies \omega &= \sum_{i=1}^n \alpha_i A_i \phi(x_i), \\ \frac{\partial L}{\partial b} = 0 \implies \sum_{i=1}^n \alpha_i A_i &= 0, \end{aligned} \quad (19)$$

$$\frac{\partial L}{\partial \xi_i} = 0 \implies \alpha_i = \gamma \xi_i,$$

$$\frac{\partial L}{\partial \alpha_i} = 0 \implies A_i [w^T \phi(x_i) + b] - 1 + \xi_i = 0.$$

Equation (19) can turn into the following matrix problem:

$$\begin{bmatrix} L & 0 & 0 & -Z^T \\ 0 & 0 & 0 & -Y^T \\ 0 & 0 & \gamma^I & -L \\ Z & Y & L & 0 \end{bmatrix} \begin{bmatrix} \bar{\omega} \\ b \\ \xi \\ \alpha \end{bmatrix} = \begin{bmatrix} 0 \\ 0 \\ 0 \\ L \end{bmatrix}, \quad (20)$$

where $Z = [\varphi(x_1)^T y_1, \varphi(x_2)^T y_2, \dots, \varphi(x_n)^T y_n]^T, Y = [y_1, y_2, \dots, y_n], L = [1, 1, \dots, 1]^T, \xi = [\xi_1, \xi_2, \dots, \xi_n],$ and $\alpha = [\alpha_1, \alpha_2, \dots, \alpha_n].$

We eliminate w and ξ and then get the following equations:

$$\begin{bmatrix} 0 & -Y^T \\ Y & \Omega + \frac{1}{\gamma} I \end{bmatrix} \begin{bmatrix} b \\ \alpha \end{bmatrix} = \begin{bmatrix} 0 \\ L \end{bmatrix}, \quad (21)$$

where $\Omega = ZZ^T,$

$$\Omega_{kl} = y_k y_l \phi(x_k)^T \phi(x_l) = y_k y_l \psi(x_k, x_l), \quad (22)$$

where $\Omega(\cdot)$ is a kernel function and satisfies the Mercer theorem.

A set of linear equations will be solved instead of a QP problem. Finally, we can obtain the following optimal classification function:

$$f(x) = \text{sign} \left(\sum_{i=1}^l A_i \alpha_i^* (x \cdot x_i) + b^* \right), \quad (23)$$

where α_i^* is the optimal solutions and corresponding bias $b^*.$ A_i is an unascertained set.

4. Experimental Results

The proposed algorithm is evaluated on colony image databases which are captured using a Basler CCD sensor. The

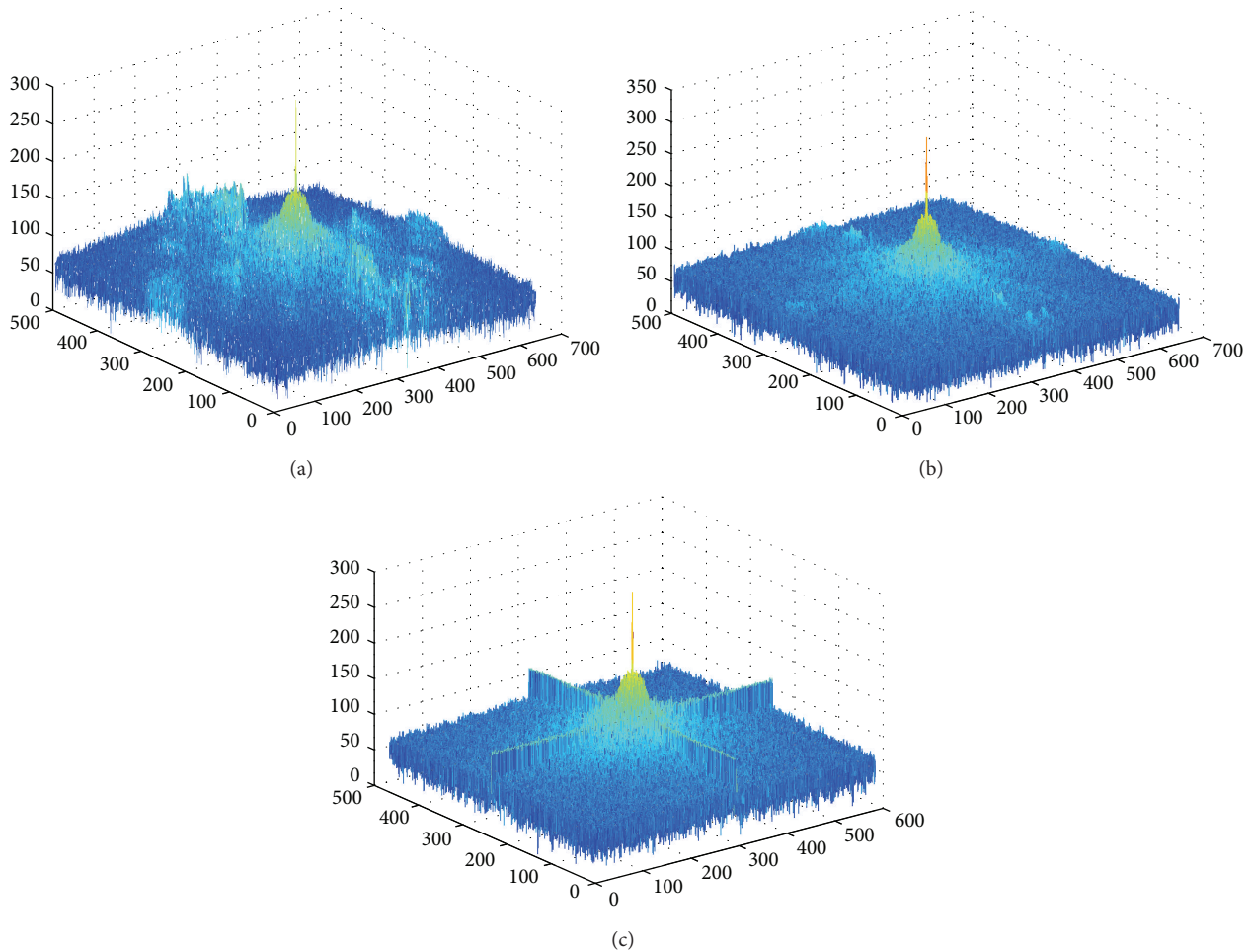


FIGURE 4: Energy spectrum at different stages.

TABLE 1: The filtering performance of three filtering algorithms.

Performance comparison	MSE		
	$\alpha = 0.1$	$\alpha = 0.3$	$\alpha = 0.5$
Median filter	38.541	47.259	85.3254
Fuzzy filter	36.573	49.694	82.3651
Mean shift filter	33.258	40.258	79.6938

images are resized to be 640×480 . The used computer is of a 3.2 G CPU running Windows 7 with a 4 G memory. The first three experiments have been carried out using the colony images to analyze the feasibility and efficiency of the proposed algorithm with MATLAB 7.2. The last experiment is carried out to demonstrate the segmentation effect and performed with Visual Studio 2010.

In image denoising, classical low-passing filters can suppress high frequency noise [24]. However, it is hard for them to preserve the edges of images due to the mixture in some frequency bands. Here, we use energy density spectrums to illustrate the outcomes of different filters [25, 26]. In Figure 4(a), this is the energy spectrum of the original image,

where yellow-orange indicates the major energy of symbol “+” and this area is contaminated by the background noise (i.e., blue and green areas). Figure 4(b) shows the outcome of a low-pass filter, where only the central area of the symbol is kept but the edges of symbol “+” are mixed with the background. In Figure 4(c), based on mean shift, it is clear that the central area of the symbol is outstanding and the edges are also kept. Traditional low-pass filters have good performance on image smoothing but also affect the edge details. In Figure 5 we observe that, after 5 iterations, entropy can reach a stable value, and meanwhile the mean shift iteration automatically stops. Listeria colony entropy is different from the other two. Second row in Figure 6 is Listeria colony. This is because of the cluster colony and agar color is approximated with colony. Figure 6 shows different kinds of colony. The first column shows three different cultures: *Microsporium audouinii*, *Listeria monocytogenes*, and *Cephalosporin*. During the development of cultures, their biochemical reactions appear to be significantly different. As a result, the histograms of cultures in drop-in bright-filed illumination may accompany a number of noisy peaks, illustrated on the second column. Using mean shift based filtering algorithms, we can remove the irregular backgrounds

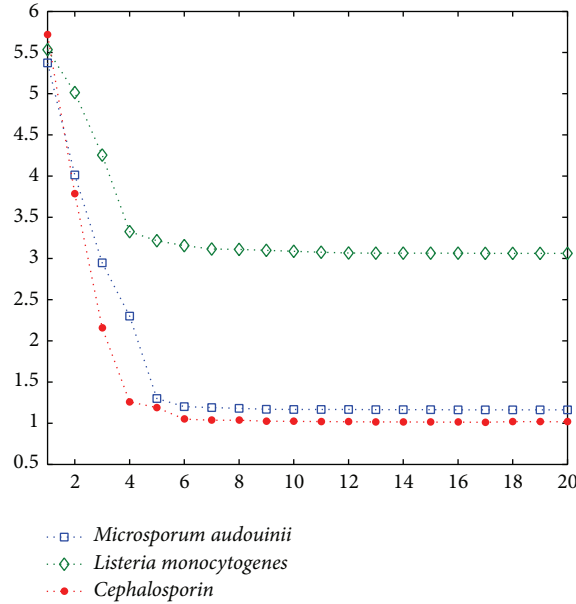


FIGURE 5: Entropy calculation using Mic, Listeria, and Ceph.

TABLE 2: The value corresponding to the unascertained information.

$f_1(y) = \begin{cases} 0.4 & y = 1 \\ 0.3 & y = 2 \\ 0.2 & y = 3 \\ 0.1 & y = 4 \end{cases}$	$f_2(y) = \begin{cases} 0.3 & y = 1 \\ 0.5 & y = 2 \\ 0.2 & y = 3 \\ 0 & y = 4 \end{cases}$	$f_3(y) = \begin{cases} 0 & y = 1 \\ 0.5 & y = 2 \\ 0.1 & y = 3 \\ 0.4 & y = 4 \end{cases}$	$f_4(y) = \begin{cases} 0.7 & y = 1 \\ 0.3 & y = 2 \\ 0 & y = 3 \\ 0 & y = 4 \end{cases}$	$f_5(y) = \begin{cases} 0.4 & y = 1 \\ 0 & y = 2 \\ 0.1 & y = 3 \\ 0.5 & y = 4 \end{cases}$
$f_6(y) = \begin{cases} 0.5 & y = 1 \\ 0.1 & y = 2 \\ 0.4 & y = 3 \\ 0 & y = 4 \end{cases}$	$f_7(y) = \begin{cases} 0.1 & y = 1 \\ 0.4 & y = 2 \\ 0.3 & y = 3 \\ 0.2 & y = 4 \end{cases}$	$f_8(y) = \begin{cases} 0.7 & y = 1 \\ 0.2 & y = 2 \\ 0 & y = 3 \\ 0.1 & y = 4 \end{cases}$	$f_9(y) = \begin{cases} 0.5 & y = 1 \\ 0.1 & y = 2 \\ 0.3 & y = 3 \\ 0 & y = 4 \end{cases}$	$f_{10}(y) = \begin{cases} 0.2 & y = 1 \\ 0.3 & y = 2 \\ 0.1 & y = 3 \\ 0.4 & y = 4 \end{cases}$

and hence reduce noisy peaks. The result of using mean shift is shown on the 3rd column. Furthermore, we apply an adaptive thresholding based peak searching approach in order to detect two peaks, which indicate the features of cultures. This results in the 4th column.

The performance of mean shift filtering can be measured with mean square error (MSE):

$$MSE = \frac{1}{BG} \sum_{x=0}^{B-1} \sum_{y=0}^{G-1} [(I'(x, y) - I(x, y))^2], \quad (24)$$

where $I'(x, y)$ is denoted by the filtered output image and $I(x, y)$ is denoted by the original input image; Table 1 shows the performance of the three kinds of filtering approach.

After extracting the characteristic peaks, we apply the ULSSVM classifier to the data for classification. We now evaluate the performance of our ULSSVM classifier against the classical SVM [27], LSSVM [28], and fuzzy SVM [29] using 400 colony images, where 150 samples belong to class 1, 50 samples belong to class 2, 100 belong to class 3, and the remainder belong to class 4. We randomly select 300

TABLE 3: Classifiers' experimental results.

Classifier	SVM	FSVM	LSSVM	ULSSVM
Accuracy	75.9%	84.6%	73.2%	92.7%
Training speed/s	12.1 s	13.7 s	5.1 s	2.7 s

samples as the training set and the remaining 100 samples are considered as the testing set. There are 130 samples labeled as the unascertained numbers, and half of them are set as training samples. Table 2 shows the values corresponding to the unascertained information. Table 3 shows the classification results. In Table 3, the experimental results demonstrate that the ULSSVM effectively improves the performance of classification.

We carry on screening colony using the ULSSVM classifier. Figure 7 shows the interface of colony screening. Figure 8 is adaptive colony segmentation. The segmentation outcomes of two different colony picking methods are as follows: the first row shows the colony with homogeneous medium and its segmentation results using region growing, and the next two rows show the colony with inhomogeneous medium and

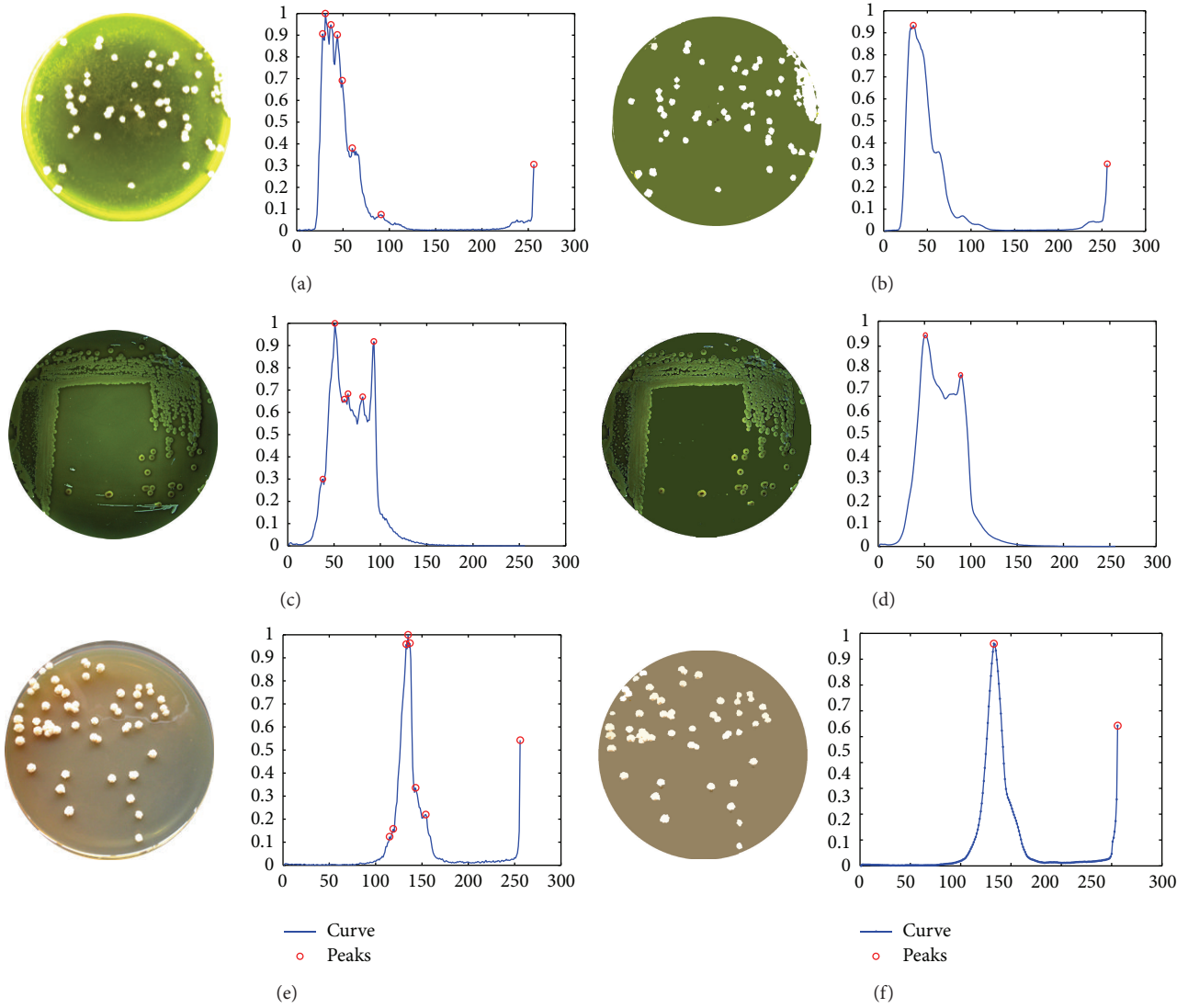


FIGURE 6: Colony imaging and morphological feature extract.

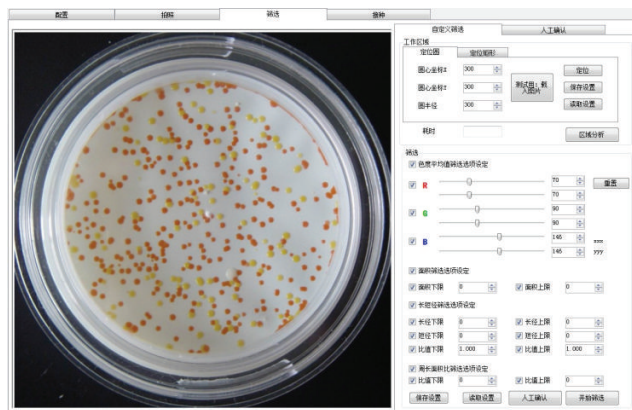


FIGURE 7: Interface of colony screening.

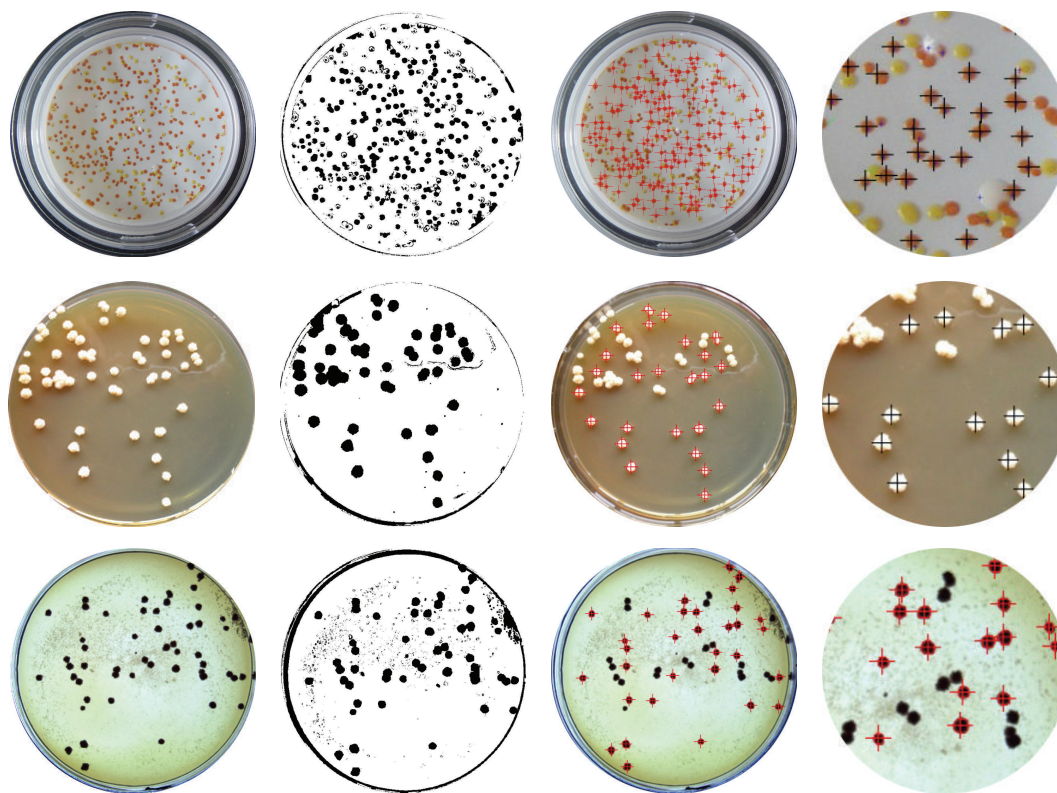


FIGURE 8: Adaptive colony segmentation based on morphological features.

the corresponding segmentation results using thresholding. The first column is original images, the second column is image process based on our approach, the third column is the identification results, and the fourth column is the local zooming of the screening. Meanwhile, we calculate the time consumption of the colony screen. The process of using the thresholding method took 2.57 s and the process of using the region growing method took 8.61 seconds.

5. Conclusions

In this paper, we have deployed an approach to perform adaptive colony segmentation in unstructured environments using feature extraction and selection in an intelligence classifier. We used the intensity histogram peaks as features. To properly determine the importance of the extracted features for colony classification, we used an unascertained theory based LSSVM classification algorithm. Experimental results show that this new approach had better performance than other state-of-the-art techniques in terms of accuracy and speed. This approach works well for adaptive colony segmentation, whilst optimizing the time consumption of colony picking.

Conflict of Interests

The authors declare that there is no conflict of interests regarding the publication of this paper.

Acknowledgments

This work was supported by the National Key Scientific Instrument and Equipment Development Projects (2012YQ15008703 and 2012YQ15008702).

References

- [1] T. Hartley, C. Stewart, R. Stewart, and D. J. Munroe, "Cost-effective addition of high-throughput colony picking capability to a standard liquid-handling platform," *Journal of the Association for Laboratory Automation*, vol. 14, no. 1, pp. 22–26, 2009.
- [2] J. Romeo, G. Pajares, M. Montalvo, J. M. Guerrero, M. Guijarro, and A. Ribeiro, "Crop row detection in maize fields inspired on the human visual perception," *The Scientific World Journal*, vol. 2012, Article ID 484390, 10 pages, 2012.
- [3] R. K. Justice, E. M. Stokely, J. S. Strobel, R. E. Ideker, and W. M. Smith, "Medical image segmentation using 3-D seeded region growing," in *Medical Imaging 1997: Image Processing*, vol. 3034 of *Proceedings of SPIE*, pp. 900–910, February 1997.
- [4] J. A. Solves Llorens, M. J. Rupérez, C. Monserrat, E. Feliu, M. García, and M. Lloret, "Segmentation of the breast skin and its influence in the simulation of the breast compression during an x-ray mammography," *The Scientific World Journal*, vol. 2012, Article ID 876489, 8 pages, 2012.
- [5] H. Y. Zhou, G. Schaefer, A. H. Sadka, and M. E. Celebi, "Anisotropic mean shift based fuzzy C-means segmentation of dermoscopy images," *IEEE Journal on Selected Topics in Signal Processing*, vol. 3, no. 1, pp. 26–34, 2009.

- [6] J. G. Kuk and N. I. Cho, "Weighted gradient domain image processing problems and their iterative solutions," *Eurasip Journal on Image and Video Processing*, vol. 2013, 2013.
- [7] H. Hrizi and N. Sboui, "Reducing the numerical calculation in the wave iterative method by image processing techniques," *Applied Computational Electromagnetics Society Journal*, vol. 27, no. 6, pp. 524–531, 2012.
- [8] Y. Awatsuji and T. Kubota, "Two-dimensional H-tree parallel optical interconnect for two-dimensional image by using optical iterative processing," *IEEE Photonics Technology Letters*, vol. 13, no. 1, pp. 79–81, 2001.
- [9] J. S. Jrgensen, E. Y. Sidky, and X. C. Pan, "Quantifying admissible undersampling for sparsity-exploiting iterative image reconstruction in X-Ray CT," *IEEE Transactions on Medical Imaging*, vol. 32, no. 2, pp. 460–473, 2013.
- [10] L. F. Zhao and Z. H. Xi, "Halo inhibition algorithm based on mean shift filter," *Systems Engineering and Electronics*, vol. 35, no. 7, pp. 1558–1563, 2013.
- [11] H. Han and K. Sohn, "Automatic illumination and color compensation using mean shift and sigma filter," *IEEE Transactions on Consumer Electronics*, vol. 55, no. 3, pp. 978–986, 2009.
- [12] F. Sahba and A. Venetsanopoulos, "Breast mass detection using bilateral filter and mean shift based clustering," in *Proceedings of the International Conference on Signal Processing and Multimedia Applications*, pp. 88–94, July 2010.
- [13] H. Zhang, J. E. Fritts, and S. A. Goldman, "An entropy-based objective evaluation method for image segmentation," in *Storage and Retrieval Methods and Applications for Multimedia*, M. M. Yeung, R. W. Lienhart, and C. S. Li, Eds., vol. 5307 of *Proceedings of SPIE*, pp. 38–49, January 2004.
- [14] B. Chen, Y. Zhu, J. Hu, and M. Zhang, "On optimal estimations with minimum error entropy criterion," *Journal of the Franklin Institute*, vol. 347, no. 2, pp. 545–558, 2010.
- [15] T. Zeng, R. Wang, and F. Li, "SAR image autofocus utilizing minimum-entropy criterion," *IEEE Geoscience and Remote Sensing Letters*, vol. 10, no. 6, pp. 1552–1556, 2013.
- [16] Y. A. Ghassabeh, T. Linder, and G. Takahara, "On some convergence properties of the subspace constrained mean shift," *Pattern Recognition*, vol. 46, no. 11, pp. 3140–3147, 2013.
- [17] V. N. Vapnik, *The Nature of Statistical Learning Theory*, Springer, New York, NY, USA, 2000.
- [18] Y. Wen, Y. Lu, and P. Shi, "Handwritten Bangla numeral recognition system and its application to postal automation," *Pattern Recognition*, vol. 40, no. 1, pp. 99–107, 2007.
- [19] N. M. Khan, R. Ksantini, I. S. Ahmad, and B. Boufama, "A novel SVM+NDA model for classification with an application to face recognition," *Pattern Recognition*, vol. 45, no. 1, pp. 66–79, 2012.
- [20] H. Zhou, G. Schaefer, M. E. Celebi, F. Lin, and T. Liu, "Gradient vector flow with mean shift for skin lesion segmentation," *Computerized Medical Imaging and Graphics*, vol. 35, no. 2, pp. 121–127, 2011.
- [21] J. A. K. Suykens and J. Vandewalle, "Least squares support vector machine classifiers," *Neural Processing Letters*, vol. 9, no. 3, pp. 293–300, 1999.
- [22] T. E. J. Behrens, M. W. Woolrich, M. E. Walton, and M. F. S. Rushworth, "Learning the value of information in an uncertain world," *Nature Neuroscience*, vol. 10, no. 9, pp. 1214–1221, 2007.
- [23] W. Li and G. X. Wang, "A purchase model with unascertained information," in *Proceedings of the 5th International Conference on Machine Learning and Cybernetics*, pp. 1840–1844, August 2006.
- [24] P. K. Parlewar and K. M. Bhurchandi, "A 4-quadrant curvelet transform for denoising digital images," *International Journal of Automation and Computing*, vol. 10, no. 3, pp. 217–226, 2013.
- [25] X. H. Wang, H. Wang, and Z. Y. Qui, "Vehicles detection based an adaptive median filter," *International Journal of Advances in Computing Technology*, vol. 4, no. 6, pp. 219–225, 2012.
- [26] Z. Zhang and G. Zhao, "Butterworth filter and Sobel edge detection to image," in *Proceedings of the 2nd International Conference on Multimedia Technology*, pp. 254–256, July 2011.
- [27] S. K. Shevade, S. S. Keerthi, C. Bhattacharyya, and K. R. K. Murthy, "Improvements to the SMO algorithm for SVM regression," *IEEE Transactions on Neural Networks*, vol. 11, no. 5, pp. 1188–1193, 2000.
- [28] W. J. Liao and Z. Balzen, "LSSVM network flow prediction based on the self-adaptive genetic algorithm optimization," *Journal of Networks*, vol. 8, no. 2, pp. 507–512, 2013.
- [29] H. Ma, J. Chan, T. K. Saha, and C. Ekanayake, "Pattern recognition techniques and their applications for automatic classification of artificial partial discharge sources," *IEEE Transactions on Dielectrics and Electrical Insulation*, vol. 20, no. 2, pp. 468–478, 2013.

Research Article

Adaptive Neuro-Fuzzy Inference System for Classification of Background EEG Signals from ESES Patients and Controls

Zhixian Yang,¹ Yinghua Wang,^{2,3} and Gaoxiang Ouyang^{2,3}

¹ Department of Pediatrics, Peking University First Hospital, No. 1 of Xian Men Street, Xicheng District, Beijing 100034, China

² State Key Laboratory of Cognitive Neuroscience and Learning and IDG/McGovern Institute for Brain Research, Beijing Normal University, Beijing 100875, China

³ Center for Collaboration and Innovation in Brain and Learning Sciences, Beijing Normal University, Beijing 100875, China

Correspondence should be addressed to Gaoxiang Ouyang; ouyang@bnu.edu.cn

Received 13 December 2013; Accepted 18 March 2014; Published 25 March 2014

Academic Editors: J. Tang and H. Zhou

Copyright © 2014 Zhixian Yang et al. This is an open access article distributed under the Creative Commons Attribution License, which permits unrestricted use, distribution, and reproduction in any medium, provided the original work is properly cited.

Background electroencephalography (EEG), recorded with scalp electrodes, in children with electrical status epilepticus during slow-wave sleep (ESES) syndrome and control subjects has been analyzed. We considered 10 ESES patients, all right-handed and aged 3–9 years. The 10 control individuals had the same characteristics of the ESES ones but presented a normal EEG. Recordings were undertaken in the awake and relaxed states with their eyes open. The complexity of background EEG was evaluated using the permutation entropy (PE) and sample entropy (SampEn) in combination with the ANOVA test. It can be seen that the entropy measures of EEG are significantly different between the ESES patients and normal control subjects. Then, a classification framework based on entropy measures and adaptive neuro-fuzzy inference system (ANFIS) classifier is proposed to distinguish ESES and normal EEG signals. The results are promising and a classification accuracy of about 89% is achieved.

1. Introduction

Encephalopathy with electrical status epilepticus during slow-wave sleep (ESES) syndrome is a condition characterized by continuous spikes and waves occurring during sleep [1]. The recent literature refers to it as “ESES syndrome,” which is an age-related reversible disorder with onset at around 4–5 years of age and a generally favorable course with disappearance at around 10–15 years of age [2], usually associated with variable cognitive and behavioral impairments [3, 4]. The pathophysiological mechanisms and neuropsychological deficits associated with this condition are still poorly understood [5]. Therefore, it is important to identify the ESES patients as early as possible such that the clinician can prescribe the necessary medication to stop its progression.

The electroencephalograph (EEG) signal is a measure of the summed activities of approximately 1–100 million neurons lying in the vicinity of the recording electrode. Since it may provide insight into the functional structure and

dynamics of the brain [6], exploration of hidden dynamical structures within EEG signals is of both basic and clinical interest and has attracted more and more attention [7–9]. One can assume that the EEG is a signal containing information about the condition of the brain. We can also accept as working hypothesis that the EEG recorded under resting conditions is representative of the global state of the brain [10, 11]. Then, a plausible working hypothesis is that background EEG corresponding to healthy controls is different from that corresponding to patients with pathologies (e.g., ESES). However, it is currently accepted that a human observer hardly discriminates EEG traces of healthy controls from those of ESES subjects. Quantitative EEG analysis using computational methods can therefore assist in the background EEG characterization. The EEG pattern classification scheme usually includes two major parts: feature extraction and classification.

Various methods have been widely used for feature extraction ranging from traditional linear methods such

as Fourier transforms and spectral analysis [12] to nonlinear methods such as Lyapunov exponents [13], correlation dimension [14], and similarity [15, 16]. Due to the complex interconnections between billions of neurons, the recorded EEG signals are complex, nonlinear, nonstationary, and random in nature. Therefore, the classification of EEG signals using nonlinear methods that detect and quantify nonlinear mechanisms and thereby better reflect the characteristics of the EEG signals. Nonlinear features may be able to unearth the hidden complexities existing in the EEG time series. Ferri et al. applied the nonlinear cross-prediction test to assess the dynamic properties of the EEG and showed that ESES, like other types of epileptic EEG activities, seems to reflect highly nonlinear and possibly low-dimensional dynamics, whereas non-ESES waking EEG seems to correspond with linear stochastic dynamics [17]. In the recent years, a series of entropy-based approaches have been widely used since they can quantify the complexity (regularity) of an EEG signal [18, 19]. The entropy of the EEG may act as a reliable indicator of changes in cortical neuronal interactions and truly reflect the intracortical information flow [20], and thus the term “entropy” may be more than merely a statistical measure of EEG patterns, which are well exploited using entropies, and it helps in providing distinguishable variation for normal and abnormal biomedical signals [21, 22]. Abásolo et al. applied the approximate entropy (ApEn) to analyse the EEG background activity of Alzheimer’s disease (AD) patients and age-matched controls. They found that ApEn is significantly lower in the AD patients at electrodes P3 and P4 [23]. Then, the spectral entropy (SpecEn) and sample entropy (SampEn) were used to analyse the EEG background activity of AD patients and showed that AD patients have significantly lower SampEn values than control subjects at electrodes P3, P4, O1, and O2 but no differences between AD patients and control subjects’ EEGs with SpecEn [24]. Burioka et al. found that the ApEn values of EEG signals in absence epilepsy during seizure-free intervals are very similar to those of healthy subjects, but the EEG signals in absence epilepsy during seizure intervals produce significant lower ApEn values than healthy subjects [25]. In the study by Kannathal et al., ApEn was used to investigate the epileptic seizure detection, where three other entropy-based features were extracted and combined with ApEn for studying normal and epileptic EEG signals [26]. A novel feature extraction method based on ApEn, SampEn, and phase entropy was proposed for diagnosing the epileptic EEG signals and showed that the extracted features with fuzzy classifier are able to differentiate the EEGs with a high accuracy [27]. The high identification accuracy was also reported in the study by Song et al. [28], in which they developed a new scheme of automatic epileptic seizure detection on the basis of SampEn feature extraction.

Recently, Bandt and Pompe proposed the permutation entropy (PE) method to measure the irregularity (complexity) of nonstationary time series [29]. The basic idea is to consider order relations between the values of a time series rather than the values themselves. Compared with ApEn and SampEn [21, 22], the advantages of the PE method are its simplicity, low complexity in computation without further model assumptions, and robustness in the presence

of observational and dynamical noise [29–31]. Cao et al. used PE to identify various phases of epileptic activity in the intracranial EEG signals recorded from three patients suffering from intractable epilepsy [32]. Li et al. used PE as a feature to predict the absence seizures in genetic absence epilepsy rats and showed a sharp PE drop after the seizures [33]. It was also found that the PE can better extract the pattern of EEG data for the prediction of absence seizure than the SampEn measure. Nicolaou and Georgiou investigated the use of PE as a feature for automated epileptic seizure detection [34]. Bruzzo et al. applied PE to detect vigilance changes and the preictal phase from scalp EEG in three epileptic patients [35]. These results showed that the EEG during epileptic seizures is characterized by a lower value of PE than the normal EEG. It was found that there is a good separability between the seizure-free phase and the pre-seizure phase and the changes of PE values during the pre-seizure phase and seizure onset coincide with changes in vigilance state [35].

In terms of classifiers, lots of methodologies have been proposed and applied to process and discriminate biomedical signals [36–38], such as electromyography [39, 40] and EEG signals [41, 42]. In particular, artificial neural networks have been utilized as the most common method for classifying the EEGs. Moreover, fuzzy set theory plays an important role in dealing with uncertainty when making decisions in medical applications. Therefore, fuzzy sets have attracted the growing attention and interest in data analysis, decision making, pattern recognition, diagnostics, and so forth [43, 44]. Neuro-fuzzy systems are fuzzy systems which use ANNs theory in order to determine their properties (fuzzy sets and fuzzy rules) by processing data samples [45]. A specific approach in neuro-fuzzy development is the adaptive neuro-fuzzy inference system (ANFIS), which has shown significant results in classification of EEG signals. Kannathal et al. proposed a novel classification framework based on entropy measures and ANFIS classifier to distinguish normal and epileptic EEG signals [26]. Güler and Übeyli proposed a new scheme using ANFIS and wavelet transform as the classifier, which can identify five types of EEG signals with a recognition rate greater than 98% [45]. Übeyli proposed a system using Lyapunov exponents of EEG signals and ANFIS as the classifier, which can identify these five types of EEG signals with a recognition rate greater than 99% [46]. In the study by Yildiz et al. [47], a wavelet entropy-ANFIS framework is proposed for classifying a state of vigilance as alert, drowsy, or sleep state on an ongoing EEG recording. A classification accuracy of more than 98% is achieved. These results show that ANFIS has potential in classifying the EEG signals.

In this study, a new approach based on ANFIS employing PE and SampEn measures was presented for classification of background EEG signals from ESES patients and controls. The proposed technique involved training the two ANFIS classifiers to classify the two classes of the EEG signals when PE and SampEn of the EEG signals were used as inputs. The goal was to find a clear differentiation between background EEG corresponding to a sample set of ESES patients and that corresponding to healthy control individuals. The paper is

TABLE 1: Summary of the EEG data.

	Set 1	Set 2
Subjects	10 healthy subjects	10 ESES patients
Age	3–9 years 4 males and 6 females	3–9 years 4 males and 6 females
Patient's state	Awake and eyes open (normal)	Awake and eyes open (no spikes)
Number of epochs	100	100
Epoch duration (s)	8	8

organized as follows. Section 2 presents a description of the data used in this work and briefly describes the extracted features and classifiers that were used. Section 3 presents the results obtained. Finally, conclusions are given in Section 4.

2. Materials and Methods

2.1. EEG Data. The EEG data used in this study consists of two different sets. The first set includes EEG recordings that were collected from 10 right-handed healthy subjects. The subjects were awake and relaxed with their eyes open. 100 16-channel EEG epochs of 8 s duration were selected and cut out from each continuous EEG recording after visual inspection for artifacts, for example, due to muscle activity or eye movements. The second set was obtained from 10 patients with ESES, all right-handed. The data set consists of EEG recordings during wakeful state. Similar to healthy data, noise-free segments are selected from the EEG recordings with ESES patients and used for the analysis. All EEG data were recorded by the Nihon Kohden digital video EEG system from a standard international 10–20-electrode placement (Fp1, Fp2, F3, F4, C3, C4, P3, P4, O1, O2, F7, F8, T3, T4, T5, and T6). They were sampled at a frequency of 500 Hz using a 16-bit analogue-to-digital converter and filtered within a frequency band from 0.5 to 35 Hz.

The study protocol had previously been approved by the Ethics Committee of Peking University First Hospital and the patients had signed informed consent that their clinical data might be used and published for research purposes. A summary of the data set is given in Table 1. A sample of EEG epochs from each of the two data sets is plotted in Figure 1.

2.2. Sample Entropy. Sample entropy (SampEn) is an algorithm derived from approximate entropy (ApEn) [21]. Introduced by Pincus et al. [48], ApEn is a technique that is useful in determining changing system complexity and it finds application in biomedical research [49]. The first step in computing ApEn of an EEG series $\{x_1, x_2, \dots, x_N\}$ is to form a sequence of vectors $X_1, X_2, \dots, X_{N-m+1}$ in R^m , defined by $X_i = [x_i, x_{i+1}, \dots, x_{i+m-1}]$ and $X_j = [x_j, x_{j+1}, \dots, x_{j+m-1}]$. Next, we define, for each i ,

$$C_i^m(r) = \frac{i}{N-m+1} \sum_{j=1}^i \theta(r - d(X_i, X_j)), \quad (1)$$

where θ is the standard Heaviside function and $\theta(x) = 1$ for $x > 0$, $\theta(x) = 0$, otherwise; r is a tolerance threshold and $d(X_i, X_j)$ is a distance measure defined by

$$d(X_i, X_j) = \max(|x_{i+k-1} - x_{j+k-1}|), \quad k = 1, 2, \dots, m. \quad (2)$$

Then, we define $\phi^m(r)$ as

$$\phi^m(r) = \frac{1}{N-m+1} \sum_{i=1}^{N-m+1} \log C_i^m(r). \quad (3)$$

For fixed m and r , ApEn is given by the following formula:

$$\text{ApEn}(m, r, N) = \phi^m(r) - \phi^{m+1}(r) \quad (4)$$

which is basically the logarithmic likelihood that runs of patterns of length m that are close (within r) will remain close on next incremental comparisons. The more regular the EEG is, the smaller the ApEn will be. The exact value of the $\text{ApEn}(m, r, N)$ will depend on three parameters: N (length of the time series), m (length of sequences to be compared), and r (tolerance threshold for accepting matches).

The ApEn specifies a tolerance threshold and so may be better than spectral entropy in the quantification of complexity of EEG recording [50]. The disadvantage of ApEn is that it is heavily dependent on the record length and is often lower than expected for short records. Another disadvantage is that ApEn lacks relative consistency [21]. To overcome the disadvantages of ApEn, a sample entropy (SampEn) was proposed to replace ApEn. By excluding self-matches [21], SampEn reduces the computing time by one-half in comparison with ApEn. Another advantage of SampEn is that it is largely independent of record length and displays relative consistency [51]. The key idea that differentiates SampEn from ApEn is using the correlation sum $C^m(r)$ in the entropy definition instead of the $\phi^m(r)$ functions defined in (3)—practically, the position of the log function changes. Thus, Richman and Moorman defined sample entropy as

$$\text{SampEn}(m, r, N) = \log \frac{C^m(r)}{C^{m+1}(r)}. \quad (5)$$

The choice of input parameters has been discussed by Pincus and Goldberger in [52]. They concluded that, for $m = 2$, values of r from 0.1 to 0.25 SD (the standard deviation of the signal) produce good statistical validity of SampEn. In this study, SampEn was estimated with $m = 2$ and $r = 0.2 \times \text{SD}$ of the EEG epoch.

2.3. Permutation Entropy. Bandt and Pompe proposed a new permutation method to map a continuous time series onto a symbolic sequence [29], where the statistics of the symbolic sequences was called permutation entropy (PE). PE refers to the local order structure of the time series, which can give a quantitative complexity measure for a dynamical time series [53]. Given a time series $\{x_1, x_2, \dots, x_N\}$, an embedding procedure was used to generate $N - (m - 1)l$ vectors $X_1, X_2, \dots, X_{N-(m-1)l}$ defined by $X_t = [x_t, x_{t+1}, \dots, x_{t+(m-1)l}]$

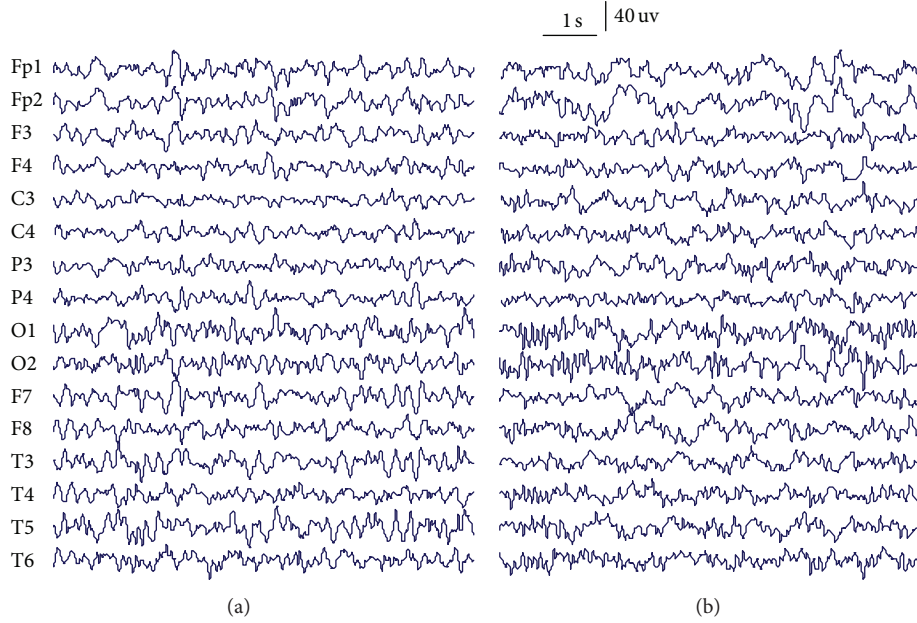


FIGURE 1: Sample EEG epochs from both ESES patient (a) and control subject (b).

with the embedding dimension m and the lag l . The vector X_t can be rearranged in an ascending order as $[x_{t+(j_1-1)l} \leq x_{t+(j_2-1)l} \dots \leq x_{t+(j_m-1)l}]$. For m different numbers, there will be $m!$ possible order patterns π , which are also called permutations. Then, we can count the occurrences of the order pattern π_i , which is denoted as $C(\pi_i)$, $i = 1, 2, \dots, m!$. Its relative frequency is calculated by $p(\pi) = C(\pi)/(N - (m-1)l)$. The PE is defined as

$$PE = - \sum_{\pi=1}^{m!} p(\pi) \ln p(\pi). \quad (6)$$

The largest value of PE is $\log(m!)$, which means that the time series is completely random; the smallest value of PE is zero, indicating that the time series is very regular. More details can be found in [29].

PE calculation depends on the selection of dimension m and lag l . When m is too small (less than 3), the scheme will not work well since there are only a few distinct states for EEG recordings. On the other hand, the length of EEG recording should be larger than m in order to achieve a proper differentiation between stochastic and deterministic dynamics [31]. In order to allow every possible order pattern of dimension m to occur in a time series of length N , the condition $m! \leq N - (m-1)l$ must hold. Moreover, $N \gg m! + (m-1)l$ is required to avoid undersampling [54]. In this study, we therefore choose the dimension $m = 5$ when calculating PE. The lag l is referred to as the number of sample points spanned by each section of the vector. The importance of the lag is that it gives the resultant fraction characteristics of the vector. In practice, an autocorrelation function (ACF) of a signal can be employed to automated determination of the lag l . An optimal lag can be found at the point where the ACF has firstly decayed to e^{-1} of its peak value [55].

2.4. Adaptive Neuro-Fuzzy Inference System. The ANFIS described by Jang [56] is adopted to evaluate the ability and effectiveness of the above entropy measures in classifying the EEG from the ESES patients and control subjects. The ANFIS learns features in the data set and adjusts the system parameters according to a given error criterion. It has been widely used in analysing the biological signals. In order to improve the generalization, ANFIS classifiers are trained with the backpropagation gradient descent method in combination with the least squares method. In this study, two ANFIS classifiers are trained with the backpropagation gradient descent method in combination with the least squares method when 16 features (dimension of the extracted feature vectors; entropy measures from 16-channel EEG) are used as inputs. The samples with target outputs ESES patients and control subjects are given the binary target values of (1, 0) and (0, 1), respectively. The fuzzy rule architecture of the ANFIS classifiers was designed by using a generalized bell-shaped membership function defined as follows:

$$\mu_{ji}(x_i) = \left(1 + \left[\frac{x_i - c_{ji}}{a_{ji}} \right]^{2b_{ji}} \right)^{-1}, \quad (7)$$

where (a_{ji}, b_{ji}, c_{ji}) are adaptable parameters.

Next, two first-order Sugeno-type ANFIS models with 16 inputs and one output are implemented. The first-order Sugeno fuzzy models have rules of the following form:

$$R_i : \text{IF } (x_1 \text{ is } U_{i1} \dots x_m \text{ is } U_{im})$$

$$\text{THEN } y \text{ is } g_i(x_1, \dots, x_m) = b_0 + b_1 x_1 + \dots + b_m x_m, \quad (8)$$

where R_i is the i th rule of the fuzzy system, x_i ($i = 1, \dots, m$) are the inputs to the fuzzy system, and y is the output of the

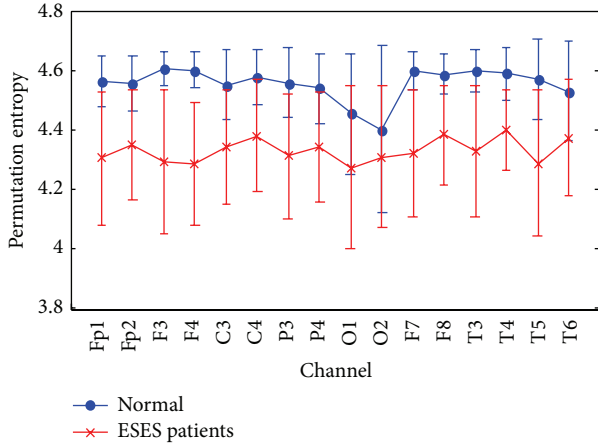


FIGURE 2: The averaged PE on channel of all EEG recordings, grouped by ESES patients and normal control subjects. Symbols represent the mean values of PE for each group and bars represent the standard error.

fuzzy system; b_i ($i = 0, 1, \dots, m$) are adaptable parameters. The ANFIS output is given by

$$F = \frac{\sum_j g_j(a_1, a_2, \dots, a_m) \Pi_i \mu_{U_{ji}}(a_i)}{\sum_j \Pi_i \mu_{U_{ji}}(a_i)}, \quad (9)$$

where $\mu_{U_{ji}}(a_i)$ is the degree of membership of a_i ($i = 1, 2, \dots, m$) to the antecedent linguistic term U_{ji} for the i th rule of the fuzzy system. Each ANFIS classifier is implemented by using the MATLAB software package (MATLAB version 7.0 with fuzzy logic toolbox).

3. Results

3.1. Entropy Measures of EEG. EEG epochs from both ESES patients and normal control subjects are investigated in this study. First, PE is applied to analyse the EEG recordings, with $m = 5$, for channels Fp1, Fp2, F3, F4, C3, C4, P3, P4, O1, O2, F7, F8, T3, T4, T5, and T6. The results have been averaged based on all the artefact-free 8 s epochs for each channel. The averaged PEs of all channels are shown in Figure 2. Symbols represent the mean values of PE for each group and bars represent the standard error. It can be found that the PE values of EEG epochs in normal control subjects are much larger than those in ESES patients. The PE values (mean \pm SD) for the control subjects and ESES patients and the P values of the one-way ANOVA test performed to examine the differences between both groups are summarized in Table 2. It can be seen that ESES patients have significant lower PE values at all 16 electrodes. These results suggest that EEG activity of ESES patients is less complex (more regular) than in a normal control subject. This result supports the view that ESES, like other types of epileptic EEG activity, would reflect low complex and high nonlinear dynamics, whereas non-ESES waking EEG would correspond with high complex dynamics.

To compare the extracted entropy information of EEG between PE and SampEn methods, SampEn is estimated for

TABLE 2: The average PE values (mean \pm SD) of the EEGs for the normal control subjects and ESES patients for all channels.

Electrode	Normal subjects	ESES patients	P value
Fp1	4.563 \pm 0.088	4.304 \pm 0.224	$P < 0.05$
Fp2	4.555 \pm 0.089	4.349 \pm 0.184	$P < 0.05$
F3	4.606 \pm 0.055	4.292 \pm 0.240	$P < 0.05$
F4	4.600 \pm 0.060	4.286 \pm 0.206	$P < 0.05$
C3	4.550 \pm 0.116	4.341 \pm 0.192	$P < 0.05$
C4	4.579 \pm 0.092	4.381 \pm 0.190	$P < 0.05$
P3	4.556 \pm 0.117	4.311 \pm 0.212	$P < 0.05$
P4	4.539 \pm 0.116	4.343 \pm 0.183	$P < 0.05$
O1	4.454 \pm 0.204	4.272 \pm 0.273	$P < 0.05$
O2	4.402 \pm 0.278	4.308 \pm 0.237	$P < 0.05$
F7	4.595 \pm 0.064	4.321 \pm 0.215	$P < 0.05$
F8	4.585 \pm 0.067	4.382 \pm 0.168	$P < 0.05$
T3	4.598 \pm 0.072	4.331 \pm 0.220	$P < 0.05$
T4	4.588 \pm 0.090	4.402 \pm 0.135	$P < 0.05$
T5	4.571 \pm 0.135	4.289 \pm 0.248	$P < 0.05$
T6	4.529 \pm 0.167	4.374 \pm 0.195	$P < 0.05$

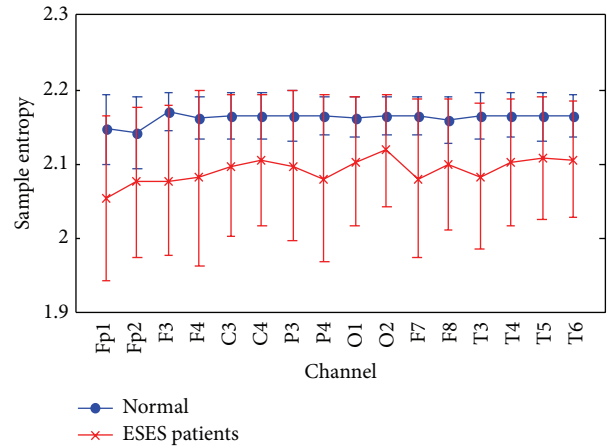


FIGURE 3: The averaged SampEn on channel of all EEG recordings, grouped by ESES patients and normal control subjects. Symbols represent the mean values of SampEn for each group and bars represent the standard error.

channels Fp1, Fp2, F3, F4, C3, C4, P3, P4, O1, O2, F7, F8, T3, T4, T5, and T6 with $m = 2$ and $r = 0.2 \times \text{SD}$ of the original data sequence. The averaged SampEns of all channels are shown in Figure 3. It can be found that the SampEn values of EEG epochs in normal control subjects are also larger than those in ESES patients. However, the SampEn values in control subjects and ESES patients are more overlapped than those of the PE values. Then, the SampEn values (mean \pm SD) for the control subjects and ESES patients and the P values of the one-way ANOVA test performed to examine the differences between both groups are summarized in Table 3. It can be seen that ESES patients have significant lower SampEn values at all 16 electrodes.

TABLE 3: The average SampEn values (mean \pm SD) of the EEGs for the normal control subjects and ESES patients for all channels.

Electrode	Normal subjects	ESES patients	<i>P</i> value
Fp1	2.147 \pm 0.045	2.055 \pm 0.111	<i>P</i> < 0.05
Fp2	2.144 \pm 0.048	2.077 \pm 0.101	<i>P</i> < 0.05
F3	2.171 \pm 0.026	2.078 \pm 0.101	<i>P</i> < 0.05
F4	2.163 \pm 0.029	2.082 \pm 0.118	<i>P</i> < 0.05
C3	2.166 \pm 0.032	2.098 \pm 0.095	<i>P</i> < 0.05
C4	2.166 \pm 0.031	2.107 \pm 0.088	<i>P</i> < 0.05
P3	2.166 \pm 0.034	2.098 \pm 0.100	<i>P</i> < 0.05
P4	2.165 \pm 0.025	2.081 \pm 0.111	<i>P</i> < 0.05
O1	2.163 \pm 0.027	2.103 \pm 0.087	<i>P</i> < 0.05
O2	2.165 \pm 0.025	2.119 \pm 0.101	<i>P</i> < 0.05
F7	2.165 \pm 0.026	2.081 \pm 0.106	<i>P</i> < 0.05
F8	2.161 \pm 0.031	2.099 \pm 0.088	<i>P</i> < 0.05
T3	2.165 \pm 0.032	2.083 \pm 0.098	<i>P</i> < 0.05
T4	2.166 \pm 0.030	2.102 \pm 0.085	<i>P</i> < 0.05
T5	2.164 \pm 0.032	2.109 \pm 0.083	<i>P</i> < 0.05
T6	2.166 \pm 0.029	2.107 \pm 0.077	<i>P</i> < 0.05

TABLE 4: Classification results with PE measure.

Desired result	Output result	
	ESES patients	Normal subjects
ESES patients	96	4
Normal subjects	18	82

3.2. Classification. As shown above, both PE and SampEn values of EEG were significantly different between ESES patients and normal control subjects. The performance of the above measures to discriminate among groups is also evaluated by means of ANFIS classifier, and 10-fold cross-validations are employed to demonstrate the accuracy of classification. First, the ability of the PE in classifying different EEG epochs is evaluated using the ANFIS. Two ANFIS classifiers are trained with the backpropagation gradient descent method in combination with the least squares method when the calculated PE values are used as input. Each of the ANFIS classifiers is trained so that they are likely to be more accurate for one state of EEG signals than the other state. Samples with target outputs sets are given the binary target values of (1, 0) and (0, 1), respectively. Each ANFIS classifier is implemented by using the MATLAB software package (MATLAB version 7.0 with fuzzy logic toolbox). The classification results are illustrated in Table 4. Of 200 EEG epochs in two groups, 178 are classified correctly. Only 4 normal EEG epochs are classified incorrectly by ANFIS as ESES EEG epochs and 18 ESES EEG epochs are classified as normal EEG epochs. The classification accuracy was 89.0%, which is defined as the percentage ratio of the number of epochs correctly classified to the total number of epochs considered for classification.

Then, in order to compare the classification accuracy of PE method with that of the SampEn method, the calculated SampEn values were used as the input data in the ANFIS classifiers, and 10-fold cross-validations were employed to

TABLE 5: Classification results with SampEn measure.

Desired result	Output result	
	ESES patients	Normal subjects
ESES patients	92	8
Normal subjects	28	72

demonstrate the performance of classification. The classification results are listed in Table 5. Of 200 EEG epochs in two groups, 164 were classified correctly. The total classification accuracy was 82.0%. Therefore, it is found that the PE measures can provide a better separability between ESES patients and normal control subjects than the SampEn measures.

4. Conclusions

In this study, we have analysed the complexity characteristics in background EEG signals from ESES patients and controls using the entropy measures. Although the background EEG marked was indeed “normal” to standard visual inspection, the proposed methodology based on entropy measures, plus ANOVA statistical test, demonstrates that the background EEG in ESES patients does differ from that in controls. It can be seen that there is a significant increase of the calculated PE and SampEn values of the EEG epochs from ESES patients to control subjects. Then, a new approach based on ANFIS employing entropy measures was presented for classification of background EEG signals from ESES patients and controls. The two ANFIS classifiers were used to classify two classes of EEG epochs when the PE and SampEn of the EEG epochs were used as inputs. The experimental results showed that the classification accuracy, 89%, based on the PE measures is much higher than that with the SampEn measures, 82%. These results suggest that the proposed ANFIS combined with PE measures might be a potential tool to classify the background EEG from ESES patients and normal control subjects. Our next goal is to confirm the results presented here in a much larger clinical cohort of ESES patients.

Conflict of Interests

The authors declare that there is no conflict of interests regarding the publication of this paper.

Acknowledgments

This research was supported by National Natural Science Foundation of China (61025019, 61105027), Beijing Natural Science Foundation (4143063), the Fundamental Research Funds for the Central Universities, and the Peking-Tsinghua Center for Life Sciences.

References

- [1] G. Patry, S. Lyagoubi, and C. A. Tassinari, “Subclinical “electrical status epilepticus” induced by sleep in children. A clinical and electroencephalographic study of six cases,” *Archives of Neurology*, vol. 24, no. 3, pp. 242–252, 1971.

- [2] C. A. Tassinari, G. Rubboli, L. Volpi et al., "Encephalopathy with electrical status epilepticus during slow sleep or ESES syndrome including the acquired aphasia," *Clinical Neurophysiology*, vol. 111, supplement 2, pp. S94–S102, 2000.
- [3] F. B. J. Scholtes, M. P. H. Hendriks, and W. O. Renier, "Cognitive deterioration and electrical status epilepticus during slow sleep," *Epilepsy and Behavior*, vol. 6, no. 2, pp. 167–173, 2005.
- [4] S. Raha, U. Shah, and V. Udani, "Neurocognitive and neurobehavioral disabilities in epilepsy with electrical status epilepticus in slow sleep (ESES) and related syndromes," *Epilepsy and Behavior*, vol. 25, pp. 381–385, 2012.
- [5] M. Siniatchkin, K. Groening, J. Moehring et al., "Neuronal networks in children with continuous spikes and waves during slow sleep," *Brain*, vol. 133, no. 9, pp. 2798–2813, 2010.
- [6] G. Buzsaki, *Rhythms of the Brain*, Oxford University Press, Oxford, UK, 2006.
- [7] R. A. Sarkis and J. W. Lee, "Quantitative EEG in hospital encephalopathy: review and microstate analysis," *Journal of Clinical Neurophysiology*, vol. 30, pp. 526–530, 2013.
- [8] W. Klimesch, P. Sauseng, and S. Hanslmayr, "EEG alpha oscillations: the inhibition-timing hypothesis," *Brain Research Reviews*, vol. 53, no. 1, pp. 63–88, 2007.
- [9] M. Scheltens-de Boer, "Guidelines for EEG in encephalopathy related to ESES/CSWS in children," *Epilepsia*, vol. 50, no. 7, pp. 13–17, 2009.
- [10] O. A. Rosso, A. Mendes, J. A. Rostas, M. Hunter, and P. Moscato, "Distinguishing childhood absence epilepsy patients from controls by the analysis of their background brain electrical activity," *Journal of Neuroscience Methods*, vol. 177, no. 2, pp. 461–468, 2009.
- [11] O. A. Rosso, A. Mendes, R. Berretta, J. A. Rostas, M. Hunter, and P. Moscato, "Distinguishing childhood absence epilepsy patients from controls by the analysis of their background brain electrical activity (II): a combinatorial optimization approach for electrode selection," *Journal of Neuroscience Methods*, vol. 181, no. 2, pp. 257–267, 2009.
- [12] Z. Rogowski, I. Gath, and E. Bental, "On the prediction of epileptic seizures," *Biological Cybernetics*, vol. 42, no. 1, pp. 9–15, 1981.
- [13] L. D. Iasemidis, J. C. Sackellares, H. P. Zaveri, and W. J. Williams, "Phase space topography and the lyapunov exponent of electrocorticograms in partial seizures," *Brain Topography*, vol. 2, no. 3, pp. 187–201, 1990.
- [14] R. G. Andrzejak, K. Lehnertz, F. Mormann, C. Rieke, P. David, and C. E. Elger, "Indications of nonlinear deterministic and finite-dimensional structures in time series of brain electrical activity: dependence on recording region and brain state," *Physical Review E: Statistical, Nonlinear, and Soft Matter Physics*, vol. 64, no. 6, Article ID 061907, 2001.
- [15] V. Navarro, J. Martinerie, M. Le van Quyen et al., "Seizure anticipation in human neocortical partial epilepsy," *Brain*, vol. 125, no. 3, pp. 640–655, 2002.
- [16] M. Niknazar, S. R. Mousavi, S. Motaghi, A. Dehghani, B. V. Vahdat, and M. B. Shamsollahi, "A unified approach for detection of induced epileptic seizures in rats using ECoG signals," *Epilepsy and Behavior*, vol. 27, pp. 355–364, 2013.
- [17] R. Ferri, R. Chiaramonti, M. Elia, S. A. Musumeci, A. Ragazzoni, and C. J. Stam, "Nonlinear EEG analysis during sleep in premature and full-term newborns," *Clinical Neurophysiology*, vol. 114, no. 7, pp. 1176–1180, 2003.
- [18] J. Gao, J. Hu, and W.-W. Tung, "Entropy measures for biological signal analyses," *Nonlinear Dynamics*, vol. 68, pp. 431–444, 2011.
- [19] C. Paisansathan, M. D. Ozcan, Q. S. Khan, V. L. Baughman, and M. S. Ozcan, "Signal persistence of bispectral index and state entropy during surgical procedure under sedation," *The Scientific World Journal*, vol. 2012, Article ID 272815, 5 pages, 2012.
- [20] J. W. Sleigh, D. A. Steyn-Ross, M. L. Steyn-Ross, C. Grant, and G. Ludbrook, "Cortical entropy changes with general anaesthesia: theory and experiment," *Physiological Measurement*, vol. 25, no. 4, pp. 921–934, 2004.
- [21] J. S. Richman and J. R. Moorman, "Physiological time-series analysis using approximate and sample entropy," *The American Journal of Physiology—Heart and Circulatory Physiology*, vol. 278, no. 6, pp. H2039–H2049, 2000.
- [22] S. M. Pincus, "Approximate entropy as a measure of system complexity," *Proceedings of the National Academy of Sciences of the United States of America*, vol. 88, pp. 2297–2301, 1991.
- [23] D. Abásolo, R. Hornero, P. Espino, J. Poza, C. I. Sánchez, and R. de la Rosa, "Analysis of regularity in the EEG background activity of Alzheimer's disease patients with Approximate Entropy," *Clinical Neurophysiology*, vol. 116, no. 8, pp. 1826–1834, 2005.
- [24] D. Abásolo, R. Hornero, P. Espino, D. Álvarez, and J. Poza, "Entropy analysis of the EEG background activity in Alzheimer's disease patients," *Physiological Measurement*, vol. 27, no. 3, pp. 241–253, 2006.
- [25] N. Burioka, G. Cornélissen, Y. Maegaki et al., "Approximate entropy of the electroencephalogram in healthy awake subjects and absence epilepsy patients," *Clinical EEG and Neuroscience*, vol. 36, no. 3, pp. 188–193, 2005.
- [26] N. Kannathal, M. L. Choo, U. R. Acharya, and P. K. Sadasivan, "Entropies for detection of epilepsy in EEG," *Computer Methods and Programs in Biomedicine*, vol. 80, no. 3, pp. 187–194, 2005.
- [27] U. R. Acharya, F. Molinari, S. V. Sree, S. Chattopadhyay, K.-H. Ng, and J. S. Suri, "Automated diagnosis of epileptic EEG using entropies," *Biomedical Signal Processing and Control*, vol. 7, pp. 401–408, 2012.
- [28] Y. Song, J. Crowcroft, and J. Zhang, "Automatic epileptic seizure detection in EEGs based on optimized sample entropy and extreme learning machine," *Journal of Neuroscience Methods*, vol. 210, pp. 132–146, 2012.
- [29] C. Bandt and B. Pompe, "Permutation entropy: a natural complexity measure for time series," *Physical Review Letters*, vol. 88, no. 17, Article ID 174102, 2002.
- [30] M. Zanin, L. Zunino, O. A. Rosso, and D. Papo, "Permutation entropy and its main biomedical and econophysics applications: a review," *Entropy*, vol. 14, pp. 1553–1577, 2012.
- [31] G. Ouyang, C. Dang, D. A. Richards, and X. Li, "Ordinal pattern based similarity analysis for EEG recordings," *Clinical Neurophysiology*, vol. 121, no. 5, pp. 694–703, 2010.
- [32] Y. Cao, W. W. Tung, J. B. Gao, V. A. Protopopescu, and L. M. Hively, "Detecting dynamical changes in time series using the permutation entropy," *Physical Review E: Statistical, Nonlinear, and Soft Matter Physics*, vol. 70, no. 4, Article ID 046217, 2004.
- [33] X. Li, G. Ouyang, and D. A. Richards, "Predictability analysis of absence seizures with permutation entropy," *Epilepsy Research*, vol. 77, no. 1, pp. 70–74, 2007.
- [34] N. Nicolaou and J. Georgiou, "Detection of epileptic electroencephalogram based on permutation entropy and support vector machines," *Expert Systems with Applications*, vol. 39, no. 1, pp. 202–209, 2012.
- [35] A. A. Bruzzo, B. Gesierich, M. Santi, C. A. Tassinari, N. Birbaumer, and G. Rubboli, "Permutation entropy to detect

- vigilance changes and preictal states from scalp EEG in epileptic patients. A preliminary study,” *Neurological Sciences*, vol. 29, no. 1, pp. 3–9, 2008.
- [36] S. Baek, C. A. Tsai, and J. J. Chen, “Development of biomarker classifiers from high-dimensional data,” *Briefings in Bioinformatics*, vol. 10, no. 5, pp. 537–546, 2009.
- [37] R. Palaniappan, K. Sundaraj, and N. U. Ahamed, “Machine learning in lung sound analysis: a systematic review,” *Biocybernetics and Biomedical Engineering*, vol. 33, pp. 129–135, 2013.
- [38] H. Zhou, H. Hu, H. Liu, and J. Tang, “Classification of upper limb motion trajectories using shape features,” *IEEE Transactions on Systems, Man and Cybernetics C: Applications and Reviews*, vol. 42, pp. 970–982, 2012.
- [39] Z. J. Ju, G. X. Ouyang, M. Wilamowska-Korsak, and H. H. Liu, “Surface EMG based hand manipulation identification via nonlinear feature extraction and classification,” *IEEE Sensors Journal*, vol. 13, pp. 3302–3311, 2013.
- [40] A. Phinyomark, P. Phukpattaranont, and C. Limsakul, “Feature reduction and selection for EMG signal classification,” *Expert Systems with Applications*, vol. 39, no. 8, pp. 7420–7431, 2012.
- [41] U. R. Acharya, S. V. Sree, G. Swapna, R. J. Martis, and J. S. Suri, “Automated EEG analysis of epilepsy: a review,” *Knowledge-Based Systems*, vol. 45, pp. 147–165, 2013.
- [42] M. Besserve, K. Jerbi, F. Laurent, S. Baillet, J. Martinerie, and L. Garnero, “Classification methods for ongoing EEG and MEG signals,” *Biological Research*, vol. 40, no. 4, pp. 415–437, 2007.
- [43] D. Nauck and R. Kruse, “Obtaining interpretable fuzzy classification rules from medical data,” *Artificial Intelligence in Medicine*, vol. 16, no. 2, pp. 149–169, 1999.
- [44] L. I. Kuncheva and F. Steimann, “Fuzzy diagnosis: editorial,” *Artificial Intelligence in Medicine*, vol. 16, no. 2, pp. 121–128, 1999.
- [45] I. Güler and E. D. Übeyli, “Adaptive neuro-fuzzy inference system for classification of EEG signals using wavelet coefficients,” *Journal of Neuroscience Methods*, vol. 148, no. 2, pp. 113–121, 2005.
- [46] E. D. Übeyli, “Automatic detection of electroencephalographic changes using adaptive neuro-fuzzy inference system employing Lyapunov exponents,” *Expert Systems with Applications*, vol. 36, no. 5, pp. 9031–9038, 2009.
- [47] A. Yildiz, M. Akin, M. Poyraz, and G. Kirbas, “Application of adaptive neuro-fuzzy inference system for vigilance level estimation by using wavelet-entropy feature extraction,” *Expert Systems with Applications*, vol. 36, no. 4, pp. 7390–7399, 2009.
- [48] S. M. Pincus, I. M. Gladstone, and R. A. Ehrenkranz, “A regularity statistic for medical data analysis,” *Journal of Clinical Monitoring*, vol. 7, no. 4, pp. 335–345, 1991.
- [49] S. M. Pincus, “Approximate entropy as a measure of irregularity for psychiatric serial metrics,” *Bipolar Disorders I*, vol. 8, no. 5, pp. 430–440, 2006.
- [50] J. Bruhn, H. Ropcke, B. Rehberg, T. Bouillon, and A. Hoeft, “Electroencephalogram approximate entropy correctly classifies the occurrence of burst suppression pattern as increasing anesthetic drug effect,” *Anesthesiology*, vol. 93, no. 4, pp. 981–985, 2000.
- [51] D. E. Lake, J. S. Richman, M. Pamela Griffin, and J. Randall Moorman, “Sample entropy analysis of neonatal heart rate variability,” *The American Journal of Physiology—Regulatory Integrative and Comparative Physiology*, vol. 283, no. 3, pp. R789–R797, 2002.
- [52] S. M. Pincus and A. L. Goldberger, “Physiological time-series analysis: what does regularity quantify?” *The American Journal of Physiology—Heart and Circulatory Physiology*, vol. 266, no. 4, pp. H1643–H1656, 1994.
- [53] G. Ouyang, X. Li, C. Dang, and D. A. Richards, “Deterministic dynamics of neural activity during absence seizures in rats,” *Physical Review E: Statistical, Nonlinear, and Soft Matter Physics*, vol. 79, Article ID 041146, 2009.
- [54] M. Staniek and K. Lehnertz, “Parameter selection for permutation entropy measurements,” *International Journal of Bifurcation and Chaos*, vol. 17, no. 10, pp. 3729–3733, 2007.
- [55] X. Li and G. Ouyang, “Estimating coupling direction between neuronal populations with permutation conditional mutual information,” *NeuroImage*, vol. 52, no. 2, pp. 497–507, 2010.
- [56] J. S. R. Jang, “ANFIS: adaptive-network-based fuzzy inference system,” *IEEE Transactions on Systems, Man and Cybernetics*, vol. 23, no. 3, pp. 665–685, 1993.